ADVANCED RAPID COMPRESSION MACHINE TEST METHODS AND SURROGATE FUEL MODELING FOR BIO-DERIVED JET AND DIESEL FUEL AUTOIGNITION

By

Casey Allen

A DISSERTATION

Submitted
to Michigan State University
in partial fulfillment of the requirements
for the degree of

DOCTOR OF PHILOSOPHY

Mechanical Engineering

2012

ABSTRACT

ADVANCED RAPID COMPRESSION MACHINE TEST METHODS AND SURROGATE FUEL MODELING FOR BIO-DERIVED JET AND DIESEL FUEL AUTOIGNITION

By

Casey Allen

A rapid compression machine (RCM) has been designed and built for investigating the autoignition characteristics of bio-derived jet and diesel fuels. The RCM has been designed with a particular emphasis on versatility, so that non-volatile fuels may be tested in a premixed gas phase, as a fuel spray, or as an aerosol in an oxidizing bath gas. A blend of these test approaches provides insight into fundamental fuel kinetics and empirical knowledge of fuel performance in practical combustion systems.

A significant portion of this work is dedicated to the optimization of the RCM, and to the development of test methods and data analysis protocols. A novel approach to gas-phase charge preparation has been used in which premixtures are prepared directly in the test chamber by use of a fuel injector. Characterization experiments with JP-8 jet fuel confirm this new direct test chamber (DTC) charge preparation protocol is a viable approach for measuring high-fidelity gas-phase ignition delay data. The DTC approach enables efficient gas-phase testing of non-volatile fuels that may not otherwise be tested with the traditional large batch mixture test approach. For fuels that lack sufficient volatility for testing via the DTC approach, two alternatives have been developed. The fuel injector may be used for fuel spray ignition studies which yield practical data with regard to the coupled spray evaporation and ignition processes that are relevant to engines. A second approach introduces a fuel aerosol and oxidizing bath gas through an optimized poppet valve before undergoing wet compression in the RCM to vaporize the fuel. The compression process yields a gaseous mixture of fuel, oxidizer and diluent gases that

undergo autoignition. Characterization experiments with ethanol have been completed which demonstrate experimental repeatability for the aerosol ignition tests.

Bio-derived (camelina seed- and tallow-derived) alternative jet fuels, referred to as hydrotreated renewable jet (HRJ) fuels have been studied using the DTC approach. The large amount of paraffinic content in the HRJ fuels and lack of aromatic compounds relative to conventional JP-8 jet fuel leads to enhanced ignition quality. Ignition delay measurements are made at low compressed temperatures (625 K $\leq T_C \leq$ 730 K), compressed pressures of p_C = 5, 10, and 20 bar, and equivalence ratios of ϕ = 0.25, 0.5 and 1.0 in air. The camelina and tallow HRJ fuels exhibit similar autoignition characteristics, but the two fuels can be distinguished under stoichiometric conditions. Kinetic modeling is conducted with a 2-component surrogate (10 % *n*-dodecane/90 % 2-methylundecane) to evaluate the potential to predict ignition behavior of the HRJ fuels. Modeling results indicate that the surrogate fuel can only provide useful predictions at a limited set of conditions (p_C = 5 bar and ϕ = 1.0), and that the agreement of the model and experimental data improves with decreasing compressed pressure.

The RCM facility has also been used to study the spray ignition behavior of petrodiesel and fatty acid alkyl esters (*i.e.*, biodiesel) with varying alkyl chain lengths (methyl vs. butyl) and degrees of unsaturation imparted by using different feedstock oils (soy vs. canola). These tests have been conducted at the low temperatures (676 K $\leq T_C \leq$ 816 K) and reduced oxygen concentrations (12 % and 18 %) relevant to low temperature combustion schemes in advanced diesel engines. On average, the biodiesel (canola-derived methyl esters) ignited 23 % faster than diesel under similar test conditions.

To my wife, Fabiola,
thank you for your enduring love and
support – you are my hero

To my children, Olivia and Andrew,
the joy you bring to my life is without bound

ACKNOWLEDGEMENTS

Nearly six years ago, I was inspired by the author Thomas Friedman and his assessment in the book, *The World is Flat*, that the United States had lost its preeminent status in science and engineering. I resigned from a career-worthy job with Accenture in Chicago, intent on returning to graduate school to make a contribution that would return the U.S. to its former status. I made the naïve decision to work with a new assistant professor who had no funded research proposals, and my wife announced our departure to East Lansing to her employer, with no new job to speak of. Looking back, I can't describe what propelled us to make such seemingly risky decisions, but in the time since then, God has blessed our family abundantly with a loving marriage, two beautiful, healthy children, a home, the opportunity for my wife to maintain her job and work from home, and untold opportunities for my growth and development at MSU while working on exciting research projects. Yes, my adviser, with whom I so "naïvely" agreed to work, did receive funding – a lot of it!

As I prepare to move on to the next phase, I do so excitedly, but with a heavy heart because of how much I've enjoyed my time at MSU. Many people have made this experience what it's been, and I want to acknowledge them.

I cannot begin to express the depth of my gratitude toward my adviser, Prof. Tonghun Lee. Tonghun: we have enjoyed a high level of collaboration, camaraderie, and confidence in one another to make this a truly productive, synergistic, and joy-filled relationship. I can say with certainty that I will never again work so closely with a superior that I enjoy as much as you. You have an incredible talent for your role, and the success I've experienced at MSU is because of doors you have opened for me. You have treated me like family, and I am grateful for that. I hope that we can find opportunities to continue working together in the future.

I am also extremely grateful for the collaboration and support I have received from College of Engineering faculty, including Prof. Harold Schock, Prof. Elisa Toulson, Prof. Indrek Wichman, and Prof. Dennis Miller. I am indebted to Prof. Schock for his support of my role in designing and building the rapid compression machine. It was a leap of faith to ask a chemical engineer to lead such an intensive mechanical design project. Much of the characterization and testing work in the rapid compression machine has benefited a great deal from conversations and collaboration with Prof. Toulson – thank you.

To the students and staff at the Energy and Automotive Research Lab, thank you. Collaboration within the lab with Daniel Valco, Xing Rao, Steve Hammack, and Cody Squibb has been invaluable. The support of Jeff Higel and Gary Keeney has been critical to the success of my project, and without it, I may not be writing this for another 6 months.

I express the most genuine gratitude to all of my financial sponsors during my time at MSU, including the Department of Energy and Michigan State University. I have deepest gratitude for the support of Joe Colucci, not solely for the financial aspect, but also for the time Mr. Colucci has spent getting to know me.

None of this would have been possible without my family. To my parents, thank you. From a young age, you have taught me discipline, nurtured my dreams, and supported my educational pursuits. I could work a lifetime and not have repaid my debt. To my wife, Fabi, I am forever grateful. I spoke of my dream to go to school, trading in my salary for a stipend, and you never once objected, complained, or discouraged me. Your love, goodness, spirit of encouragement, and will to face tough challenges with me are an inspiration, and that’s why I love you.

TABLE OF CONTENTS

LIST OF TABLES

LIST OF FIGURES

LIST OF SYMBOLS

γ	Specific heat ratio
ΔH_c	Heat of combustion of fuel (*i.e.*, lower heating value)
$\bar{v}_p$	Mean piston speed
τ_1	First-stage ignition delay
τ_2	Second-stage ignition delay
τ	Total (overall) ignition delay
ϕ	Equivalence ratio
ϕ_{max}	Maximum equivalence ratio [for given initial temperature]
A	Interior surface area of RCM combustion chamber
A, B	Fitting parameters for molecular weight correlation
C_1, C_2, C_3	Arbitrary optimization parameter for heat loss model
C_D	Coefficient of discharge
C_p	Constant-pressure heat capacity
C_v	Constant-volume heat capacity
$C_{v,fv}$	Constant-volume heat capacity of fuel vapor
$C_{v,g}$	Constant-volume heat capacity of gas mixture
$C_{v,l}$	Constant-volume heat capacity of liquid fuel

h_c	Heat transfer coefficient (instantaneous)
$h_{v,Tint}$	Enthalpy of vaporization at temperature, T_{int}
ID	Ignition delay (equivalent to τ)
M	Molecular weight
m_f	Injected fuel mass
n_f	Moles of fuel
n_g	Moles of gas mixture
O/F	Oxidizer-to-fuel mass ratio
p	Pressure
p_0	Initial pressure
p_c	Compressed pressure
Q_c	Heat of combustion
$\dot{Q}_{c,m}$	Maximum apparent heat release rate
$\hat{\dot{Q}}_{c,m}$	Maximum apparent heat release rate normalized by τ, m_f, and ΔH_c
Q_w	Heat loss to the walls of the combustion chamber
t	Time
T	Mean gas temperature
T_0	Initial temperature
T_{10}	Temperature at 10 % volume recovery from distillation

T_{50}	Temperature at 50 % volume recovery from distillation
T_{90}	Temperature at 90 % volume recovery from distillation
T_b	Mixture boiling temperature
T_c	Compressed temperature
$T_{fl,0}$	Initial fuel temperature
$T_{g,0}$	Initial gas temperature (adiabatic-core calculation)
t_{inj}	Time of injection [after top dead center]
T_{int}	Intermediate temperature [at which vaporization occurs]
T_M	Molal average boiling temperature
T_{RZ}	Reaction zone temperature
T_V	Volumetric average boiling temperature
T_w	Temperature of the walls
V_0	Initial volume
V_c	Combustion cylinder volume
V_{eff}	Effective volume
v_{exp}	Volume expansion profile
v_p	Volume expansion polynomial
X_{O2}	Oxygen mole fraction

LIST OF ABBREVIATIONS

AHRR	Apparent heat release rate
APS	Average particle size
ATDC	After top dead center
BD	Biodiesel
CBE	Canola butyl ester (biodiesel)
CFD	Computational fluid dynamics
CFR	Cooperative fuels research
CHRJ	Camelina hydrotreated renewable jet [fuel]
CME	Canola methyl ester (biodiesel)
CN	Cetane number
CR	Compression Ratio
D2	No. 2 diesel (petroleum-derived)
DCN	Derived cetane number
DTC	Direct test chamber
EGR	Exhaust gas recirculation
EOC	End of compression
FAAE	Fatty acid alkyl esters
FAME	Fatty acid methyl ester
GC/MS	Gas chromatography/mass spectrometry
HEFA	Hydroprocessed esters and fatty acids

HMN	Heptamethylnonane
HRJ	Hydrotreated renewable jet [fuel]
ICCD	Intensified charge-coupled device
IQT	Ignition quality tester
LHV	Lower heating value
LTC	Low temperature combustion
NPT	National pipe thread
NTC	Negative temperature coefficient
PLIF	Planar laser-induced fluorescence
RCM	Rapid compression machine
SCFH	Standard cubic feet per hour
SME	Soy methyl ester (SME)
SOI	Start of injection
TDC	Top dead center
THRJ	Tallow hydrotreated renewable jet [fuel]
TIC	Total ion chromatogram
TKE	Turbulent kinetic energy
USAF	United States Air Force
VI	Virtual instrument

Chapter 1: INTRODUCTION

1.1. Background & Motivation

1.1.1. Application of a Rapid Compression Machine to Chemical Kinetics

A large portion of this work is devoted to a description of the design and construction of a rapid compression machine (RCM), a technical combustion device which has traditionally been used for investigating fuel ignition kinetics in a well-characterized, zero-dimensional system. The RCM test environment seeks to decouple chemical processes from transport process such as evaporation and mixing, in order to isolate the chemical reaction for study at a prescribed condition (*e.g.*, temperature, pressure, reactant concentration). Data acquired from a RCM is used to validate the global behavior (*i.e.*, ignition delay) and species concentration predictions of detailed kinetic mechanisms. Considering the objective of constructing a RCM and its intended purpose, it seems prudent to review available data in the literature to answer the following questions related to the value of chemical kinetics and RCM measurements:

- Can a RCM be used to establish a test environment that is truly homogeneous, without significant temperature and concentration gradients that would influence measurements and prevent using the data for mechanism validation?

- Are there limitations to the value of the data provided by a RCM? For which test conditions and test fuels can RCM measurements be considered suitable for mechanism validation?

In what follows, publications in the literature, as well as empirical data gathered as part of this work will be used to answer these questions.

Nature of the Rapid Compression Machine Test Environment

There are relatively few RCMs in existence and operation today, but there has been an historical development of these machines dating back to 1906 [4-5]. The first RCMs were used to investigate the autoignition temperature of fuels [4-5]. Affleck and Thomas [6] provide a review of these machines which were driven by the momentum transfer of falling weights or through the use of a flywheel-driven crank. The mechanics of modern RCMs are fundamentally different and are most often pneumatically-driven and hydraulically-stopped [6-10,1]. Notable exceptions include the University of Michigan free sabot piston design which is stopped by forming an interference fit between the piston and bore at the end of the stroke [11]; and the University of Science and Technology at Lille design which stops the piston with a specially-designed cam [12]. Modern designs enable RCMs to be operated with higher compression ratios (16 – 25) and short compression times (20 - 80 ms), making the apparatus well-suited to combustion kinetics studies. A more extensive review of existing RCMs is provided by Donovan et al. [11] and by Mittal [13].

For the development of kinetic models, it is essential that a computationally-tractable approach exist to model data obtained in a RCM. Kinetic simulations which require the full 3-D fluid mechanics to be modeled are not useful. With this in mind, RCMs are often designed to minimize fluid motion so that the system can be modeled as zero-dimensional. A number of studies have assessed the viability of this approach by characterizing the nature of the RCM test environment, and the most prominent of these are summarized here.

Griffiths et al. [14] conducted a rigorous characterization of the temperature and concentration fields in a RCM during compression and the early stages of reaction using schlieren photography, chemiluminescent imaging and planar laser induced fluorescence (PLIF).

In particular, the work of Griffiths et al. sought to identify temperature inhomogeneities introduced by gas motion in the post-compression period, and to characterize how these inhomogeneities interact with the autoignition chemistry to influence the spatial development of ignition within the RCM test chamber. At the outset, Griffiths et al. acknowledge the existence of a roll-up vortex identified in prior studies, and express concern over its role in obscuring the zero-dimensional nature of the gas core in the RCM. The authors of the work note several essential findings in the context of modeling the RCM environment as zero-dimensional, where there is no chemistry-transport interaction. To summarize, after reaching the end of compression (EOC), cool boundary layer gases are swept across the face of the piston and begin to penetrate into the core gas region in as little as 2 ms. For the low-to-moderate temperatures investigated by Griffiths et al., acetone PLIF measurements indicated a 40 K gradient between the cooler plug and the adiabatically-heated gases in the toroidal region surrounding the core. For gas phase oxidation processes, such a gradient can be significant, but Griffiths et al. suggest that zero-dimensional codes can be reasonably robust in their predictions provided that the fuel and test conditions are not overly susceptible to negative temperature coefficient (NTC) behavior. In the low-temperature oxidation regime where fuel reactivity exhibits positive temperature dependence, the reaction progresses most rapidly in the toroidal region and predictions are expected to be valid if the heat losses are well-characterized. This is true because the reference temperature calculated for the adiabatic core characterizes the experiment and drives the reaction chemistry. For moderate temperatures, where NTC behavior can predominate, this may not be the case because the early stages of reaction occur most rapidly in the cooler core. These reactions augment the temperature so as to minimize temperature inhomogeneities, which may seem to be desirable; however, reactive intermediates are also generated during these stages which make the cooler core more sensitive to subsequent phases of reaction. In other words, the main hot ignition event may be dictated by temperature conditions in the cooler core that are not representative of the reference temperature for the experiment. Finally, the conclusions of Griffiths et al. must be viewed with the understanding that the RCM at The University of Leeds does not include a creviced piston to suppress vortex formation and support the longevity and uniformity of the adiabatic core. Although the general conclusions regarding the timescales for core deterioration may not be applicable to RCM designs with creviced pistons (as in this work), the interpretation of the regimes which drive the ignition process is valid for any RCM system where thermal stratification exists.

Mittal and Sung [15] performed extensive temperature characterization of the core gas region after compression for a flat piston and a piston machined with a numerically-optimized crevice design. Acetone PLIF measurements were recorded to assess the uniformity of the core gas temperature. Mittal and Sung concluded that a flat piston was incapable of producing a zero-dimensional environment due to mixing of hot and cool gases, but that the creviced piston significantly augmented the volume of the adiabatic core region. It was observed that the survival of the core volume is influenced by test conditions, with lower pressures leading to faster deterioration. Based on these results, Mittal and Sung indicate that the RCM environment may be modeled as zero-dimensional for post-compression times of up to 100 ms when a creviced piston is used.

Accepting the existence of an adiabatic gas core does not eliminate other concerns about the quality of the reactive environment in the RCM. A full understanding of the reaction conditions requires an accurate representation of heat loss from the RCM, which is essential for modeling the data as zero-dimensional. Conventional methods rely on experimental means to quantity the heat loss for each unique test [1,16]. The need to do so is highlighted by the work of Würmel et al. [17] in which the dependence of fuel ignition delay on diluent gas composition, and hence mixture thermophysical properties (*i.e.,* specific heat, thermal conductivities), was investigated. As part of the work, the autoignition of 2,3-dimethylpentane was studied with diluent gas compositions that included nitrogen, argon, helium, xenon and blends of nitrogen and argon. Würmel et al. discovered that for commonly used test times in the RCM (1 – 200 ms post-compression) the adiabatic core temperature was not sufficient to characterize the ignition delay, and that the heat loss rate determined by the diluent gas composition plays a significant role in governing the development of autoignition. In fact, for tests with helium, the heat loss rate was so excessive that the authors advise against its use in RCM tests. For the reader, the essential consequence to understand is that even with a creviced piston in place, the gas composition is an important consideration for determining the validity of the adiabatic core hypothesis.

Limitations to the Value of RCM Data

The previous section highlights some of the specific limitations to gathering valuable RCM data. For designs with a creviced piston, some of the fuel and oxidation regime concerns are mitigated, and the primary concern becomes measuring the ignition phenomena within what is considered a well-characterized test time. Figure 1-1 has been adapted from the work of Prof. R.K. Hanson at Stanford University [18], and it illustrates the relationship between *n*-dodecane ignition delay times and the shock tube and RCM devices available for their measurement. The boundaries of the RCM test times illustrated in Figure 1-1 consider two limiting cases. The upper limit of the test time describes the interval after compression for which the core conditions (*i.e.*, adiabatic reference temperature) can be considered valid. The details of this have been discussed in the prior section. The lower test time boundary concerns the influence of the RCM compression process on the ignition delay measurements. For highly reactive fuels and test conditions, the ignition reactions can be initiated during the late stages of compression. This is increasingly problematic for ignition delays less than 10 ms. In these test cases, the reference temperature is not established prior to the start of the reaction, and error is introduced into the measurement. An additional concern relates to the accurate assignment of the initial test conditions which can be challenging when the RCM must be heated to volatilize a fuel sample. This potential source of error is quantified in § 2.1.2.

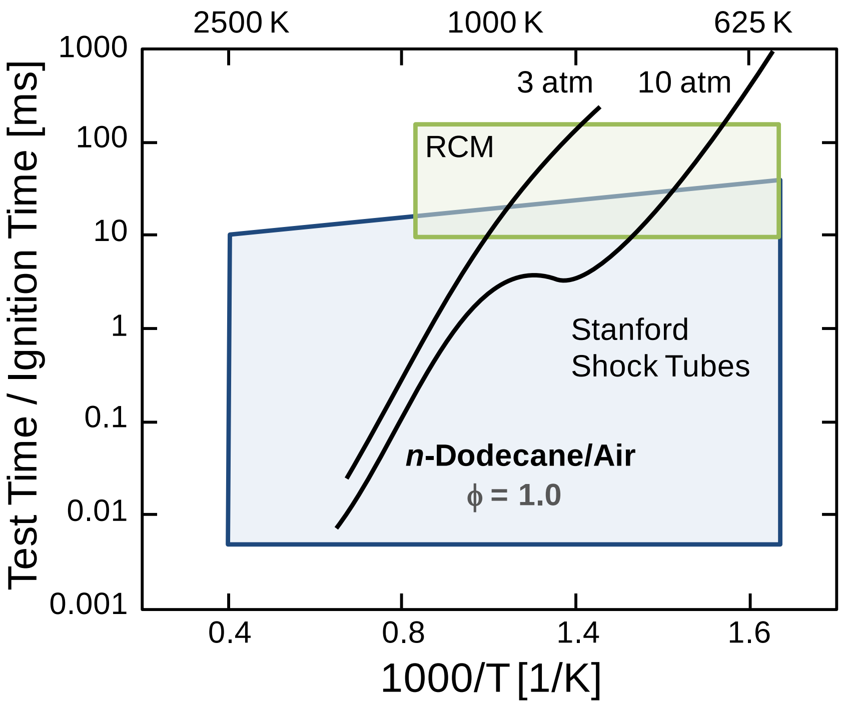

Figure 1-1. RCM and shock tube (ST) test times relative to *n*-dodecane ignition delay times over a broad range of temperature conditions. For interpretation of the references to color in this and all other figures, the reader is referred to the electronic version of this dissertation.

1.2. Objectives and Scope of Research

The purpose of this work is to design, build and characterize a versatile rapid compression machine that can be used to investigate the autoignition characteristics of non-volatile fuels (*e.g.*, jet fuel, diesel fuel), and to use the RCM to investigate the ignition kinetics of bio-based jet and diesel fuels. Central to the characterization of the RCM has been the development of advanced test methods that are capable of creating a well-characterized test environment in which ignition delay measurements may be made. Creating this type of test environment for a non-volatile fuel is challenging, particularly if a premixed system is desired.

The preferred method for testing a fuel in the RCM involves preparing the reactive charge directly in the heated test chamber, allowing sufficient time for fuel volatilization and mixing. Extensive characterization work has been performed to identify the minimum time required for fuel volatilization and mixing to create a homogeneous premixture of fuel, oxygen and diluent gases. Preparation of the premixture directly in the test chamber is a novel approach, but one that confers benefits compared to conventional methods (*e.g.*, reduced initial temperatures, fuel system simplification, and minimization of fuel condensation concerns). Secondary test methods that investigate the compression ignition of a fuel spray or wet-compression of a fuel aerosol may also be employed.

The ignition characteristics of new bio-based jet fuels being developed by the U.S. Air Force are investigated and compared with those of conventional jet fuels. The results of these tests yielded the first known kinetic ignition data for bio-synthetic jet fuels. The objective of these tests is to gather data that will support development of the surrogate fuels and kinetic models needed to expedite integration of the fuels into the U.S. Air Force fleet. In this particular work, a two-component surrogate fuel is investigated for that purpose, so that it may be integrated into combustor simulations as a means to predict performance. One significant barrier to the integration of these alternative fuels is their low volumetric energy density relative to conventional petroleum-based fuels. As a potential solution to this problem, the addition of aluminum nanoparticles in the liquid fuel is proposed with the objective of increasing the energy density of the fuel blend. The ignition and combustion enhancement effect of including the nanoparticles is reported at low nanoparticle concentrations which may not be considered harmful to gas turbine operation.

To support the increased adoption of biodiesel in the U.S. market, the ignition characteristics of biodiesels with improved physical properties (*i.e.*, superior cold-flow) are investigated. The ignition measurements are made by compression-igniting a fuel spray in the RCM in a test mode that mimics the behavior of a diesel engine. These tests enable observation of the practical ignition behavior of a fuel under realistic engine conditions. In a broader sense, the tests serve the purpose of investigating important changes in the combustion characteristics of a fuel whose chemical composition has been altered to elicit an improved physical property.

1.3. Structure of the Dissertation

This dissertation is composed of 6 chapters, and the scope of the content is described in the previous section. Chapter 2 is devoted to a detailed description of the RCM test facility, including available test methods and characterization data for each of these test methods. Particular emphasis is given to the test strategy which prepares reactants directly in the test chamber. Chapter 3 presents data regarding the autoignition characteristics of conventional and bio-synthetic jet fuels. Ignition delay measurements for these fuels are made by compression-igniting premixed charges, and the data are used to assess the viability of using a 2-component surrogate fuel to predict the autoignition characteristics of the fuel. Chapter 4 is based on a study of the ignition characteristics and heat release rates of petrodiesel and biodiesels made from different feedstocks (soybeans vs. canola seed) or transesterified with unique alcohols (methanol vs. *n*-butanol). Chapter 5 presents an investigation of the potential to enhance the ignition and combustion characteristics of a liquid fuel by including low concentrations of aluminum nanoparticles. Data regarding the experimental repeatability are presented, as is data demonstrating the reduction in ignition delay for ethanol and JP-8 when 2 %-wt nanoparticles are included in the liquid fuels. Concluding remarks and suggestions for future work appear in Chapter 6.

The research that is recorded in this work has been compiled from previously published journal articles and from manuscripts being reviewed for publication. For convenience, these articles are referenced here, and the reader is directed to the journal articles for additional information:

8 **Ignition Behavior and Surrogate Modeling of JP-8 and of Camelina and Tallow Hydrotreated Renewable Jet Fuels at Low Temperatures**
Proceedings of the Combustion Institute (In Review)
C. Allen, D. Valco, E. Toulson, T. Edwards, T. Lee

7 **Application of a Novel Charge Preparation Approach to Testing the Autoignition Characteristics of JP-8 and Camelina Hydroprocessed Renewable Jet Fuel**
Combustion and Flame (Accepted)
C. Allen, E. Toulson, T. Edwards, T. Lee

6 **An Investigation of the Influence of Fatty Ester Composition on Biodiesel Combustion**
Biomass & Bioenergy (Submitted)
C. Allen, E. Toulson, D. Tepe, H. Schock, D. Miller, T. Lee

5 **Ignition Characteristics of Diesel and Canola Biodiesel Sprays in the Low-Temperature Combustion Regime**
Energy & Fuels, Vol. 25, pp. 2896-2908 (2011)
C. Allen, E. Toulson, D. Hung, H. Schock, D. Miller, T. Lee

4 **Modeling the Autoignition of Fuel Blends with a Multi-step Model**
Energy & Fuels, Vol. 25, pp. 632-639 (2011)
E. Toulson, C. Allen, D. Miller, J. McFarlane, H. Schock, T. Lee

3 **An Aerosol Rapid Compression Machine for Studying Energetic-Nanoparticle-Enhanced Combustion of Liquid Fuels**
Proceedings of the Combustion Institute, Vol. 33, pp. 3367-3374 (2010)
C. Allen, G. Mittal, C.-J. Sung, E. Toulson, T. Lee

2 **Optimization of a Multi-step Model for the Auto-Ignition of Dimethyl Ether in a Rapid Compression Machine**
Energy & Fuels, Vol. 24, pp. 3510-3516 (2010)
E. Toulson, C. Allen, D. Miller, H. Schock, T. Lee

1 **Modeling the Auto-Ignition of Oxygenated Fuels using a Multi-step Model**
Energy & Fuels, Vol. 24, pp. 888-896 (2010)
E. Toulson, C. Allen, D. Miller, T. Lee

Chapter 2:

EXPERIMENTAL FACILITY & METHODS

2.1. Rapid Compression Machine

A heated RCM has been designed, built and characterized as a central part of this work for the purpose of investigating the ignition kinetics of conventional and alternative fuels. The RCM is pneumatically-driven and hydraulically-stopped. The design of the RCM has been focused on addressing the challenges associated with creating homogeneous premixtures of non-volatile fuels, and hence obtaining kinetic data for these fuels. New approaches have been developed for creating premixtures which rely on a fuel injector to load liquid fuel directly into the test chamber for each test or rely on wet-compression of an aerosol fuel in an oxidizing bath gas. These approaches extend the test range of traditional RCM designs, and extensive characterization work has been completed to evaluate these strategies for their ability to produce high-fidelity kinetic data.

2.1.1. General RCM Specifications

A schematic of the RCM test facility appears in Figure 2-1 and photographs of the facility appear in Figure 2-2. The RCM is pneumatically-driven by a 5-inch diameter piston. The pneumatic chamber has been custom built by Peninsular Cylinders and is capable of operating with pressures up to 300 psi. The rear of the pneumatic chamber is cut with a 3” NPT port through which high pressure air expands to propel the piston during operation. A 20 gallon air reservoir is attached to the pneumatic chamber to maintain approximately 95 % of the initial driving pressure throughout the stroke. The front of the pneumatic chamber is cut with three

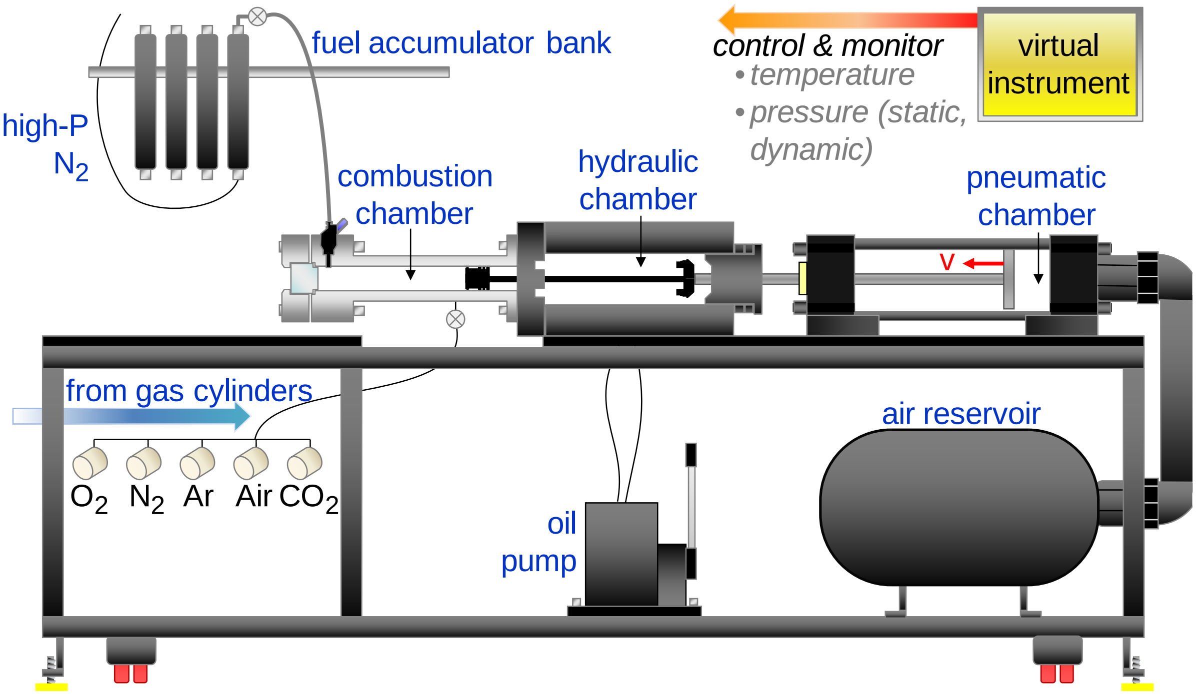

Figure 2-1. Schematic of the rapid compression machine test facility.

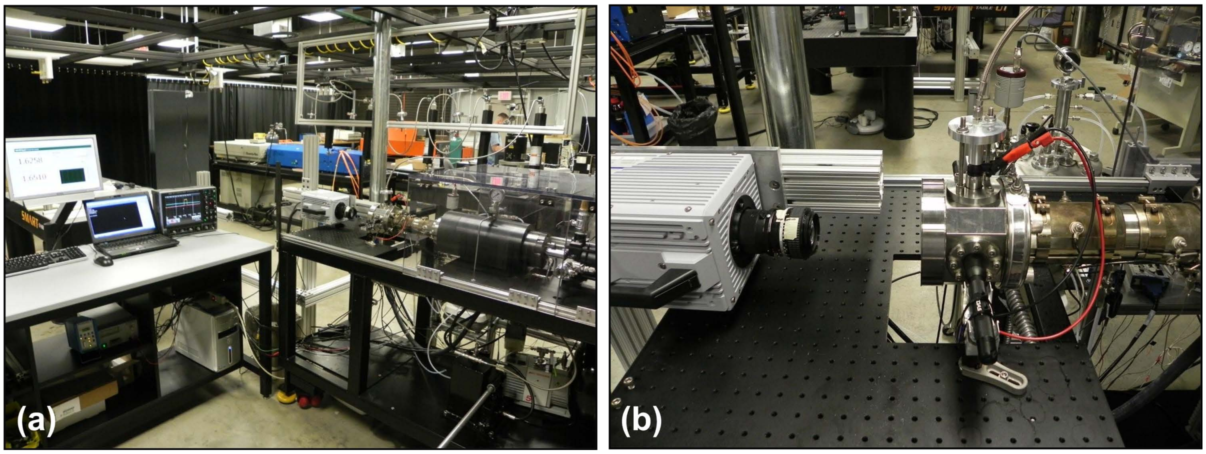

Figure 2-2. Photos of the (a) full RCM test facility and (b) the test chamber setup for visualization of fuel spray ignition.

vents to quickly evacuate the air ahead of the pneumatic piston during the stroke. The vents are 1” NPT ports outfitted with full-port ball valves.

The RCM piston assembly is hydraulically-stopped by a cupped piston that enters a groove filled with oil to generate hydraulic pressure and decelerate the piston. The hydraulic piston governs the limits of motion for the piston assembly; the starting position of the stroke is determined by where the hydraulic piston touches the stroke adjustment piece, and the end of the stroke occurs when the hydraulic piston strikes the stopping ring. The stroke length may be set to 8”, 9”, or 10” based on the number of shims installed. The hydraulic piston is constructed of two pieces of 1018 cold-rolled steel that compress and hold an o-ring that is used to seal the hydraulic chamber for pressurization. The pressure in the hydraulic chamber is quickly relieved during operation and the pneumatic chamber begins to drive the piston forward. A two-piece piston design that tightly grips the o-ring ensures the ring will not fall out during operation. Additional specifications for the hydraulic piston appear in § 2.1.3.

Ignition tests are carried out in the 2-inch diameter combustion chamber by compressing the charge to its autoignition temperature while continuously monitoring the chamber pressure using a Kistler 6125B piezoelectric pressure transducer. The combustion chamber is fabricated from 304 stainless steel and the inner diameter is plated with a thin layer of chrome (0.0005”) to provide a smooth bore for the piston to ride. The RCM can be equipped with a flat piston, or a creviced piston may be used to decouple the fluid dynamics from the fuel kinetics. Both pistons are fabricated of 6061 aluminum and are anodized black. The creviced piston minimizes fluid motion during compression, and its geometry is based on the optimized design of Mittal and Sung [1]. The crevice is machined near the leading edge of the piston, and two additional glands are machined to accept Parker polypak seals that seal during compression and when vacuuming the chamber before a test. The dimensions of the creviced piston appear subsequently in Figure 2-18c. The standard clearance at top dead center (TDC) is 0.5”, but this may be altered by including 1/16” shims between the hydraulic chamber and combustion chamber, or by altering the piston rod length with 1/4” spacers. Combined with the ability to change the stroke length, this allows nearly continuous variability of the compression ratio (CR) between 4 and 17 with the creviced piston and 4.8 and 21 for the flat piston. The head piece of the combustion chamber provides optical access through fused silica windows (Hereaus, Suprasil 2 Grade). A laser beam or laser sheet may be passed through the side windows and the end window may be used for imaging. The windows are replaced with stainless steel replicas when optical diagnostics are not being used. The windows and stainless steel replicas are sealed by viton o-rings placed around the perimeter. The combustion chamber is equipped with band heaters for controlled charge heating, and the engineering of the heating system is described in detail in § 2.1.3. The initial pressure is measured with a manometer (Baratron 626B or Omega PX409-050A10V) that is adjacent to a charge inlet line. The manometers are also used to measure the partial pressures of gas components in a mixing vessel. The vessel is used to manometrically prepare oxygen and diluent gas mixtures used for testing.

2.1.2. Major Engineering Challenges & Design Considerations

The superior approach for obtaining kinetic ignition data from a RCM is to first create a premixed charge of reactants and to subsequently compress the mixture to autoignition conditions with minimal fluid motion. This approach creates a zero-dimensional, homogeneous environment that isolates the ignition chemistry from the physical transport processes of fuel vaporization and the convective and diffusive flows of reactant species. Establishing this type of environment in a RCM for testing non-volatile fuels is challenging, and has been prohibitive when measuring the ignition characteristics of kerosene-type fuels under rich conditions, diesel fuels, and biodiesels. For all of these fuels, the test chamber of the RCM must be preheated to vaporize all of the fuel components, but this must be done with care so that (1) the temperature field within the test chamber is uniform and that (2) the preheat temperature is mild enough to avoid thermal decomposition of the test fuel.

The importance of temperature uniformity in the test chamber is paramount when gathering ignition delay data to support chemical kinetic models. Reference temperatures used to characterize the measurements must be accurately known, and if they are not, large errors can be introduced into the Arrhenius kinetic parameters that are tuned based on experimental data. Inaccuracies in the measured initial temperatures are amplified when calculating the compressed temperature conditions which are used to characterize the test condition. This amplification occurs because compressed temperatures are calculated using the adiabatic compression relationship, $\int_{T_0}^{T_c} \frac{\gamma}{\gamma-1} \frac{dT}{T} = \ln \frac{p_c}{p_0}$, where T is the temperature, γ is the specific heat ratio, p is the pressure, and the subscripts *0* and *c* correspond to the initial and compressed states, respectively.

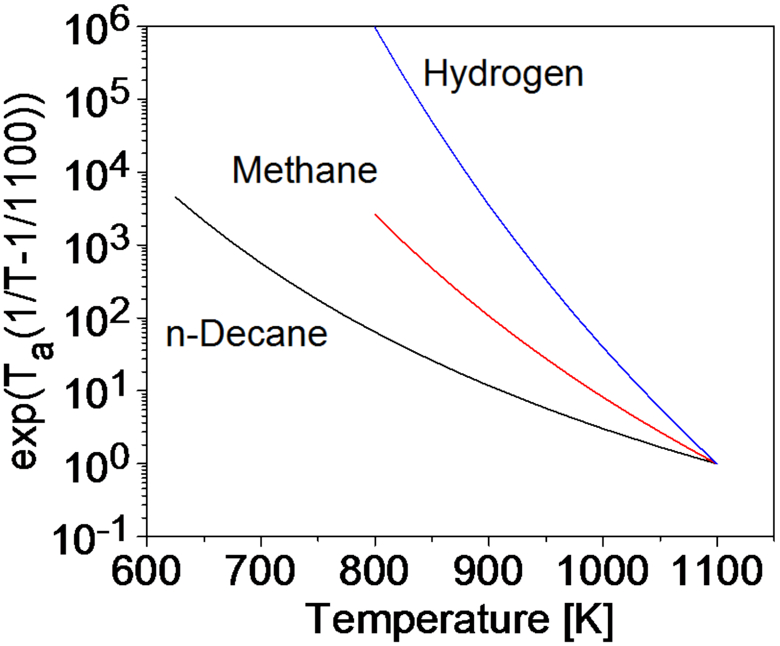

Figure 2-3. Temperature dependence of ignition delay correlations for *n*-decane, methane, and hydrogen.

The level of amplification increases with increasing compression ratio, but even for modest compression ratios, the error can be magnified two-fold. The significance of poor temperature characterization is evident when considering the strong influence of temperature on fuel ignition kinetics. Ignition delay correlations published for *n*-decane [19], methane [20] and hydrogen [20] have been used to evaluate temperature sensitivity over the low-to-moderate temperature range, and the results appear in Figure 2-3. Over the temperature range considered, the ignition delay changes by orders of magnitude, and even for the modest change of 10 K (750 K – 760 K), the ignition delay of *n*-decane is reduced by approximately 20 %. This type of strong dependence on temperature illustrates the importance of carefully characterizing the temperature field in the RCM, and subsequent sections describe the engineering effort undertaken to control and describe the initial temperature in the RCM test chamber.

The second, and related, challenge is to select an initial temperature for fuel volatilization

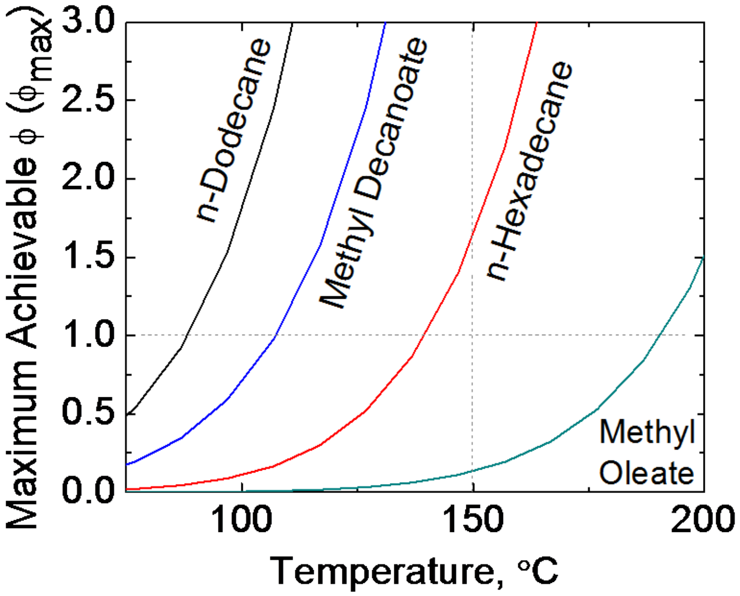

Figure 2-4. Maximum achievable equivalence ratios as a function of temperature for *n*-dodecane, methyl decanoate, *n*-hexadecane, and methyl oleate (calculations assume a total mixture pressure of 1 bar).

that does not lead to thermal decomposition of the fuel. The maximum achievable equivalence ratios (ϕ_{max}) for a range of initial temperatures have been calculated for *n*-dodecane, methyl decanoate, *n*-hexadecane, and methyl oleate using vapor pressure correlations for these fuels. These calculations assume a total mixture pressure of 1 bar, and the results appear in Figure 2-4. It is observed that *n*-dodecane (jet fuel surrogate) and methyl decanoate (biodiesel surrogate) may be tested at a wide range of equivalence ratios using temperatures less than 150 °C, where fuel decomposition increasingly becomes a concern. However, *n*-hexadecane (diesel surrogate) tests are limited to mildly rich conditions in order to maintain temperatures less than 150 °C, and methyl oleate (biodiesel component) cannot even be tested under stoichiometric conditions without approaching temperatures of 200 °C. Subsequent sections of this work describe an approach designed to minimize initial test temperatures, and extensive chemical analysis is conducted to ensure no fuel decomposition occurs during testing.

2.1.3. Novel Design Aspects of the Rapid Compression Machine

Test Mode Overview: Premixed, Spray Ignition, Aerosol Wet-Compression

The novelty of the RCM is due primarily to the various operation modes that are accommodated, and the engineering and design elements described in the following sections. The foundation of the RCM is based on the premixed testing mode for which RCMs have been conventionally used; however, a modification to this test approach has been developed whereby liquid fuel is loaded directly into the test chamber and volatilized by heating. Practical spray ignition measurements are also possible using the fuel injector to dispense a single injection into compression-heated gas. This approach creates a test environment similar to a diesel engine, and can be used to investigate relative ignition behavior of fuels. Finally, an aerosol testing mode is enabled by replacing the end window and flange with a poppet valve. During testing, a fuel

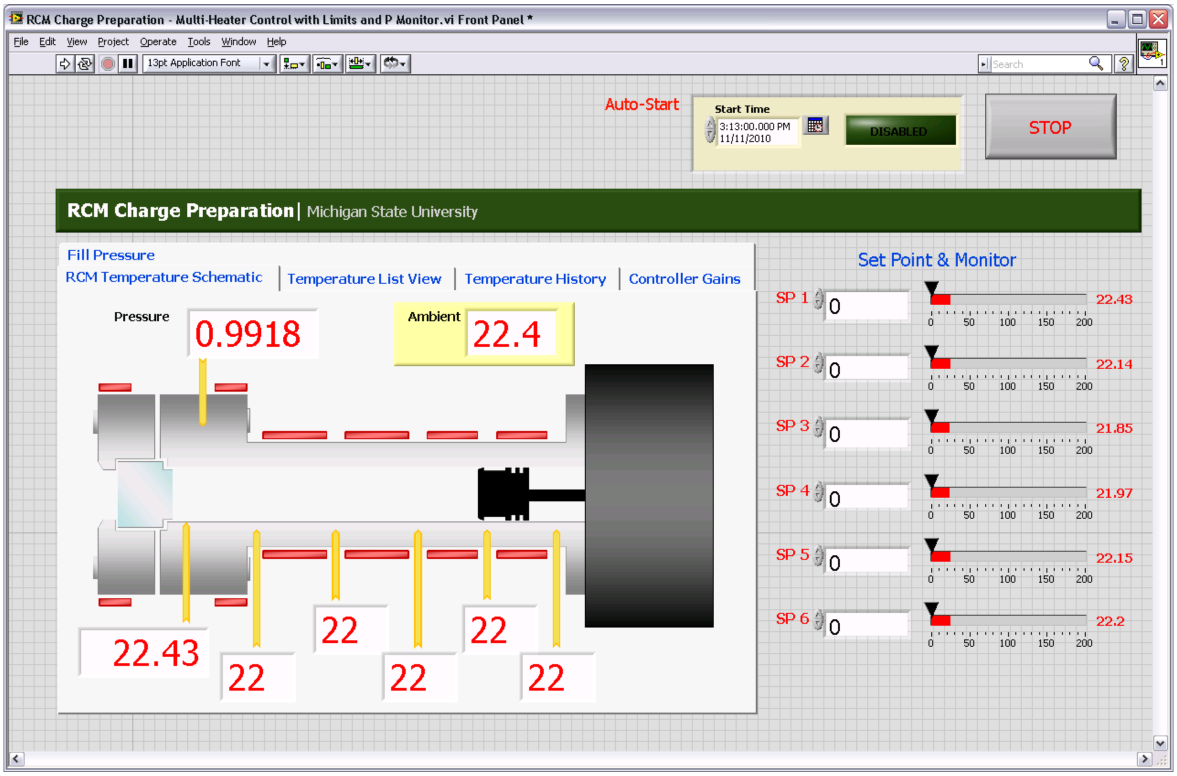

Start Time 3:13:00.000 PM 11/11/2010

Pressure 0.9918

Ambient 22.4

22.43
22
22
22
22
22

SP 1 0 22.43
SP 2 0 22.14
SP 3 0 21.85
SP 4 0 21.97
SP 5 0 22.15
SP 6 0 22.2

Figure 2-5. LabView virtual instrument used to control the combustion chamber temperature and monitor the mixture pressure.

aerosol flows continuously through the test chamber before the inlet (poppet) and outlet valves close and the compression process begins. Characterization work confirms that the aerosol approach is not suitable for measuring high-fidelity kinetic data, but that it can provide repeatable test results and is useful for investigating advanced combustion concepts. The details of each of these approaches, including relevant characterization data, appear in this chapter.

Temperature Control System

The low vapor pressures of the jet fuels tested in this study require that the fuel and oxidizer mixtures be heated to ensure the fuel is in the vapor phase. The RCM temperature is maintained using six individual electrical band heaters that are wrapped with high-temperature insulation. The heaters are controlled by a National Instruments LabView virtual instrument (VI) (screenshot in Figure 2-5) that receives feedback from six thermocouples that are embedded

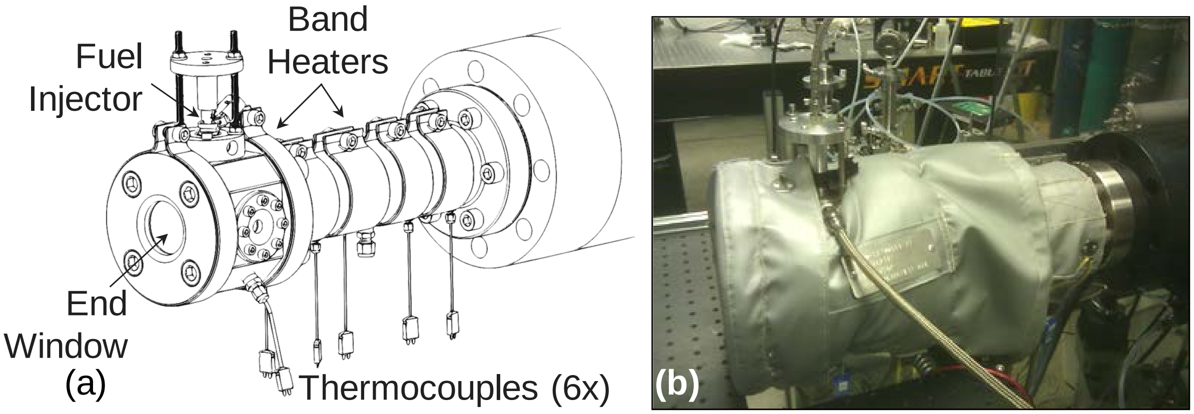

Figure 2-6. . (a) Depiction of the arrangement of the band heaters and thermocouples used to control the combustion chamber temperature. (b) Photograph of high-temperature insulation used to promote temperature homogeneity in the test chamber.

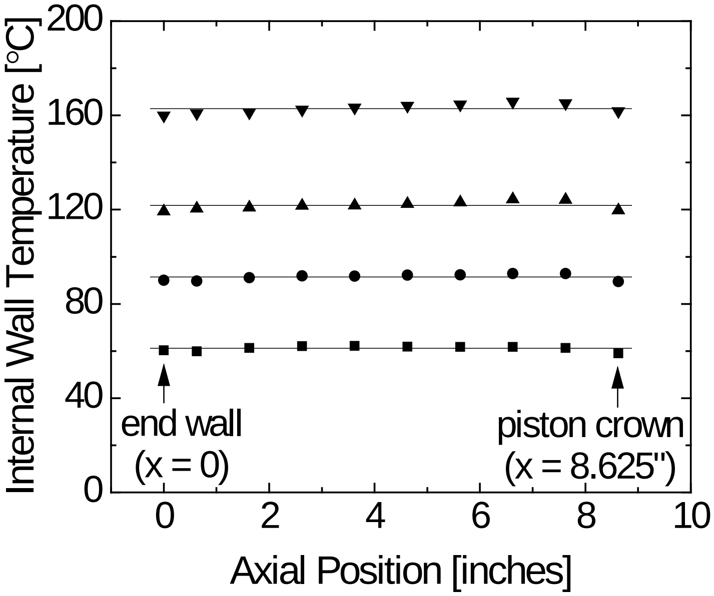

Figure 2-7. Wall and piston temperatures measured in the RCM test chamber at four unique control temperature setpoints.

within the walls of the combustion chamber. The placement of the heaters and the thermocouples appears in Figure 2-6a and the extent of the insulation is shown in Figure 2-6b. Each heater is wired to a junction box where it is connected to a solid-state relay that is pulse-width modulated to maintain the temperature setpoint. It is critical that the heating mechanism provides a homogeneous temperature field in the RCM, so that the ignition kinetics are not affected by any local hot spots. As such, the temperature profile of the combustion chamber was examined by using a thermocouple to measure the temperature at multiple wall locations, the end wall, and the piston crown. Four unique temperature control set points were tested, and the results are compiled in Figure 2-7. The data demonstrate that there is little variation in the wall temperature at different axial positions. However, the variation does increase at higher temperature set points. It is also noted that two depressions in the measured temperatures exist. The first occurs near the end wall, and is an effect of the cooling water that passes through the flange used to mount the fuel injector. The coolant is necessary to reduce the temperature experienced by the main body of the fuel injector and thus promote consistent performance of the injector. The second temperature depression is observed at the piston crown, which occurs because the piston does not have direct physical contact with the heated walls. Neither of these temperature depressions is considered to be significant because the deviation is no more than 1.3 % (3.2 – 5.8 K) from the maximum measured temperature for a given set point.

Fuel Injection System

The fuel loading requirement for each test in the RCM is very small (typically 10 – 100 mg), and thus the creation of a single premixture requires a high resolution method for metering the fuel into the test chamber. Fuel injectors are a well-developed technology capable of this resolution. A production gasoline direct injection fuel injector has been chosen for the system because it provides repeatable injections and it is easily controlled with an injector driver box and a LabView VI. To ensure the injector operates as expected while the RCM is heated, the injector body is water-cooled. This has a trivial influence on the wall temperature of the RCM, as described in the previous section, because the cooling channel is located sufficiently far from the interior of the combustion chamber. Fuel is delivered to the injector by a stainless steel flexible

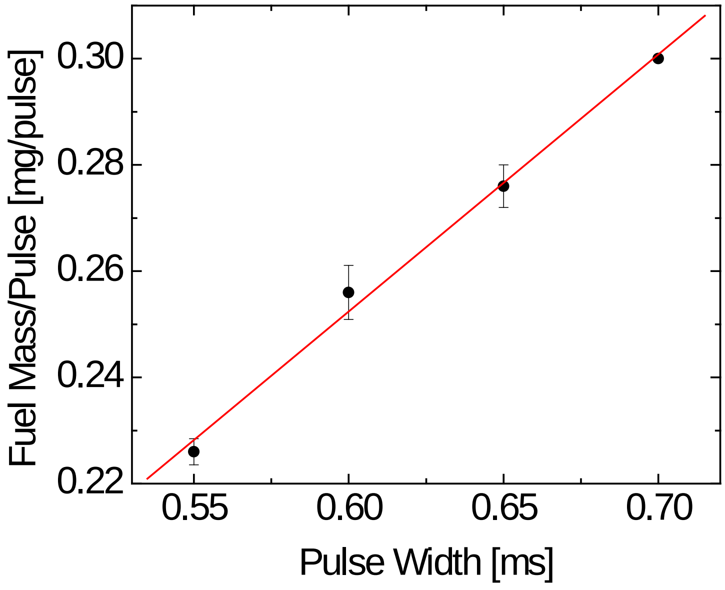

Figure 2-8. Fuel injector calibration curve for JP-8 jet fuel describing the injected fuel mass as a function of injection pulse width.

tube that is connected to a hydraulic piston accumulator which acts as a pressurized fuel reservoir. Compressed nitrogen is used to pressurize the fuel line to 3 MPa. By sending a TTL pulse to the injector driver box, the injector is opened for a duration of time that corresponds to the TTL pulse width, and the liquid fuel sprays into the RCM.

Each unique combination of a fuel injector and a test fuel must be calibrated. A calibration curve is constructed that describes the injected mass as a function of pulse width. Several pulse widths are selected as calibration points, and for each point, a series of injections (≥ 100) are collected in a container. The total mass of the injections is determined by measuring the mass of the container before and after the test which allows direct calculation of the fuel mass per injection. Care is taken to select calibration points in the linear operating region of the injector so a linear fit can be safely applied to the data. The fit is used to calculate the number and duration of the injections required for each test. It should be noted that relatively short pulse widths are selected for the calibration points so that multiple injections are required for each test

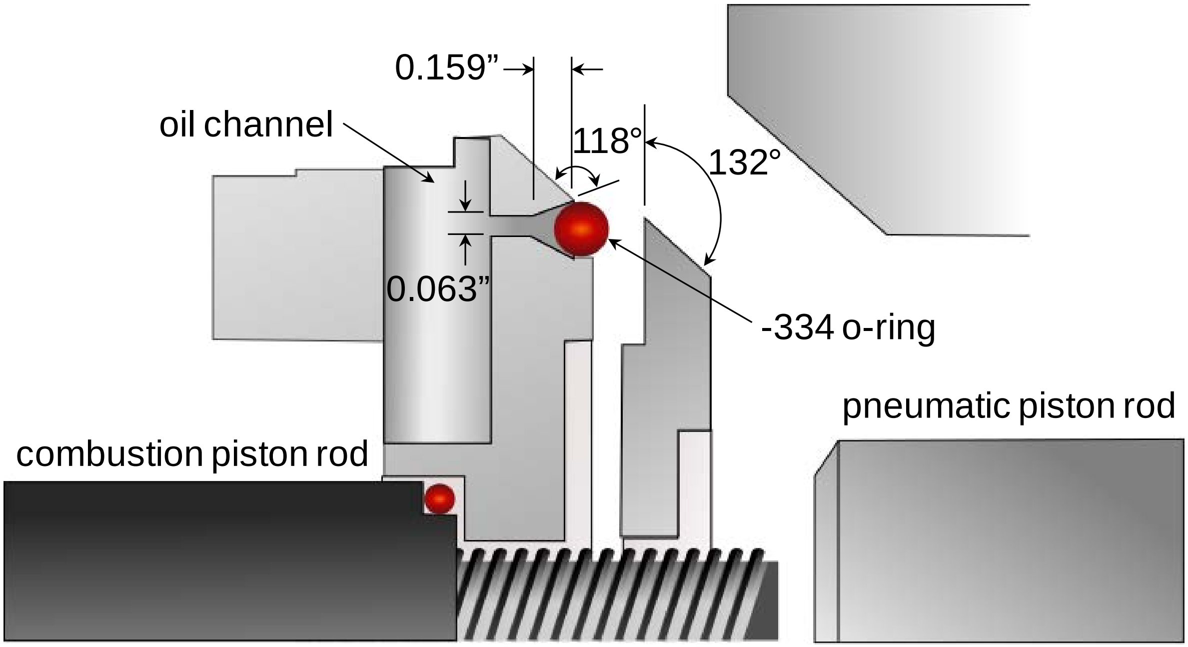

Figure 2-9. Hydraulic piston assembly.

(typically 5 – 35). This minimizes the effect of any shot-to-shot variation that could influence test results where a single injection is used. A sample calibration curve appears in Figure 2-8 for JP-8 fuel. Error bars have been included in the plot, which represent the standard error in five measurements at each calibration point. The data clearly demonstrate the linear relationship between the injection pulse width and the injected mass over the calibrated range of pulse widths.

Hydraulic Piston

The o-ring seal that exists at the interface between the hydraulic chamber and the hydraulic piston is subjected to a strong shearing force during operation of the RCM. With the original one-piece hydraulic piston design, the shearing force was sufficient to pull the o-ring from its gland, thus requiring that the hydraulic chamber be opened and a new o-ring installed. To avoid this time-consuming remedy and to ensure maintenance-free operation, a two-piece hydraulic piston was designed. A schematic of the new piston design appears in Figure 2-10,

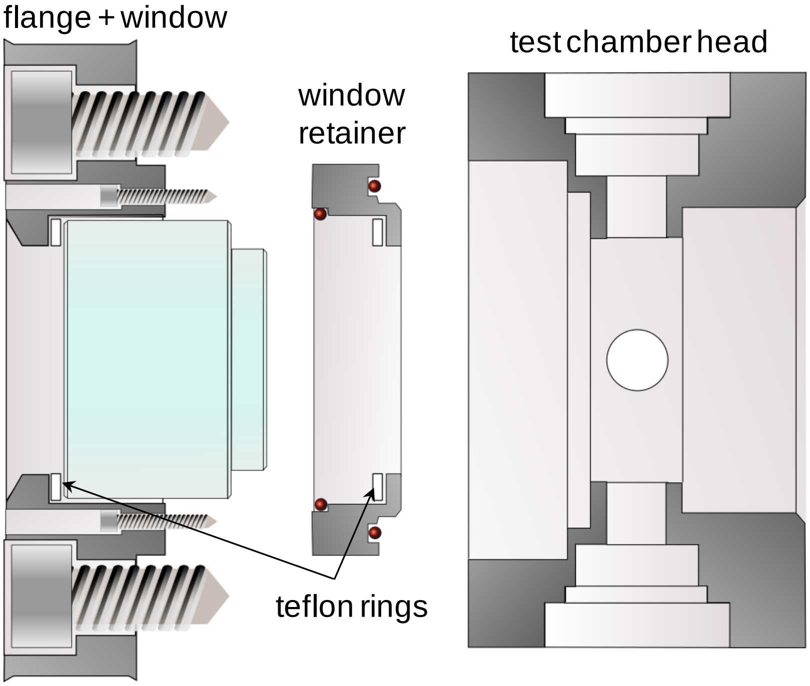

Figure 2-10. RCM test chamber head assembly for clamping window into place.

which illustrates the stacking assembly of the piston and rod parts. The rod coming from the combustion chamber threads into the pneumatic chamber piston rod, and the hydraulic piston pieces are held firmly between the rods. An oversized o-ring (size -334) is compressed between the two hydraulic piston pieces, and is used to form a seal against the back of the hydraulic chamber. The new design has been used successfully without a failure event for approximately 3000 tests since its fabrication.

High-Pressure Window Design

The fused silica windows used for optical access into the RCM must be cleaned intermittently. The frequency of cleaning is dependent on the test conditions used. The windows have been designed to minimize concerns about breakage during cleaning. In the design, which is illustrated in Figure 2-10, the window is held between a flange and a retainer ring. To avoid contact with the metal parts, the window is supported by teflon rings on both sides. The main advantage of this design is that when the window must be cleaned, the entire flange and retainer assembly is removed from the test chamber head for cleaning. The window is not directly handled while cleaning, and by remaining within the flange and retainer assembly, the torque settings on the bolts and alignment of the window is not altered.

2.2. Premixed Mode: Direct Test Chamber Charge Preparation

Fundamental measurements of ignition delays are most frequently carried out in RCMs and shock tubes, each of which require a means to prepare premixtures of fuel, oxidizer and diluent gases. For a non-volatile fuel, this is typically accomplished by means of a separate vessel that is heated and stirred. Premixtures using non-volatile fuels and prepared in a separate vessel require sufficient residence times at elevated temperatures to evaporate and mix. Samples are transferred from the mixing vessel to the test device over a period of several hours, and the extended exposure to high temperatures increases the risk of thermal decomposition of the fuel.

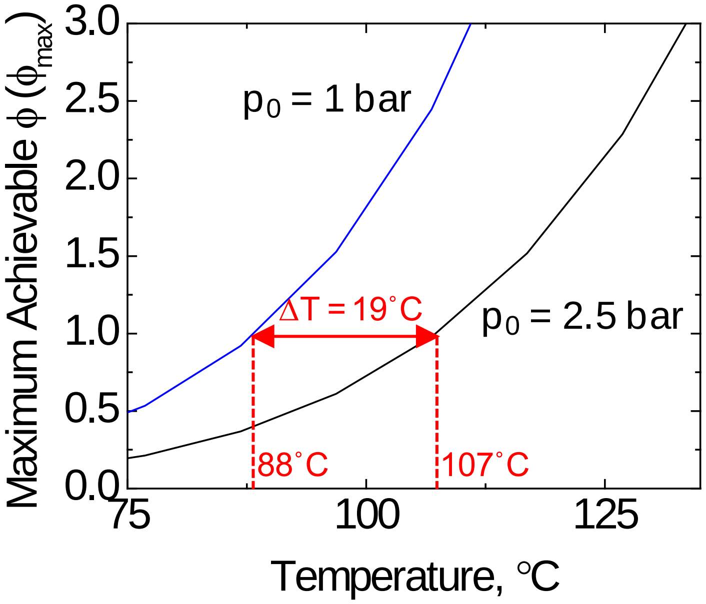

Figure 2-11. Comparison of initial temperature requirements for testing a given equivalence ratio at total mixture pressures of 1 bar and 2.5 bar.

Additionally, if the mixture is to be used for several tests, it must be created with a sufficiently high pressure to fill the test device multiple times which raises the minimum temperature requirement. For example, the creation of a stoichiometric mixture of *n*-dodecane in air with an initial pressure of 1 bar would require a minimum initial temperature of 88 °C for complete evaporation. However, the initial temperature requirement is raised substantially to 107 °C if the premixture is prepared at a total pressure of 2.5 bar in a separate vessel to be used for several tests. This disparity is illustrated in Figure 2-11, where the maximum achievable equivalence ratio is plotted as a function of initial premixture temperature for total mixture pressures of 1 bar and 2.5 bar. The ϕ_{max} curves in Figure 2-11 are generated by assuming the partial pressure of the fuel in the mixture is equivalent to the fuel saturation pressure for at a given initial temperature.

By preparing a unique premixture for each test directly in the test device rather than in a mixing vessel, several benefits can be realized. First, a premixture with a particular equivalence ratio may be prepared using a lower initial temperature to reduce concerns over fuel thermal decomposition. A second, and related benefit, is that premixtures of extremely non-volatile fuels (*e.g.*, alkyl esters from biodiesel) may be prepared directly in the test chamber which could not reasonably be created in a separate mixing vessel due to the higher initial temperatures and long mixing times. The final benefit of preparing the premixtures directly in the test chamber is that the separate heated mixing vessel and heated transfer lines may be removed from the experimental setup. The elimination of the heated tubing is of particular benefit because temperature can be difficult to control within the tubing and fuel condensation is always of concern. The experiments in this work have utilized this approach of creating the premixtures directly in the test chamber, and for convenience, we refer to this as the direct test chamber (DTC) charge preparation approach. The main obstacle to implementing the DTC approach is the ability to accurately load small amounts of fuel into the chamber. To address this challenge, we employ a fuel injector which loads fuel into the test chamber, as described in § 2.1.3.

2.2.1. Analysis of Fuel Evaporation and Fuel Mass Loading

Application of the DTC approach requires knowledge of the time required for the loaded fuel to fully evaporate. Prior to the making ignition delay measurements, we have probed the evolution of the gas-phase mixture after injecting a fuel sample into the chamber. The purposes of these tests are to (1) confirm all the components of the hydrocarbon fuel blend fully vaporize without any thermal decomposition or condensation, (2) to determine how long to wait before initiating a test once the fuel has been injected, and (3) to confirm fuel loading is consistent with expectations based on the injector calibration. The composition of the gas-phase mixture was investigated by drawing gas samples from the RCM which were analyzed using gas chromatography/mass spectrometry (GC/MS). Gas sampling is enabled in the RCM by machining a port through a stainless steel replica of the front window, depicted in Figure 2-6a, and attaching a compression fitting which contains a small septum. At a given time after injection of the fuel, a 10.0 mL gas sample was drawn through the septum and bubbled through a solvent to be used in the GC/MS analysis.

Fuel Evaporation

Samples of a JP-8 jet fuel and air mixture were drawn from the RCM to investigate the fuel evaporation process at an initial temperature of 135 °C. The fuel loading conditions for these tests corresponded to a stoichiometric premixture used for testing a compressed pressure of p_C = 20 bar, with a fuel partial pressure of 3.66 kPa. These conditions represent the highest fuel loading of any test in this study. The total ion chromatogram (TIC) results from these tests appear in Figure 2-12 where samples have been drawn from the RCM at 2, 4, and 8 minutes after

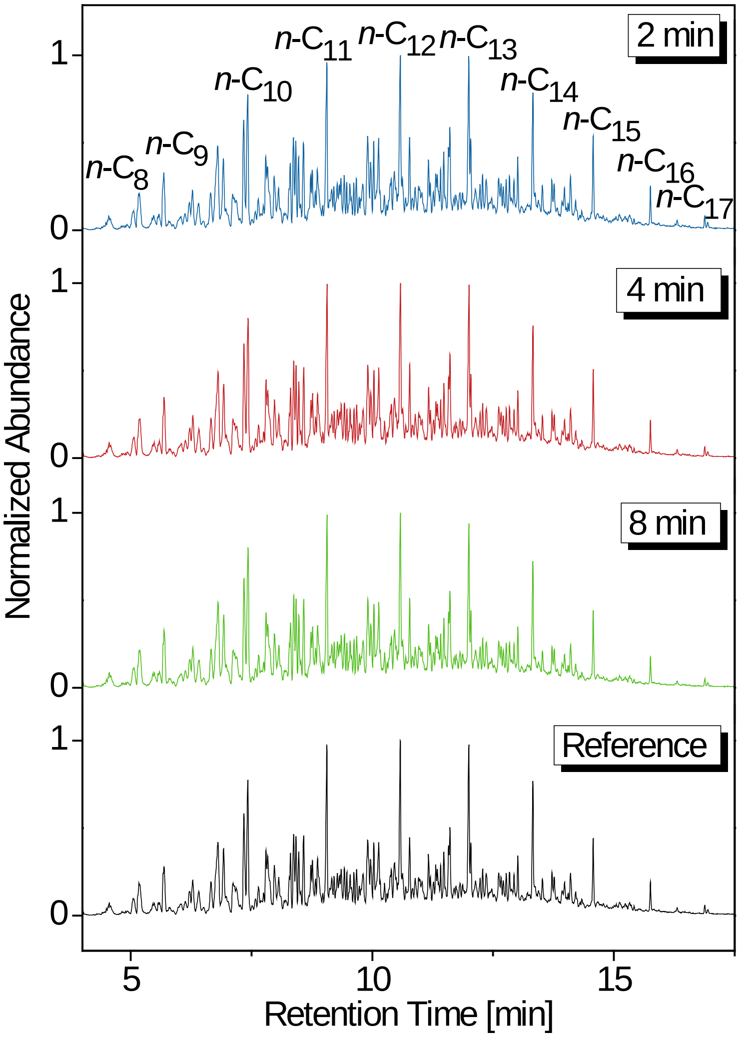

Figure 2-12. Normalized total ion chromatograms for a JP-8 reference sample and volatilized samples drawn from the RCM at 2, 4, and 8 minutes after injection (fuel partial pressure: 3.66 kPa).

injection. The TIC data is compared with a TIC reference created directly in the pentane solvent (1000 μg/ml) rather than being sampled from the RCM. To compensate for any concentration differences created during the sampling process, the abundances are normalized by the peak abundance for *n*-dodecane (*n*-C_{12}). The fuel sample is presumed to have completely evaporated when the relative peak sizes for each of the species matches that of the reference sample. Based on this criterion, the fuel sample appears to be totally evaporated at 2 – 4 minutes after injection.

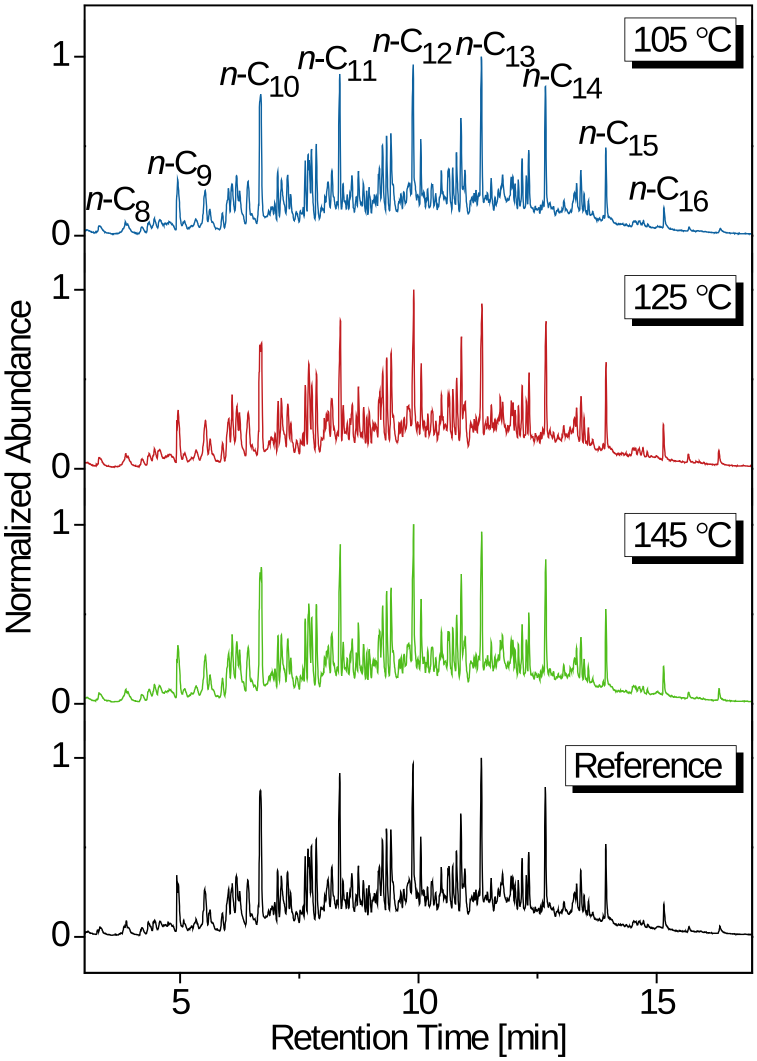

Figure 2-13. Normalized total ion chromatograms for a JP-8 reference sample and volatilized samples drawn from the RCM at 2 minutes after injection for initial temperatures of 105 °C, 125 °C, and 145 °C (fuel partial pressue: 1.25 kPa).

Additional JP-8/air samples were drawn from the RCM and analyzed with GC/MS for a lighter fuel loading case, corresponding to a fuel partial pressure of 1.25 kPa. For this test, samples were drawn at initial temperatures of 105 °C, 125 °C, and 145 °C to identify the minimum initial temperature required for total fuel evaporation. The relative peak sizes between the hydrocarbon components in Figure 2-13 are very consistent for all of the tested temperatures when compared to the reference JP-8 sample. This consistency indicates that all of the components are fully vaporizing, and that a homogeneous JP-8/air charge can be prepared in the

RCM using evaporation and mixing times as short as two minutes and at temperatures as low as 105 °C for a fuel partial pressure of 1.25 kPa. The data show no indication of preferential vaporization, thermal decomposition, or condensation. This is true even for the higher molecular weight alkanes, which are present in sufficiently small quantities so that evaporation occurs in a short period of time.

Fuel Mass Loading

The fuel injector calibration process described in § 2.1.3 provides a description of the expected fuel mass to be injected for a given pulse width. However, there are some anticipated sources of error during the calibration process that cannot be easily quantified, and which raise questions about the validity of the calibration:

- The calibration is performed in open air where some of the fuel may volatilize and not be registered on the scale. Does the volatilized sample significantly affect the calibration for fuels of interest (*e.g.*, jet fuels)?

- Each calibration run utilizes 100 or more pulses of the injector, while some of the DTC tests utilize as few as 2 injections. Can the behavior of the injector over so few pulses be accurately represented by the calibration curve made with so many injection pulses?

- The injectors are calibrated at ambient conditions, while the injector experiences elevated temperatures during tests in spite of the cooling applied to the injector body. Does the heating alter the behavior of the injector or influence the physical properties of the fuel (*e.g.*, viscosity) so as to make the calibration invalid?

In consideration of these potential sources of error, a strategy was devised for investigating the fuel mass loading in the RCM. The approach rests on first accepting that the

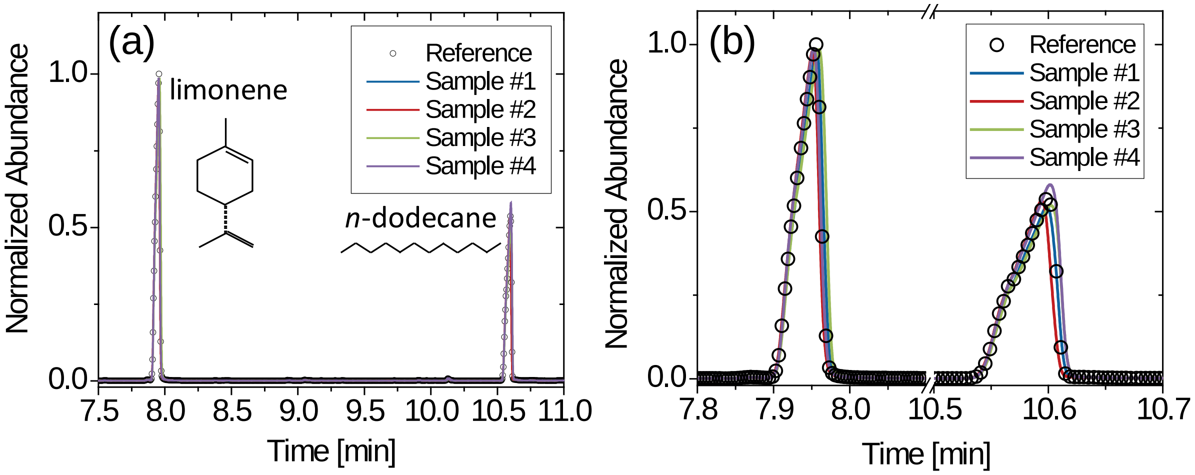

Figure 2-14. Total ion chromatogram data for blends of limonene and *n*-dodecane to investigate the fuel mass loading in the RCM.

fuel is totally evaporated for a given test condition, which has been established in the previous section. The tests begin by establishing a standard mixture of the two hydrocarbon components, *n*-dodecane ($C_{12}H_{26}$, 170.33 g/mol) and limonene ($C_{10}H_{16}$, 136.24 g/mol) in a 1:1 volume ratio. A small volume (20 μl) of this standard mixture is injected with a syringe through the septum that is typically used only for sampling, and 2 minutes is provided for total evaporation. After this evaporation period, a sample is drawn from the RCM and analyzed with GC/MS. The ratio of integrated peak area in the TIC data for the two hydrocarbon components is indicative of the 1:1 volume ratio prepared for the standard mixture. In subsequent tests, only limonene (10 μl) is loaded into the RCM via the syringe, and the *n*-dodecane (10 μl) is loaded into the RCM using the fuel injector. Samples are drawn from the RCM after 2 minutes and analyzed with GC/MS. The TIC data is compared with the standard reference to confirm that the ratio of integrated peak areas for the two species matches the ratio observed for the standard reference. The results of this comparison appear in Figure 2-14, where the reference data is overlaid with data from 4 unique tests. The data in Figure 2-14a clearly show the two distinct peaks for limonene and *n*-dodecane

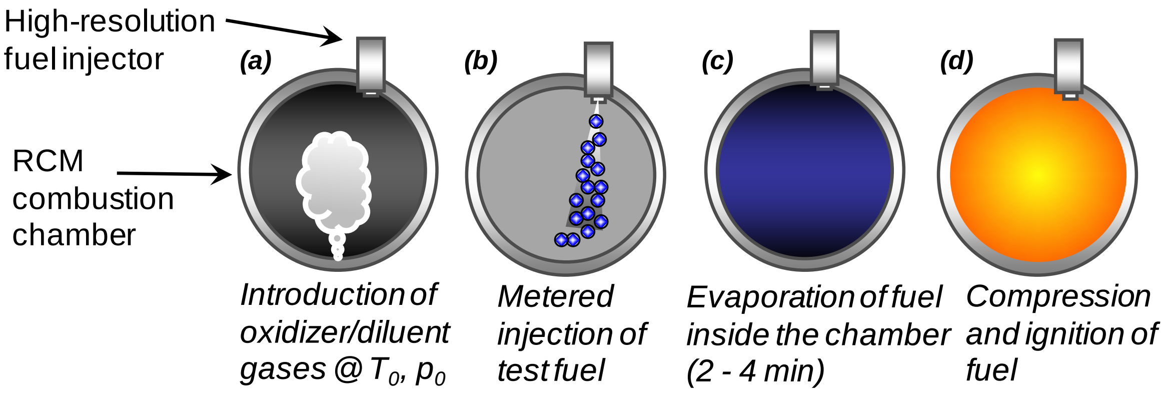

Figure 2-15. Protocol for preparing a reactive charge with the DTC approach..

without any evidence of fuel decomposition. More importantly, Figure 2-14b illustrates that the injected mass of *n*-dodecane closely follows that of the reference. This result indicates that the actual mass loaded by the injector matches the description of the injector calibration curve.

It should be noted that only 3 injection pulses were required to load 10 μl of *n*-dodecane into the RCM, which is a fair representation of the lightest fuel loading tests presented in this work where 2 injections were needed. It is expected that the fuel mass loading best reproduces the calibration behavior with increasing number of pulses, and that this data represents the worst case scenario.

2.2.2. Test Protocol

Based on these results of the charge characterization presented in § 2.2.1, the reactive charges are prepared in the following manner, as depicted in Figure 2-15. The test chamber is evacuated to sub-Torr pressures using a vacuum pump. The oxidizer and diluent gases are subsequently added manometrically to the test chamber (Figure 2-15a), and the inlet valve is closed to isolate the contents. At this time, the fuel injector is actuated to deliver a particular fuel mass (Figure 2-15b). The fuel is provided approximately 2 - 4 minutes for evaporation and mixing (Figure 2-15c), depending on the amount of fuel loaded. After the evaporation period, the test is commenced by compressing the charge to elevated temperatures and pressures (Figure 2-15d).

2.3. Spray Ignition Mode

2.3.1. Hybrid Approach to Generating Test Conditions

Autoignition delay time tests in RCMs have conventionally used three approaches to altering the compressed temperature: (1) changes to the initial temperature, (2) alteration of the compression ratio, and/or (3) changes to the mixture specific heat by altering the diluent gas composition. The spray ignition tests conducted as part of this work use a hybrid approach to generating the test temperatures. The compressed temperature is set by changing the diluent gas composition and by varying the post-compression cooling time before commencing the fuel spray. This approach is illustrated in Figure 2-16, where tests for four different compressed

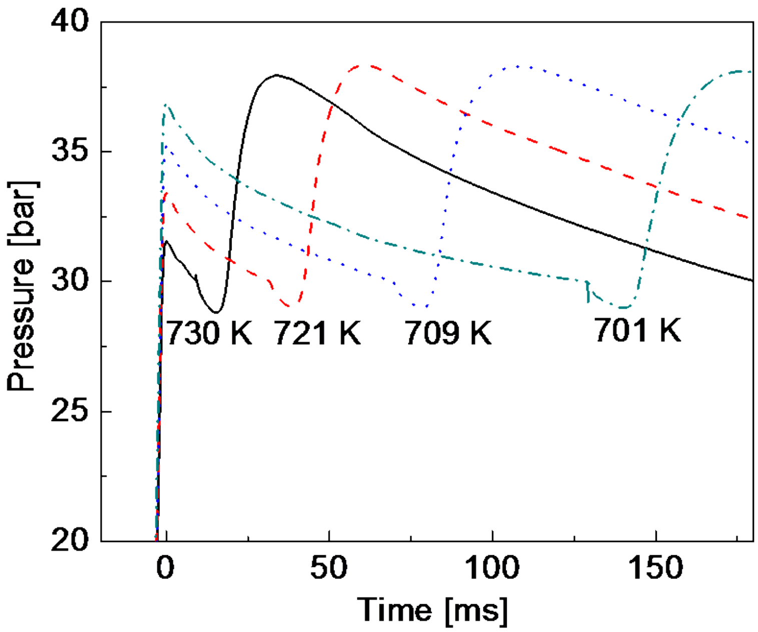

Figure 2-16. A sample set of reactive pressure history curves (canola biodiesel, 12% O_2) that illustrate the injection timing approach that is used to generate the desired test temperatures. Each curve is marked with the calculated gas temperature at the time of injection.

temperatures are conducted using a single gas mixture and a single compression ratio. The temperatures describing each pressure curve in Figure 2-16 are adiabatic core temperatures, and have been calculated using the effective volume approach described by Tanaka et al. [16] and by Mittal and Sung [1]. These core temperatures are considered valid up to the time of injection. The initial pressures for the tests are determined in advance to yield the desired compressed temperature when the cylinder pressure reaches 30 bar during cooling.

2.3.2. Assessment of Test Approach

Many studies in the literature have been devoted to characterizing the adiabatic core region of gas that can be generated in RCMs [21-22,11,23-24,15,25-26]. One focus of these studies has been to identify the spatial extent and temporal duration over which the core conditions prevail before degenerating due to convective and diffusive transport. A brief review of these studies is relevant because of the approach used in this study, where core conditions form the basis for characterizing the gas temperature up to 140 ms after the end of compression. It is important to know if the adiabatic core temperature calculations may be considered valid at such post-compression times where they serve as an input to estimate the temperature of the reactive charge after the fuel spray has evaporated. The review will be limited to studies that have employed a creviced piston, as in the RCM described in this paper. Creviced pistons are known to suppress vortex formation during compression, and thereby improve the persistence and spatial extent of core conditions in the RCM [24,15,25]. This is a critical feature in our study because it promotes the viability of core temperature calculations long after the end of compression.

The machining of a crevice around the periphery of a RCM piston crown was first proposed by Park and Keck [27]. A preliminary comparison with a flat piston (*i.e.*, no crevice) demonstrated that the crevice did reduce the rate of heat transfer to the test chamber walls and make the compression more isentropic in nature. However, no calculations or measurements were presented to characterize the temperature or velocity fields in the core. Subsequent studies by Lee and Hochgreb [24] and Würmel and Simmie [26] were each concerned with crevice optimization for a particular RCM. Computational fluid dynamics (CFD) model results reported in each of these studies indicated that the extent of the core region is augmented significantly by the presence of a piston crevice. Yet, results were only presented for relatively short post-compression times (< 30 ms). A more complete set of experimental and numerical results were reported by Mittal and Sung [15] in their study of post-compression temperature and velocity fields generated by creviced and flat pistons. Measurements using acetone planar laser-induced fluorescence (PLIF) sought to identify the time at which core gas temperatures were reduced due to mixing with the roll-up vortex. Tests indicated that temperature uniformity across the core is a function of the compressed pressure, p_C, and that the degree of uniformity may be greatly enhanced for tests at p_C = 39.5 bar relative to tests at p_C = 11.95 bar. For the tests at p_C = 39.5 bar, no core temperature inhomogeneity was observed at 114 ms post-compression; and even at 200 ms post-compression, only a 40 K temperature reduction was observed near the central axis with much of the core gas remaining homogeneous in temperature. CFD model results for laminar conditions and a compressed pressure of 39.9 bar suggest that the core gas region extends over 70 % of the test chamber at 120 ms post-compression. Donovan et al. [28] published a characterization study of a RCM with a unique sabot piston design that is capable of promoting core gas formation in a manner similar to a creviced piston. Fine-wire thermocouple measurements were recorded at multiple radial and axial locations to identify the boundaries of the adiabatic core. By defining the core region to exist anywhere the temperature surpassed 90 %

of the peak measured temperature, Donovan et al. [28] estimated that the core region covered 50 % of the test gas volume. This estimate appears to be valid up to 50 ms post-compression. It is unclear from the work of Donovan et al. [28] how the core volume is diminished for post-compression times longer than 50 ms.

Although different RCMs typically exhibit unique heat loss and boundary layer suppression characteristics, it should be emphasized that the piston, crevice, and bore designs used for the RCM in this work are identical to the design of Mittal and Sung [1]. We therefore give high regard to their previously described crevice optimization study [15] because we expect the results may apply similarly to our RCM. Upon a more careful examination of these experimental results it is seen that the temporal evolution of the core gas region is not clearly defined for post-compression times between 114 ms and 200 ms. For these two post-compression times where temperatures are measured, two considerations are noted in the broader context of this publication:

- The homogeneity and radial extent of the core gas reported at 114 ms post-compression is adequate for testing the spray ignition delays in the manner proposed in this paper. However, the experimental and numerical results both demonstrate that a reduction in compressed pressure leads to temperature inhomogeneities at earlier post-compression times. The extent and lifetime of the core gas region for compressed pressures of 30 bar cannot be accurately known using the results of Mittal and Sung [15].

- The core gas temperature inhomogeneity that appears in the measurement at 200 ms post-compression (p_c = 39.5 bar) is estimated to be 40 K. This magnitude of variation is unacceptable for measuring high-fidelity gas phase ignition delay data. However, it is possible that spray ignition delay measurements will not be significantly affected by this level of localized temperature variation. This is hypothesized because the fuel spray has significant momentum as it leaves the injector, and the radial spray geometry drives a mixing process that may reduce locally confined temperature variations of this magnitude in the core region.

Given these considerations, it is prudent to investigate the effect of injection timing on the ignition delay, as an unambiguous confirmation of the test approach. To do so, five different test gas mixtures were created with varying nitrogen:argon ratios. Each mixture required a unique post-compression cooling time to reach the desired compressed temperature of 727 ± 2 K. The reaction zone temperatures for these tests are 708 ± 1 K. The procedure for this calculation is presented subsequently in § 4.4.1. The raw pressure history data for these tests appear in

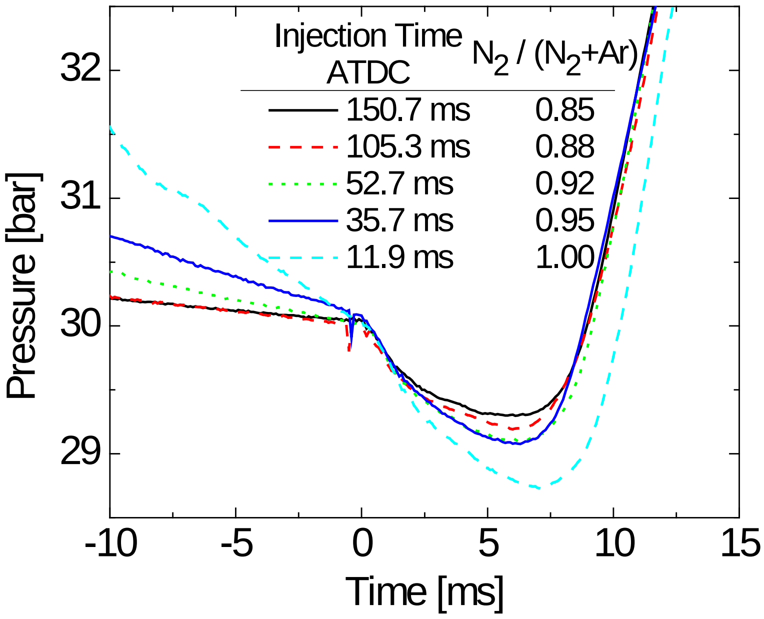

Figure 2-17. Pressure history data for canola biodiesel ignition which illustrates the independence of the ignition delay from injection timing. Injections occurred at a unique time for each test, but with similar compressed temperatures (727 ± 2 K) for all tests.

Figure 2-17, where time $t = 0$ corresponds to the injection event. The pressure loss that occurs prior to $t = 0$ is a result of charge gas cooling, and it is clearly seen that the injection accelerates the pressure loss as energy is absorbed by the fuel spray for heating and vaporization. The timing of the ensuing pressure rise due to ignition is nearly identical for injection times of $t_{inj} \geq 35.7$ ms. For the $t_{inj} = 11.9$ ms case, the ignition appears to happen more slowly than for other cases, which is an unexpected result because the extent of the core region should be at a maximum for this test. However, it can be seen that the pre-injection pressure loss is much more rapid for this test than for the others, which can be attributed to increased gas velocities within the test chamber at such an early post-compression time. The increased charge motion enhances heat transfer to the walls, and during the ignition event, a larger amount of fuel energy must be released to overcome these losses before the pressure begins to rise.

Two ignition delay periods are used to characterize the ignition process in this study. When using the appropriate definitions in § 4.4.2, the first and total ignition delay periods are repeatable to within 8 % and 7 %, respectively, for the tests shown in Figure 2-17. The authors note that ignition delay measurements using a prevaporized charge in a RCM typically exhibit repeatability between 2 – 5 % [29,1,30]. These are fundamentally different types of measurements, but the comparison is indicative of the level of repeatability that is observed using more established test methods. On this basis, the proposed test approach is used to measure the ignition delays for sprays that occur up to 140 ms after the end of compression.

2.3.3. Test Protocol

The spray ignition tests begin by first evacuating the combustion chamber using a vacuum pump, and subsequently filling the chamber with the oxidizer and diluent gas mixture to the required initial pressure. The gas mixture is subsequently compressed before spraying a known quantity of fuel into test chamber once the desired conditions are achieved. The timing and duration of the fuel spray is controlled by a LabView VI. During compression, the VI monitors and records voltage data from the piezoelectric pressure transducer and charge amplifier setup. Once the pressure reaches a given threshold, a hardware trigger is activated which the VI considers to be at time $t = 0$. The piston reaches TDC some time later (~ 8 ms). The exact time of piston arrival at TDC is known accurately from a calibration procedure performed for each unique test condition. Timing for the start of injection (SOI) may be set in the VI to take place anywhere after the trigger occurs with resolution on the order of 10 microseconds. All tests reported in this study set the SOI to occur at some time delay after TDC (ATDC).

2.4. Aerosol Wet-Compression Mode

Traditional RCM designs are intended to gather chemical kinetic data by compression-igniting a homogeneous premixed charge. In this work, we sought to develop a versatile RCM capable of burning neat aerosol fuels and heterogeneous mixtures for the purpose of investigating advanced combustion concepts, including energetic-nanoparticle-enhanced combustion.

2.4.1. Optimization of Poppet Valve Design and Operation

Poppet Valve Optimization with CFD Simulations

In a RCM ignition test, establishing a uniform charge is of critical importance for taking accurate, repeatable measurements. In a premixed vapor test, the test charge is allowed to homogenize in the combustion chamber before compression begins. In an aerosol test, a gas and aerosol flow moves through the combustion chamber until the inlet (poppet) and outlet valves are

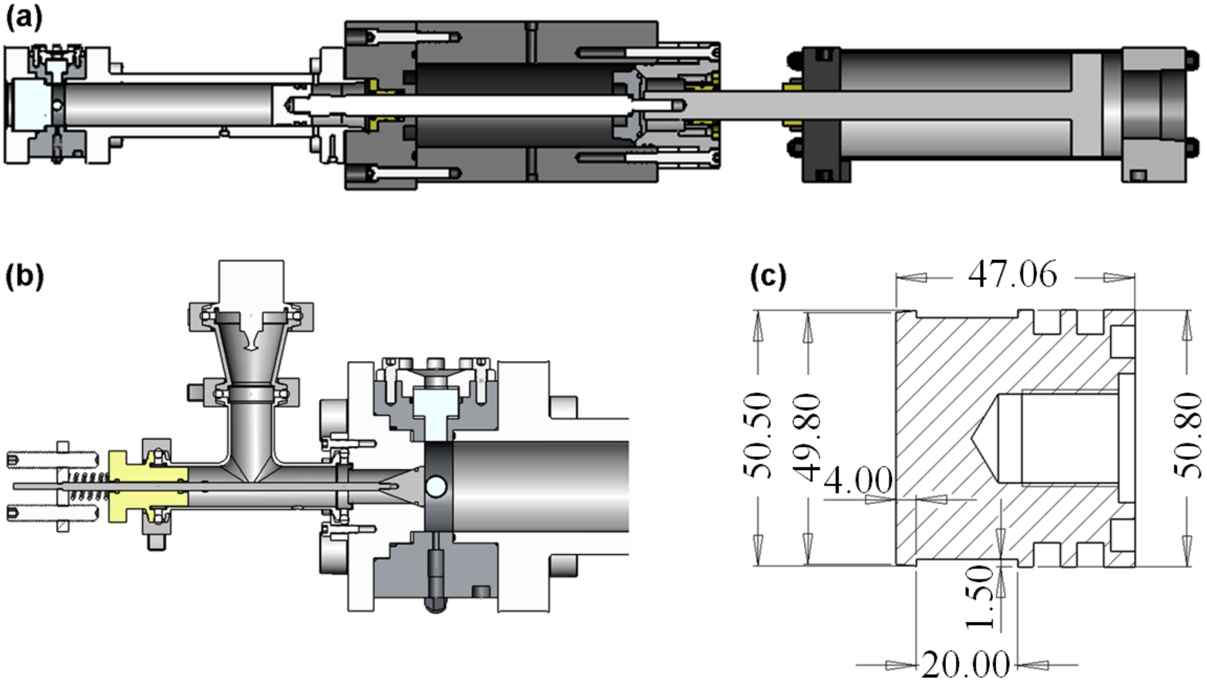

Figure 2-18. RCM schematics. (a) Overall RCM schematic depicting combustion chamber, hydraulic chamber and pneumatic chamber; (b) Aerosol unit that may replace end window and flange in overall setup; (c) creviced piston with dimensions (in millimeters) [1].

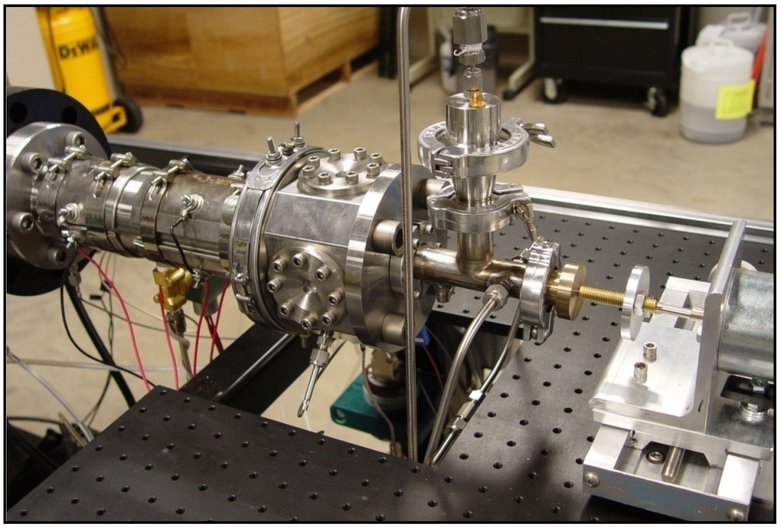

Figure 2-19. Photograph of the aerosol RCM experimental setup.

closed just prior to the start of compression. The location of these valves and the gas inlets are identified in Figures 2-18 and 2-19. Establishment of a uniformly distributed aerosol charge relies on turbulent mixing of the gas and aerosol as the aerosol-laden gas flow moves past the poppet valve. Given this consideration, CFD analysis using STAR-CCM+ was carried out to compare the turbulent swirling generated by airflow through the valve opening. The intent of the model was to provide high-level guidance for the design of the poppet valve, and the presence of the aerosol was not considered for the simulations. A two-dimensional grid was generated for each poppet valve design with higher mesh density near the poppet valve. Grid independence was confirmed in tests with an increased mesh density. For the tested models, increasing the mesh density led to only modest changes in peak velocity (< 1 %). The simulations employed the k-ε turbulence model and no-slip boundary conditions were specified on all walls. Steady-state solutions were achieved for each model using an inlet velocity of 0.33 m/s.

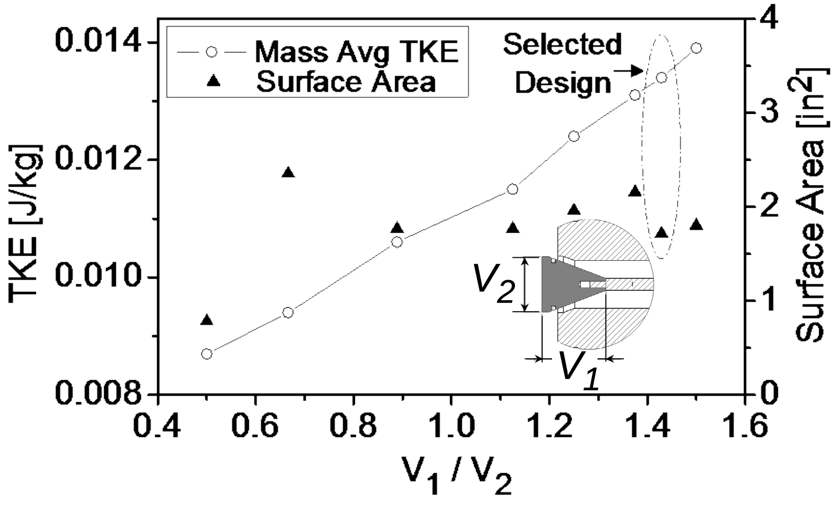

Figure 2-20. The mass-averaged turbulent kinetic energy and surface area for candidate poppet valve designs. The selected design (V_1 / V_2 = 1.43) is highlighted. The inset image displays the poppet valve head and stem. The shaded area of the poppet head corresponds to the surface area used to compare valve designs.

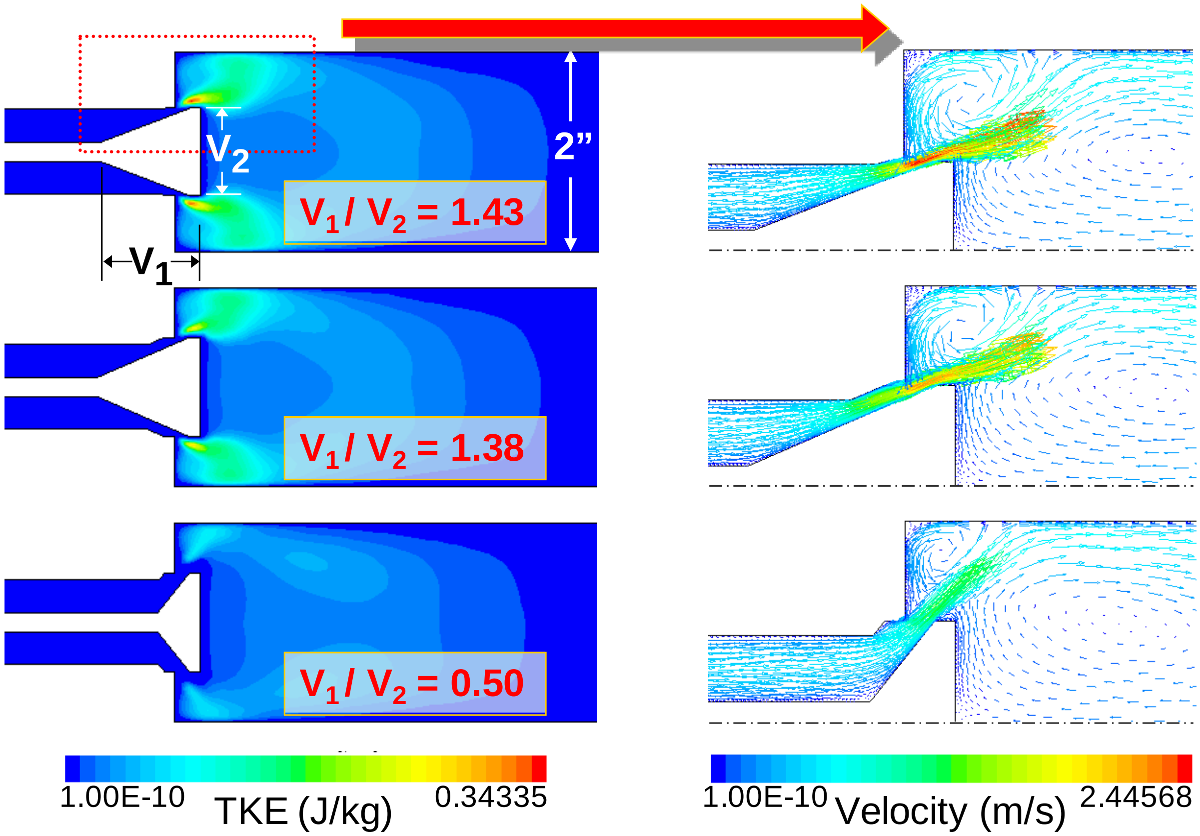

Figure 2-21. TKE fields and velocity vectors for flow fields generated by candidate poppet valves.

Preliminary analysis of the poppet valve system identified two key design variables that contributed strongly to swirling flow in the combustion chamber. Figure 2-20 depicts these dimensions as V_1 and V_2. Simulations were conducted for different combinations of V_1 and V_2 and the results were evaluated using two design criteria: (1) the poppet valve should maximize turbulent swirl as measured by mass averaged turbulent kinetic energy (TKE); and (2) the poppet valve design should minimize the surface area where the impinging aerosol may settle out of the flow. The surface area we considered corresponds to the posterior side of the poppet valve, represented by the shaded surface of the inset poppet valve image in Figure 2-20. The TKE provided a scalar quantity to measure the relative strength of eddies in the flow and was used as a basis to compare turbulent swirl for different poppet valve designs. Figure 2-20 summarizes the

TKE values for an array of V_1/V_2 values, each with a poppet valve opening distance of 0.25 in. Additional simulations with changes to the opening distance exhibited the same trend shown in Figure 2-20, of increasing mass averaged TKE values with increases in V_1/V_2. The optimum opening distance was determined experimentally through a light scattering experiment that is subsequently described. The simulations led to selection of the poppet valve design with V_1/V_2 = 1.43. This model is marked in Figure 2-20, and it can be seen the model has a comparatively large TKE value (0.0134 J/kg) and a relative minimum for surface area (1.718 in^2).

Figure 2-21 displays the TKE field near the poppet valve for three candidate designs, including the selected design (V_1/V_2 = 1.43). The figure also describes the region of focus for which velocity vectors are presented. The flow fields clearly depict the swirling motion generated as the flow emerges from the poppet valve, and that the intensity of the motion is greatly enhanced for the selected design relative to the other candidates. The steady-state solution presented here cannot capture the inherently unsteady nature of the turbulence and vortex shedding; however, the models are sufficient when comparing relative swirling motion as a design criterion for the poppet valve.

Poppet Valve Opening Distance Optimization

The CFD simulations identified the poppet valve design for maximizing turbulence in the combustion chamber, but gave no direct indication of the overall aerosol distribution uniformity in the combustion chamber or the optimized poppet opening distance. We qualitatively addressed these questions by directing a laser light sheet (8 mW He-Ne) through an aerosol flow and imaging the light scattered by the aerosol droplets for three different opening distances: 1/8”,

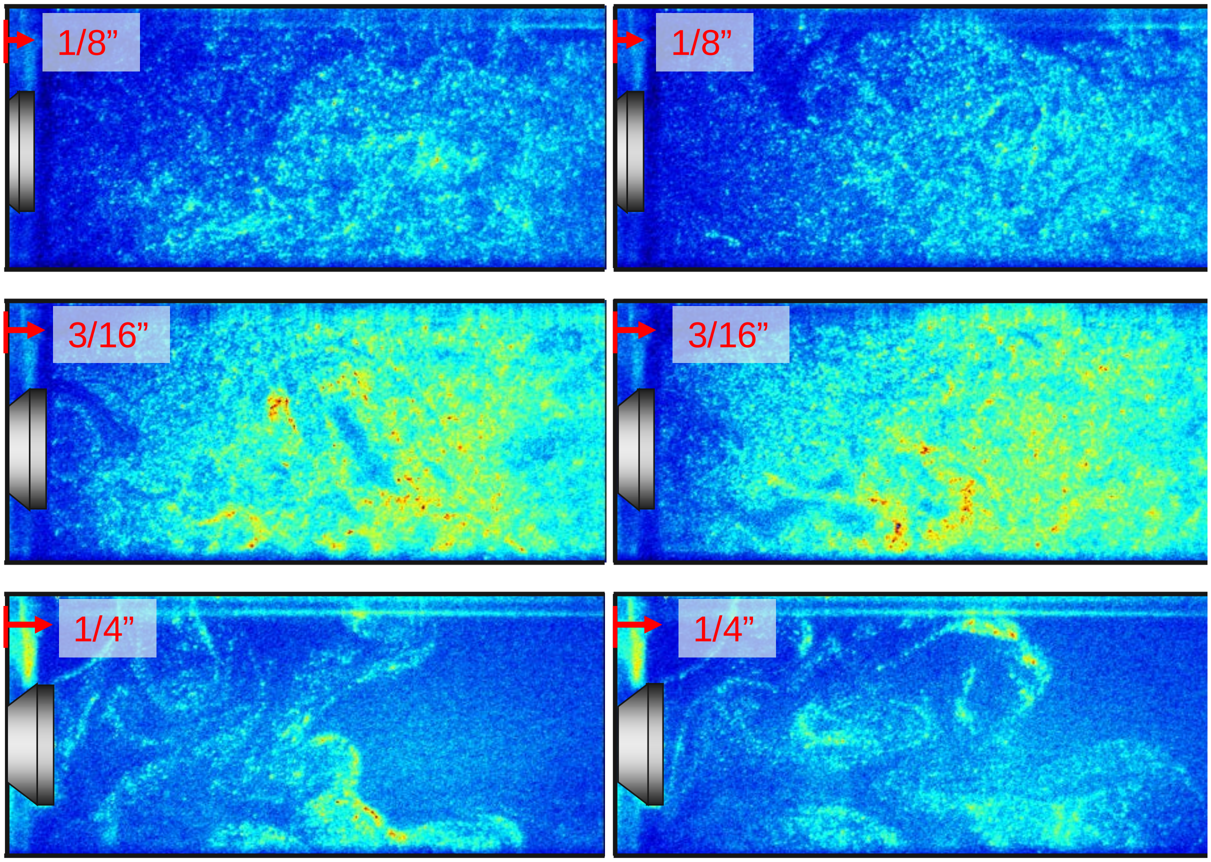

Figure 2-22. ICCD camera images of laser light scattered from aerosol droplets in a glass tube. Two representative images appear for each poppet valve opening distance.

3/16” and 1/4”. The poppet valve assembly was attached to a glass tube for optical access, and the light sheet was directed vertically through the center plane of the glass tube. All of the tests were conducted with aerosol flow rates 0.15 kg/hr and air flow rates of 10 SCFH, corresponding to a flow velocity of 0.28 m/s.

Figure 2-22 shows two representative images for each of the opening distances tested. The image for the 1/4” opening distance clearly shows the aerosol droplets are entrained in the turbulent eddies, but the droplets are not uniformly distributed in the plane. By reducing the opening distance to 3/16”, we observed light scattering from a large portion of the imaged plane, indicating a more uniform distribution of aerosol in the chamber. Reducing the opening to 1/8” also showed light scattering from a larger portion of the imaged plane when compared to the 1/4” opening distance. However, the scattered light intensity decreased for the 1/8” opening distance when compared to a 3/16” opening. We suspect this occurs because more aerosol droplets settle on the back of the poppet valve for the 1/8” opening distance thus reducing the aerosol loading in the chamber. The tests determined that a 3/16” opening distance maximized droplet loading and uniformity of aerosol distribution. Based on this conclusion, all aerosol ignition tests in the RCM were performed with a 3/16” poppet opening distance. Tests to quantify aerosol loading in the chamber have been carried out separately.

2.4.2. Test Protocol

Aerosol test charges are prepared in a continuous flow operation. With the piston in a fully-retracted position, the poppet valve and outlet valve are opened and the chamber is purged with air for several minutes. After the purging period, the initial test pressure is established by throttling the flow to the vacuum pump, and aerosol generation begins. The aerosol is generated by a Sono-Tek 120 kHz ultrasonic nozzle which is capable of generating an 18 μm median droplet diameter for water with a flow rate of 3 – 5 in/s. The nozzle is positioned downstream of the flow, and the aerosol is carried into the chamber by the incoming flow. A syringe pump (Fisher Scientific, 14-831-200) delivers liquid to the nozzle at a constant rate of 30 mL/hour for all tests, and the aerosol filling proceeds for a prescribed time to achieve a given bulk equivalence ratio. During the filling period, the piston is balanced in the retracted position through intense pressure in the hydraulic chamber and pneumatic chamber. The sudden relief of pressure in the hydraulic chamber causes the piston to lunge forward, dramatically increasing the temperature and pressure to conditions where the fuel aerosol is vaporized and autoignition occurs.

2.5. Kinetic Modeling of Rapid Compression Machine Data

2.5.1. Specification of the Effective Volume

Kinetic modeling of rapid compression machine data is an important step for comparing experimental results with kinetic predictions to check the viability and accuracy of the kinetic models. For the purposes of this work, the kinetic models have been used with proposed jet fuel surrogates to assess their ability to reproduce the observed ignition behavior. An essential element of this modeling is the specification of an effective volume profile that accounts for the heat losses from the RCM test chamber during compression and the post-compression period. The approach for specifying the effective volume profile has been published in previous work, and is summarized here.

The creviced piston in the RCM is employed to swallow the roll-up vortex formed at the periphery of the chamber during the compression and to support the validity of the adiabatic core hypothesis [27]. According to this hypothesis, heat losses from the RCM are restricted to a thin boundary layer at the chamber walls, and the gas core within the test chamber undergoes adiabatic compression. The heat losses lead to an overall reduction in measured cylinder pressure relative to a charge undergoing truly adiabatic compression, and serve as a global indicator of the non-adiabaticity of the compression. Under this assumption, the measured pressure (p_C), initial pressure (p_0) and known initial volume (V_0) can be used to calculate the effective volume profile (V_{eff}) up to the end of compression as

$$\int_{p_0}^{p_c} \frac{1}{\gamma} \frac{dp}{p} = ln \frac{V_{eff}}{V_0}. \tag{2-1}$$

The effective volume profile calculations depend on the specific heat ratio (γ), which can be calculated using temperature-dependent thermophysical property data [31]. The compressed

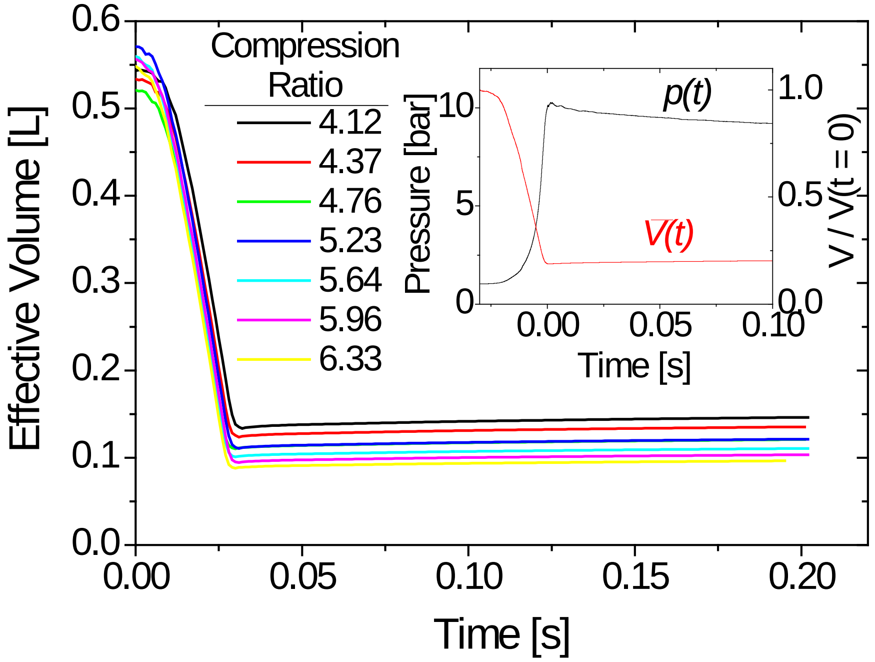

Figure 2-23. Sample effective volume profiles. Inset compares an effective volume profile with the corresponding pressure data over the same time interval.

temperature (T_c) needed as input for these calculations may also be calculated numerically using a second adiabatic compression relationship,

$$\int_{T_0}^{T_c} \frac{\gamma}{\gamma - 1} \frac{dT}{T} = ln \frac{p_c}{p_0}, \tag{2-2}$$

where T_0 is the initial charge temperature. Once the piston reaches TDC, it is locked in place by the excess pneumatic pressure acting on the back of the piston assembly. The effective volume during the post-compression period is modeled as an adiabatic expansion process, yielding a time (t) dependent volume expansion profile (v_{exp}) as

$$v_{exp}(t) = \left(\frac{p(0)}{p(t)}\right)^{1/\gamma} \tag{2-3}$$

where $t = 0$ corresponds to TDC. The experimentally-derived volume expansion profile is fitted with a polynomial function (v_p) to eliminate unwanted disturbances in the volume profile that arise from noise in the data. The effective volume calculated at TDC, $V_{eff}(0)$, is coupled with the polynomial fit to calculate the time-dependent effective volume after TDC as

$$V_{eff}(t) = V_{eff}(0) \cdot v_p(t). \tag{2-4}$$

The outlined approach has been used to calculate all of the effective volume profiles used for modeling purposes in this work. Seven of these calculated profiles appear in Figure 2-23, each for a unique compression ratio. The profiles show the rapid change in volume during the

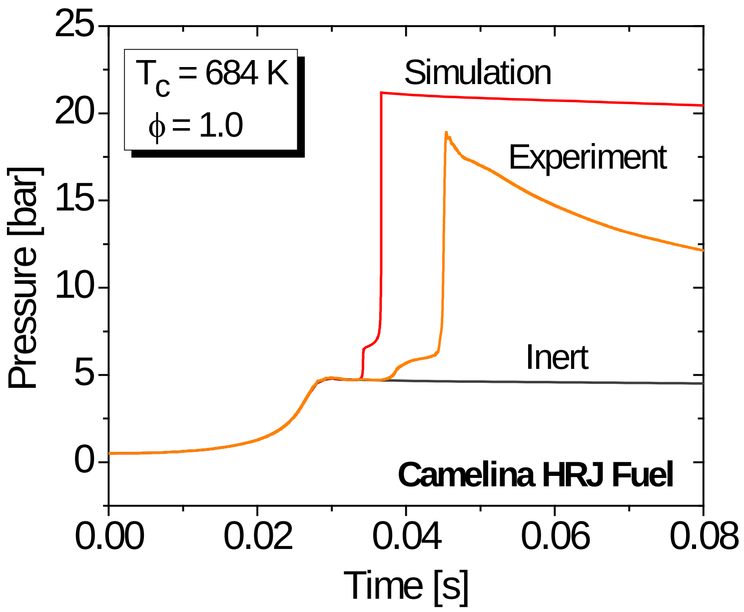

Figure 2-24. Comparison of the pressure evolution for a reactive experiment, an inert test used to create an effective volume profile, and a kinetic simulation based on the effective volume profile.

compression process leading up to TDC. Once the piston arrives at TDC, there is a slow volume expansion process as additional heat is lost to the surroundings. The inset of Figure 2-23 displays a normalized volume profile and the pressure data in the corresponding time interval. The heat loss in the post-compression period is evident by the loss in pressure that occurs after TDC.

Due to the evolving reaction and conditions in a RCM test, a reactive test cannot be used to create an effective volume profile. Instead, the effective volume profile for a given test must be created by running a separate inert test in which all of the oxygen is replaced by nitrogen. All other conditions of the inert test mimic those of the reactive test. The effective volume profiles calculated in this manner are used as input to the kinetic simulations where the energy equation is solved for each instant in time. Sample kinetic modeling results appear in Figure 2-24 where they are compared with experimental data and the inert trial used to construct the effective volume profile. The data and simulation predictions are results obtained as part of the bio-synthetic jet fuel study presented in Chapter 3. The data clearly demonstrate that the heat loss characteristics of the inert case (no oxygen) reflect the heat loss behavior for the reactive experimental test.

2.5.2. Chemical Kinetics Software Packages

The chemical kinetics simulations conducted as part of this work have been completed in CHEMKIN 4.1, CHEMKIN PRO, or Cantera 1.8. The CHEMKIN software packages are commercially-sold by Reaction Design, and offer many prepackaged reactor models that are intended for simulating specific burner geometries or idealized flow conditions. CHEMKIN is the *de facto* standard for conducting gas phase kinetic simulations and published mechanisms and thermodynamic data are often published in a format amenable to being used as CHEMKIN input. Simulations of the RCM utilize the *Closed Homogeneous Reactor* model by specifying the initial conditions of the test and by supplying the effective volume profile used to constrain the volume of the reactor. CHEMKIN solves the energy equation over a specified time interval to calculate system temperatures, pressure, and species concentrations.

Cantera 1.8 is a powerful, open-source software package for simulating chemical kinetic phenomena. The Cantera object-oriented framework is flexible, easily modified, and may be called from codes written in Fortran, C++, Python, and MATLAB. Cantera is equipped with a built-in internal combustion engine model which accepts a polynomial function to describe piston velocity. The Cantera simulations conducted in this work have used effective volume profiles to calculate the RCM piston velocity as described by Mittal [13]. The calculated velocity profile serves as a basis for fitting a high-order polynomial describing the piston velocity, which is used with Cantera to describe the motion of the RCM piston during the kinetic simulation. The appendix includes Python codes developed to calculate and fit the piston velocity profile based on effective volume data (*pistonVelociy.py*), and to conduct a kinetic simulation in Cantera using the polynomial input (*jp8_ranzi.py*).

2.5.3. Surrogate Fuels

Simulating the ignition kinetics of jet fuels and other complex fuel blends is a challenge because the fuels are comprised of numerous and often unquantified hydrocarbon components. For practical purposes, it is highly desirable to develop a surrogate fuel with a limited number of components that reproduces the global ignition behavior of the fuel. Once identified, the surrogate fuel may be integrated with large-scale CFD simulations to obtain predictions of the real fuel behavior.

Surrogate jet fuels are investigated in this work for their ability to reproduce the ignition behavior of real conventional and alternative jet fuels. The surrogate fuel components and the corresponding kinetic mechanisms for these simulations are summarized in Table 2-1.

Table 2-1. Jet fuel surrogates and mechanisms tested in this work

Jet Fuel	Surrogate Components		Scope of Test
Jet-A	*n*-dodecane *iso*-octane *n*-propylbenzene 1,3,5-trimethylbenzene	40.41 % 29.48 % 22.83 % 7.28 %	Physical surrogate tested in RCM, no chemical kinetic simulation.
JP-8	*n*-dodecane *iso*-octane toluene methycyclohexane benzene	73.5 % 5.5 % 10.0 % 10.0 % 1.0 %	Mechanism: Ranzi et al. [32], selected due to ability to predict NTC behavior as described by Vasu et al. [33].
Camelina HRJ & Tallow HRJ	2-methylundecane *n*-dodecane	90. 0 % 10.0 %	Mechanism: Sarathy et al. [34], selected because only known mechanism that can accommodate high molecular weight branched alkanes

Chapter 3:

IGNITION CHARACTERISTICS OF CONVENTIONAL AND BIO-DERIVED JET FUELS

3.1. Introduction & Background

Major initiatives are underway in the U.S. to reduce reliance of foreign energy sources. These initiatives are primarily focused on the transportation sector, and often seek to replace conventional petroleum-based fuels with alternative fuels. Military logistics are a major component of these initiatives, and due to the large volume of jet fuel consumed annually by the U.S. Department of Defense, provide an excellent opportunity to displace a significant portion of conventional fuel consumption. In FY09, the Department of Defense consumed 3.9 billion gallons of jet fuel at a cost $7.3 billion [35]. Approximately 64 % of this fuel was consumed by the U.S. Air Force (USAF) [36]. Jet fuel has traditionally been refined from petroleum, largely from foreign sources, and the USAF recognizes the potential benefits that may be realized by replacing conventional jet fuel with alternative, domestically-produced fuels. To this end, the USAF is certifying the existing aircraft fleet to use 50:50 blends of JP-8 with synthetic jet fuel (Fischer-Tropsch-derived, S-8), and is conducting tests to use blends that would include bio-derived jet fuel. The USAF is currently procuring hydrotreated (hydroprocessed) renewable jet (HRJ) fuels created by hydroprocessing a biological feedstock of either camelina seed oil or tallow. These HRJ fuels, also referred to as bio-synthetic paraffinic kerosene (bio-SPK) or hydroprocessed esters and fatty acids (HEFA), are characterized by their high ratio of branched to normal paraffins and by their lack of aromatics and oxygenated compounds and limited cycloparaffins.

The certification of a new fuel for full-scale deployment requires extensive testing and modeling work which rely on kinetic models describing the chemical reactivity of a fuel under a broad range of test conditions. Ignition delay measurements which support these models are ideally obtained in premixed systems, and the most commonly used devices to obtain these data are rapid compression machines and shock tubes. However, there is a lack of this type of fundamental data to support and validate kinetic mechanisms, largely because of challenges in forming a premixed charge of non-volatile fuels (*i.e.*, conventional and alternative jet fuels), in these test devices. The creation of a premixed fuel and air charge for these fuels requires preheating of the fuel to vaporize all of the components. However, the heat must be carefully applied to the system because excessive temperatures lead to concerns regarding thermal decomposition of the fuel, especially for high molecular weight compounds. The risk of decomposition is increased by the conventional use of a mixing vessel which is heated for several hours during batch premixture preparation and testing. These limitations have thus far prohibited ignition delay measurements for high molecular weight fuels (*e.g.*, C_{16} - C_{20} hydrocarbons, alkyl esters from biodiesel), and have restricted measurements for kerosene-type middle distillates to low and moderate equivalence ratios.

In this work, the new DTC method for preparing a reactive charge directly in the RCM has been proposed and characterized in § 2.2. The method has been specifically designed for creating premixtures with non-volatile fuels, and it provides an efficient means for measuring ignition delays at a broad set of test conditions. The objectives of this study are to use the DTC approach to investigate the autoignition characteristics of the conventional jet fuels Jet-A and JP-8, as well as the alternative camelina-derived HRJ and tallow-derived HRJ fuels. The ignition delay measurements for the conventional fuels will be compared with literature data to check for consistency, and the comparison of JP-8 with HRJ fuels will be used to show that despite similar boiling ranges between the fuels, the ignition characteristics of these fuels are distinct. The integration of HRJ fuels with existing aircraft will require advanced modeling work that accounts for its unique autoignition behavior relative to JP-8, and this study proposes a useful method for obtaining this data. Furthermore, to minimize the complexity of modeling the ignition behavior of the numerous hydrocarbon components within the HRJ fuels, simulations will be performed using a simple, 2-component surrogate to evaluate the potential for predicting the ignition behavior of the bio-synthetic HRJ fuels.

To conclude this introduction, we note that this study is largely devoted to the characterization of a new test approach and a comparison of the autoignition characteristics of JP-8 with bio-derived military-grade jet fuels. For this reason, we provide only brief comments regarding prior studies of JP-8 and Jet-A autoignition chemistry. The reader is directed to the work of Dagaut et al. [37], which provides a comprehensive review of these experimental and modeling studies. Since its publication, new measurements of jet fuel ignition delays have been published, including RCM measurements by Kumar et al. [2] and shock tube measurements by Kahandawala et al. [38], Dean et al. [39] and Vasu et al. [33]. Additional Jet-A ignition delay measurements from both a RCM and a shock tube have been published by Dooley et al. [3] as part of a major initiative aimed at developing a jet fuel surrogate.

3.2. Test Fuels

Ignition delay times were measured in this study for the commercial jet fuel, Jet-A, the conventional military jet fuel, JP-8, and for the two military-grade hydrotreated renewable jet fuels, camelina HRJ (CHRJ) and tallow HRJ (THRJ). The properties of these fuels are summarized in Table 3-1. The fuel samples have been furnished by the Air Force Research Laboratory at Wright Patterson Air Force Base, and carry the standard identifiers of POSF-4658 (Jet-A), POSF-6169 (JP-8), POSF-6152 (CHRJ), and POSF-6308 (THRJ). A total ion chromatogram for each of these fuels appears in Figure 3-1. The Jet-A and JP-8 TICs are characterized by large peaks for each of the normal hydrocarbons between C_8 (*n*-octane) and C_{16} (*n*-hexadecane). The other peaks correspond to *iso*-paraffins, cycloparaffins, and aromatics (Jet-A: 19 %-vol, JP-8: 15.7 %-vol). The TICs for the HRJ fuels are distinctly different, and the data show evidence of the high ratio of branched to normal paraffinic content that is characteristic of

Property	Jet-A (POSF 4658)	JP-8 (POSF 6169)	Camelina HRJ (POSF 6152)	Tallow HRJ (POSF 6308)
Molecular Formula (estimated) †	$C_{12.15}H_{23.77}$	$C_{11.89}H_{23.06}$	$C_{11.51}H_{24.96}$	$C_{12.59}H_{27.10}$
Heat of Combustion (LHV)	43.2 MJ/kg	43.4 MJ/kg	44.1 MJ/kg	44.1 MJ/kg
Hydrogen Content (% mass)	14.1	14.0	15.4	15.3
Specific Gravity	0.806	0.798	0.752	0.758
Flash Point	51 °C	46 °C	43 °C	51 °C
Freezing Point	-48 °C	-50 °C	< -77 °C	-62 °C
Distillation				
Start	--	158 °C	151 °C	165 °C
10 %	180 °C	177 °C	161 °C	179 °C
50 %	212 °C	203 °C	182 °C	210 °C
90 %	251 °C	241 °C	237 °C	243 °C
Complete	274 °C	268 °C	259 °C	255 °C
Cetane Number ‡	47.1 [3]	38 – 49 [40-41]	53.9	--
Cetane Index *ASTM 4737, Proc. B*	48.5	49.7	63.6	66.7

† Calculated using method proposed by Rao [42].
‡ Data represent both cetane numbers and derived cetane numbers

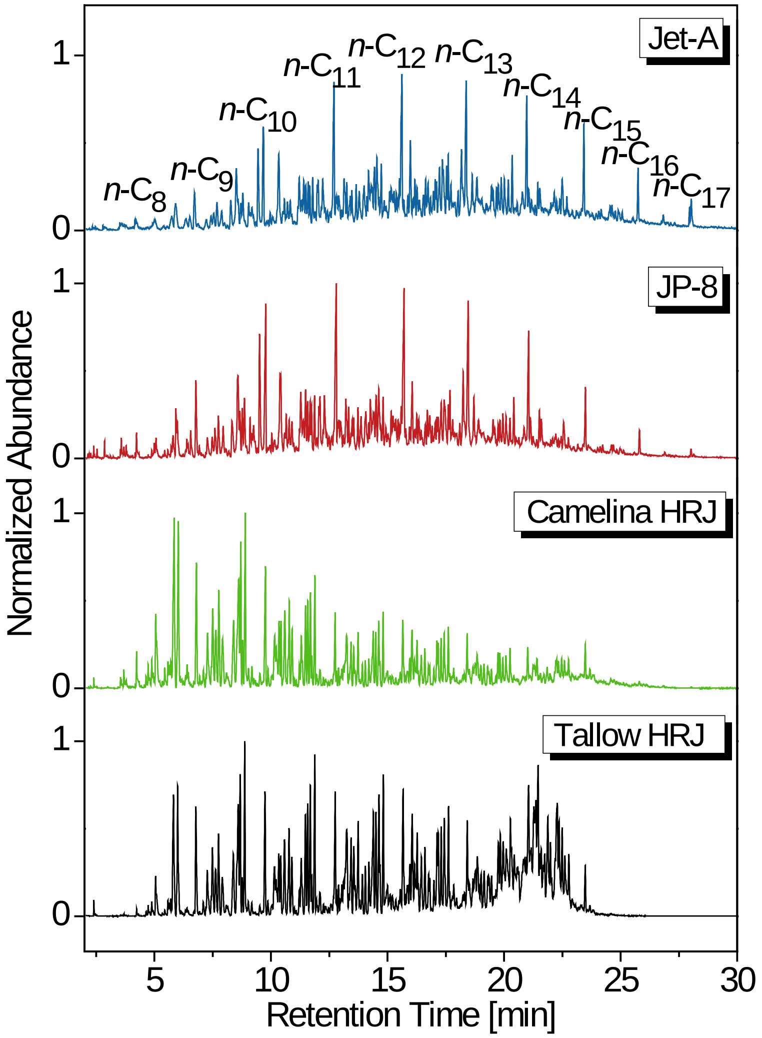

Figure 3-1. Total ion chromatograms for Jet-A, JP-8, camelina HRJ, and tallow HRJ.

HRJ fuels [43-44]. In fact, these HRJ fuels are expected to consist almost entirely of branched and normal paraffins with aromatics and olefins together comprising less than 1 % of the fuel blend [43]. The TIC data have been analyzed to estimate that the camelina HRJ and tallow HRJ fuels both have a branched to normal paraffin mass ratio of approximately 90:10 [44]. Although not apparent in the TIC data, cycloparaffins do constitute a small amount of the CHRJ (10 %) and THRJ (2 %) fuels [43].

The property data describing the jet fuels in Table 3-1 highlight three distinctive features about HRJ fuels. First, the HRJ fuels experience improved cold-flow properties relative to conventional jet fuels due to the high level of branched to normal paraffinic content. This property is manifest in the reduced freezing point for the CHRJ and THRJ compared to JP-8 and Jet-A. Second, the lack of aromatics and fully-paraffinic nature of the HRJ fuels leads to enhanced ignition quality which is evident in the derived cetane numbers and cetane indices. Finally, HRJ fuel density is low relative to conventional jet fuels, which translates into less energy for a given volume. This is considered a detriment to usability because the range payload of an aircraft is impaired when using HRJ fuels [45].

3.2.1. Average Molecular Formulae Estimation

For testing and analysis purposes, the fuel average molecular formulae must be known to estimate equivalence ratios and prepare reactive mixtures. In lieu of performing extensive chemical analysis, the average molecular formulae have been estimated using an approach from the literature which uses distillation data and specific gravity data as inputs to calculate the average molecular weight of a petroleum blend [42]. This approach is coupled with the fuel specification data describing the hydrogen content (%-mass) to determine the average molecular formulae. All of the required data for these calculations appears in Table 3-1. The approach for estimating the average molecular weight has been published by Rao, and it seeks to correlate the average molecular weight (M) as a function of mixture boiling point (T_b),

$$M = \left({}^{T_b}\!/_{A} \right)^{B} \tag{3-1}$$

The parameters A and B in Equation 3-1 are calculated based on the molal average boiling point, T_M, as described by Rao [42]. All of the required equations appear in the original publication, except for a definition of the volumetric average boiling point, which we have defined as

$$T_V = \frac{T_{10} + T_{50} + T_{90}}{3}, \tag{3-2}$$

where T_{10}, T_{50} and T_{90} correspond the temperatures (K) at which 10 %, 50 %, and 90 %, respectively, of the volume is recovered during distillation.

Using this approach, the fuel average molecular formulae for Jet-A, JP-8, CHRJ and THRJ have been estimated as $C_{12.15}$ $H_{23.77}$, $C_{11.89}H_{23.06}$, $C_{11.51}H_{24.96}$, and $C_{12.59}H_{27.10}$, respectively. These formulae are used to prepare a reactive charge in the RCM with a given equivalence ratio. However, it should be noted that the test mixtures have been created on a mass basis, and these molecular formulae are used only to calculate the corresponding equivalence ratios and mole fractions that are required for the compressed temperature calculations. The author notes that the average molecular formulae do confirm an important expectation regarding the fuel compositions. The estimated molecular formulae for the HRJ fuels closely follow C_nH_{2n+2}, which is the characteristic formula for the normal and branched paraffins expected to largely comprise the HRJ fuels. The estimated formulae for Jet-A and JP-8 indicate a lower carbon-to-hydrogen ratio than for the CHRJ fuel, and are a result of the olefins, aromatics, cycloparaffins found in conventional jet fuels.

3.3. Experimental Test Conditions

Ignition delay measurements have been made in the RCM for JP-8, CHRJ and THRJ fuels at compressed temperatures of 625 K ≤ T_C ≤ 730 K, compressed pressures of p_C = 5, 10 and 20 bar, and at equivalence ratios of ϕ = 0.25, 0.5 and 1.0. All reactive charges have been prepared in synthetic dry air, 21 % O_2 and 79 % N_2. The compressed temperatures and pressures are attained through a combination of changes in compression ratio and by changing the initial temperature and pressure of the charge. Initial temperatures between 110 °C and 135 °C were selected to ensure complete fuel vaporization, which has been confirmed using GC/MS analysis as discussed in § 2.2.1. The upper limit of tested compressed temperatures was selected to avoid first stage ignition activity during the compression stroke. Such an occurrence prohibits use of the ignition delay definition, and prevents accurate assignment of a compressed temperature. The investigated test conditions are graphically-summarized in Figure 3-2 relative to other jet fuel oxidation studies. Based on the figure, it is seen that the tests are focused on the low temperature and low-to-moderate pressure regions.

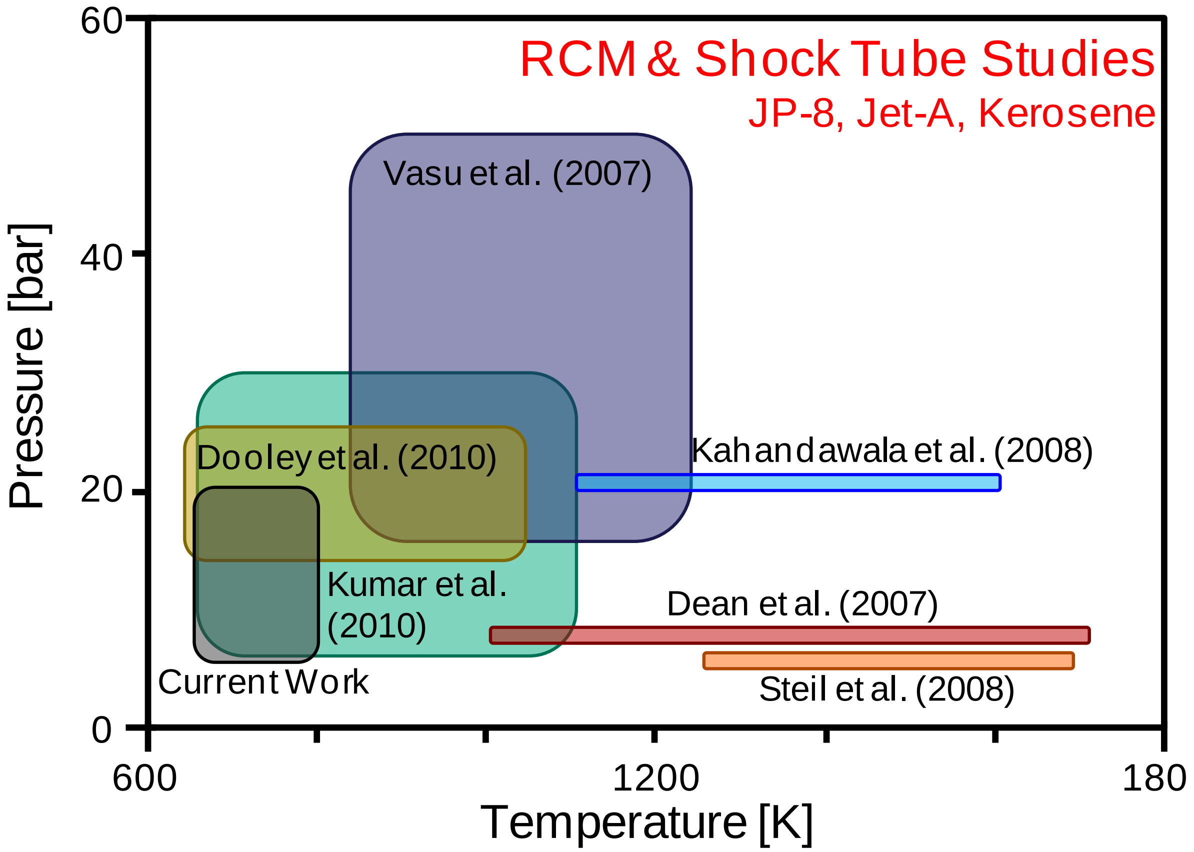

Figure 3-2. Summary of test conditions investigated in this work and in prior studies published in the literature for JP-8, Jet-A and kerosene.

3.4. Kinetic Modeling for Jet Fuel Surrogates

3.4.1. JP-8 Fuel Surrogate

The experimental measurements of JP-8 ignition delays have been complemented by ignition delay calculations from a kinetic model, primarily to identify the role of the compression process in determining the ignition delay. To represent the complex hydrocarbon blend of JP-8, the simulations utilize the JP-8 surrogate (Violi #3) proposed by Violi et al. [46], which is described in the previous chapter in Table 2-1. The hydrocarbon kinetic mechanism published by Ranzi et al. [32] is used for the simulations, which is comprised of 10,951 reactions, representing 365 species. The simulations were conducted in CHEMKIN 4.1, and the compression process and heat losses are accounted for by specifying an effective volume profile as described in § 2.5.1. Results from these simulations appear in Figure 3-4 and will be discussed in the § 3.6.

3.4.2. HRJ Fuel Surrogate

Kinetic modeling has been used to evaluate the potential of using a 2-component surrogate fuel to predict the ignition behavior of the bio-synthetic HRJ fuels. The major species in the HRJ fuels are *n*-paraffins and *iso*-paraffins, and analysis of the TIC in Figure 3-1 yielded a composition estimate for both the CHRJ and THRJ fuels of 10 % *n*-paraffins and 90 % *iso*-paraffins when cycloparaffins are neglected. This estimation is consistent with data in the literature [43], and has been chosen as basis for setting the surrogate fuel composition. Considering the average molecular formulae presented in § 3.2.1, we propose using a surrogate fuel blend of two C_{12} hydrocarbons: 10 % *n*-dodecane and 90 % 2-methylundecane.

The proposed surrogate has been used with the kinetic model of Sarathy et al. [34] for modeling the oxidation of 2-methylalkanes. The kinetic mechanism consists of 7171 chemical species and 31,669 reactions and includes refined chemistry for $C_8 - C_{16}$ *n*-alkanes [47]. We have selected this mechanism because to our knowledge, no other mechanism exists which can accommodate high molecular weight *iso*-paraffins. However, we note that validation studies published with the mechanism considered fuels of only modest molecular weight: 2-methylhexane, 2-methylheptane, and *n*-octane. The authors suggest that validation using these fuels is representative of the class of 2-methylalkanes, and that the results can be considered valid for larger 2-methylalkanes where the same reaction rate rules have been applied [34].

The kinetic simulations have been conducted in CHEMKIN PRO using the closed homogeneous batch reactor model. Heat loss from the RCM has been considered in these models by including a volume expansion term in the effective volume profiles that constrain the volume during the CHEMKIN simulations. Details of this approach were described in § 2.5.1.

3.5. Data Analysis and Uncertainty

3.5.1. Adiabatic Core Hypothesis and Compressed Temperature Calculations

For a purely vapor charge, the compressed temperature can be predicted by assuming a core region of the charge is isentropically-compressed. Previous studies have demonstrated the adiabatic core hypothesis is theoretically valid in a RCM [24], and Mittal and Sung have experimentally demonstrated that the use of a creviced piston supports the hypothesis [15]. Under the existence of an adiabatic core, the compressed temperature can be calculated by

$$\int_{T_0}^{T_c} \frac{\gamma}{\gamma - 1} \frac{dT}{T} = ln \frac{p_c}{p_0}, \tag{3-3}$$

where T is temperature, γ is the specific heat ratio (C_p/C_v), p is pressure, and the subscripts *0* and *c* correspond to initial and compressed conditions, respectively. It should be noted that the compressed temperature (T_C) in Equation 3-3 is not the temperature of an adiabatically-compressed charge. Heat loss is occurring during the compression process and is accounted for by the experimentally-measured pressure (p_C).

3.5.2. Ignition Delay Definition

The primary measurement derived from RCM test data is the ignition delay. In this section, we provide a standard definition of the ignition delay periods so the results from all tests may be compared without ambiguity. This is especially important when two-stage ignition behavior is observed, as it was for all tests in this study. For ignition events of this type, multiple ignition delay periods are defined to fully characterize the ignition event. As illustrated in Figure 3-3, the first-stage ignition delay (τ_1) is defined as the time period between the end of compression and the maximum rate of pressure rise due to first-stage ignition activity. The end of compression is identified as the time when the time derivative of the pressure (*dp/dt*) becomes negative. The second-stage ignition delay (τ_2) is defined as the time duration between the end of τ_1 and the maximum rate of pressure rise due to the second stage of ignition. The overall ignition delay period is referred to as $\tau = \tau_1 + \tau_2$, and is illustrated in Figure 3-3.

Figure 3-3 also reveals the high frequency oscillations present in the raw pressure data, which arise from the extreme impulsive load on the pressure transducer during ignition. These oscillations are similar in nature to the oscillations observed in homogeneous charge compression ignition engines when excessive pressure rise rates exist during combustion [48]. It is desirable to filter these oscillations for more straightforward data analysis. As an example, the raw pressure data in Figure 3-3 is complemented with the same dataset after a filtering option.

The data have been filtered using a low-pass Butterworth filter with a 5000 Hz cutoff frequency, which has additionally been applied to all datasets in this study prior to calculating the ignition delay periods. Filtering the data simplifies identification of the inflection points in *dp/dt*, and does not eliminate or alter any critical information from the data, such as the timing of top dead center or the timing of pressure rise due to ignition.

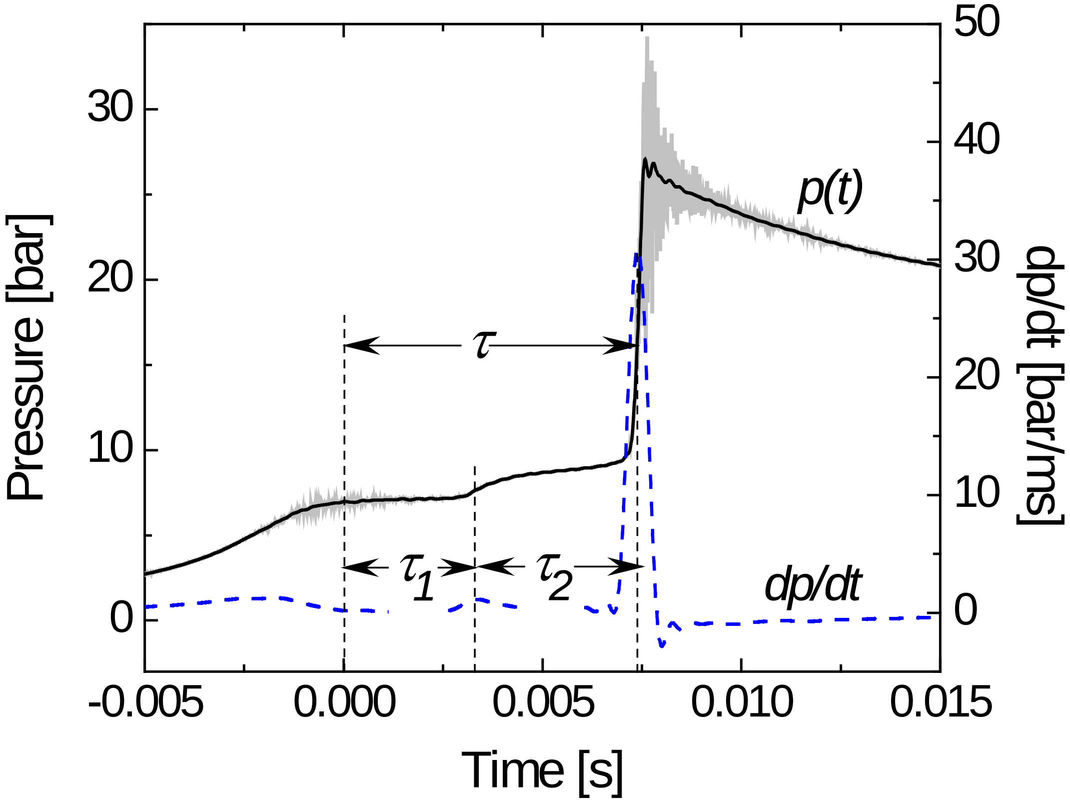

Figure 3-3. Sample pressure history data and pressure derivative data (*dp/dt*) illustrating the filtering operation and the ignition delay definitions for τ_1, τ_2, and τ.

3.5.3. Thermophysical Properties

The JP-8 and CHRJ fuels are complex mixtures of hundreds of hydrocarbon components. It is rare that a single isomeric compound comprises more than 5 % of the mixture [49]. With the exact composition unknown, the ideal gas heat capacity is often estimated using a surrogate blend with a limited number of components. The five-component JP-8 surrogate mixture (Violi #3) proposed by Violi et al. [46] has been used in this study to estimate the compressed temperatures of JP-8 and oxidizer gas mixtures. The composition of this surrogate is listed in Table 2-1. For the HRJ fuels, which are greater than 99 % paraffinic, we can calculate T_c using the thermophysical properties of any single paraffin. This is true because mixtures have been made by injecting a known fuel mass, and subsequently calculating fuel mole fractions from the molecular weight estimations that are based upon the proposed average molecular formulae. Although each paraffin has a unique constant-pressure heat capacity (C_p), weighting the values by their respective fuel mole fractions (X_f) makes the differences in $X_f \cdot C_p$ negligible. For this type of calculation, we have used the thermophysical property data of *n*-dodecane [31].

3.5.4. Experimental Uncertainty

All test conditions are repeated a minimum of three times, and the standard deviations of the measurements are represented by error bars when presenting results in the following section. Total ignition delay measurements were repeatable to within ±5 % and first stage ignition delay measurements were repeatable to within ±8 %. The main uncertainty in the experiments is the calculation of a compressed temperature as a reference for comparing datasets. The compressed temperature calculations are influenced by uncertainties in initial temperature (±3 K), initial pressure (±0.08 %), initial volume (± 0.004 L), compressed pressure (±0.3 bar), injected fuel mass (±3 %), and thermophysical property data (±0.5 %). These inputs have been used to calculate the uncertainty in the compressed temperature as ±1.25 % (8 – 9 K), which is represented by error bars in subsequently presented data.

3.6. Experimental Results & Surrogate Model Predictions

3.6.1. Comparison of Ignition Delay Measurements with Literature Data

For the new DTC charge preparation approach proposed in this work, it is desirable to obtain ignition delay data that can be compared with prior measurements in the literature using a batch-based mixture preparation approach. There is an abundance of published Jet-A ignition delay data for test conditions near 20 bar, which we have used for comparison. Discrepancies in test pressures are reconciled in the comparison by scaling all of the literature ignition delays as $\tau \sim 1/p_C$. We expect this scaling may be too simplistic, and may obscure the comparison; however, in the absence of more comprehensive data, it is a good starting point considering its widespread use in the literature [39,50]. The results of this first comparison motivated an additional comparison to be made for JP-8 at the lower compressed pressure of 7 bar. Existing ignition delay measurements published in the literature were recorded at a compressed pressure of 7 bar, and this serves as an additional direct comparison for data measured in a rapid compression machine without any pressure scaling requirements.

Autoignition Behavior of Jet-A and Air at a Compressed Pressure of 20 bar

Figure 3-4 shows the ignition delay data measured in the RCM for stoichiometric mixtures of Jet-A and air at a compressed pressure of 20 bar. All measurements were taken at low compressed temperatures (670 – 750 K) by compressing a mixture with an initial temperature of T_0 = 135 °C. Overall, the datasets from the literature exhibit good consistency at high temperatures, but the agreement deteriorates at low temperatures where peroxy chemistry dominates. The measured ignition delays from this study are shorter than published by other authors. We speculate that the variability between the measurements may be a result of three

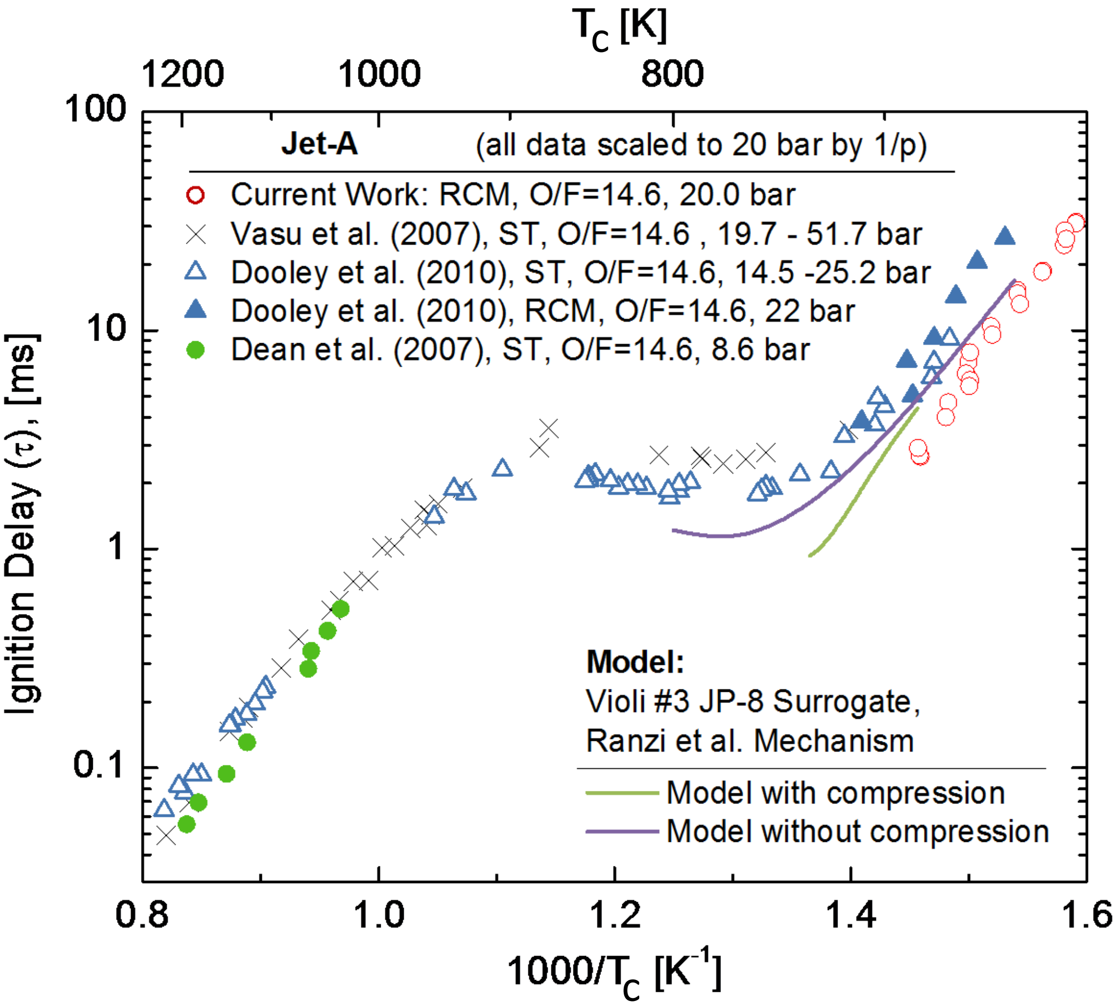

Figure 3-4. Comparison of Jet-A ignition delay measurements in the RCM with data published in the literature. Simulations using a JP-8 surrogate investigate the influence of compression on the ignition delay time.

different effects. First, error may be introduced by scaling the data, where we assume the ignition delay exhibits a p^n dependency with n = -1.0. Although this dependency is commonly used, preliminary kinetic modeling results using the Ranzi mechanism [32] and the Violi #3 [46] surrogate suggest that for our tested temperature range, the pressure dependence is much less and that on average n = -0.4. It is worth noting, that the agreement between the datasets improves for exponents greater than n = -1.0. Second, some of the ignition delay data compared in Figure 3-4 were measured in shock tubes (ST). Shock tubes do not rely on the mechanical compression process used in a RCM which can initiate fuel oxidation reactions during the late stages of compression. These effects are generally considered negligible for fuels exhibiting longer ignition delays (> 10 ms), but the early reaction may be significant for the measurements we have reported. To consider the influence of compression, chemical kinetics simulations have been conducted for two sets of cases. The first simulation set uses compression to generate the conditions at TDC, while the second set is treated as a constant volume bomb with the conditions at TDC used as the initial conditions in the simulation. These simulations utilized the Violi #3 JP-8 surrogate formulation [46] and the hydrocarbon mechanism proposed by Ranzi et al. [32]. The purpose of these simulations is only to consider the effects of compression, thus variations in the Jet-A and JP-8 chemical components are not expected to influence the findings. Absolute comparisons of the ignition delay measurements and predicted values are not the intended for these calculations. The simulation results appear in Figure 3-4 and clearly indicate that the compression process plays a more important role in determining the ignition delay as the compressed temperature increases. The simulations also corroborate our finding that additional measurements at higher temperatures are prohibited in the RCM because τ_1 approaches zero, which prevents the assignment of reaction conditions at TDC. Overall, the simulations demonstrate that the compression process is not responsible for the discrepancy between the datasets across the entire range of test conditions, particularly at lower compressed temperatures. The final point to consider when comparing the data in Figure 3-4 is that each study has vaporized the fuel using unique initial temperatures and fuel vessel residence times. Some, but not all of these studies have included GC/MS analysis to confirm the fuel composition in the test device, and as we have noted, this may be of consequence for test mixtures which are heated for hours, thus increasing the opportunity for thermal decomposition of the fuel. The likelihood of thermal decomposition of a fuel increases with the number of carbon atoms in the fuel molecule. These same fuel molecules, with increasing numbers of carbon atoms, are known to ignite more readily, and elimination of these species from the mixture has the potential to increase the ignition delay of the aggregate fuel mixture. The potential increased presence of higher hydrocarbon species in our test mixtures may lead to shorter ignition delays relative to other studies.

In spite of the minor discrepancies between the datasets, the comparisons presented in this section lead to the important conclusion that the DTC approach yields repeatable ignition delay measurements that are generally consistent with our expectations regarding NTC behavior and absolute ignition delay times.

Autoignition Behavior of JP-8 and Air at a Compressed Pressure of 7 bar

An additional set of ignition delay measurements was taken for JP-8 in air at a compressed pressure of 7 bar. This lower pressure facilitates a more direct comparison with literature data because ignition delay data from a RCM has been previously published for JP-8 at a compressed pressure of 7 bar [2]. A comparison of these two datasets does not require scaling for the pressure dependency and can be considered to be more reliable than the comparison presented in § 3.6.1.

An oxidizer-to-fuel mass ratio of *O/F* = 14.6 was used for the first set of measurements at p_C = 7 bar, which is similar to the value *O/F* = 13 used by Kumar and Sung [2]. The data from these measurements are compared in Figure 3-5. The τ_1 measurements reported in the two studies are consistent, but in spite of the similarity in test conditions, there is an approximately four-fold difference in the overall ignition delay measurements. This disparity is quite large considering that the comparison in Figure 3-4. shows much better agreement among the data produced by the two different RCMs. We investigated the discrepancy in the measurements by first considering previously reported data by the authors, which demonstrated that the overall ignition delay of JP-8 is sensitive to changes in equivalence ratio, but that the first ignition delay period is insensitive to this parameter [51]. As noted, one of the major benefits of the DTC test approach is that by loading fuel directly into the test chamber, the fuel concentration is readily known, and it can be easily adjusted by altering the number and duration of fuel injections. This

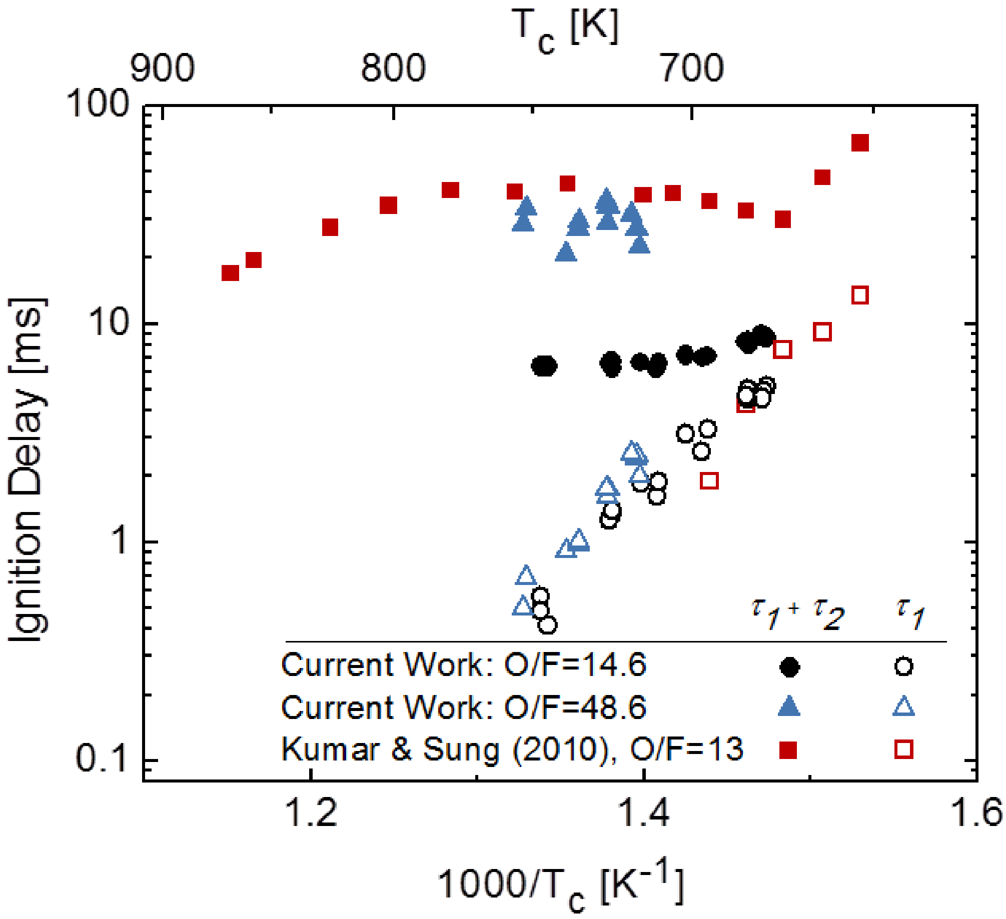

Figure 3-5. JP-8 ignition delay measurements at a compressed pressure of 7 bar compared with values published by Kumar and Sung [2].

advantage facilitated additional ignition delay measurements under much leaner conditions with an oxidizer-to-fuel mass ratio of *O/F* = 48.6. These data are reported in Figure 3-5, where τ_1 is observed to be similar to the τ_1 measurements recorded at *O/F* = 14.6. However, the τ data is noticeably longer and approaches the duration reported by Kumar and Sung [2]. The consistency in the τ data deteriorates for the measurements at *O/F* = 48.6 relative to the measurements at *O/F* = 14.6. This occurs because as few as two injections are required to create the premixed charges using *O/F* = 48.6, and shot-to-shot variation in the injector performance becomes an important consideration.

3.6.2. Comparison of Conventional and Bio-synthetic Paraffinic Kerosene Fuels

Ignition Delay Measurements

Ignition delay measurements for JP-8, CHRJ and THRJ fuels recorded in this work are compared in Figure 3-6a with Jet-A ignition delay measurements reported by Dooley et al. [3]. All measurements from this study that appear in Figure 3-6a were taken for ϕ = 1.0 and a compressed pressure of 20 bar. The shock tube measurements reported by Dooley et al. [3] were also made at ϕ = 1.0 and pressures between 14.5 and 25.2 bar. These data have been scaled to 20 bar using $\tau \sim 1/p$ to facilitate the comparison. Ignition delays for the conventional petroleum-based jet fuels JP-8 and Jet-A are generally consistent, which is not unexpected because the compositions of the two fuels are quite similar [52]. The agreement between the two datasets improves as the compressed temperature decreases. For shorter ignition delays, specifically those less than 10 ms, the measurements in the RCM become increasingly affected by preignition reactions that may occur during the late stages of the compression stroke. The shock tube data are not influenced by this type of physical process, and we attribute the qualitative deviation in the two datasets to the influence of compression. This hypothesis is meant to address only the qualitative nature of the ignition delay trend and not the absolute measurements. We are comparing two different fuels and we should not expect perfect congruency between the datasets.

The JP-8, CHRJ and THRJ fuels data in Figure 3-6 are repeated in the inset figure for improved visibility. Error bars have been omitted from these data for clarity. For a given test conditions, the JP-8 clearly exhibits a longer ignition delay than either of the HRJ fuels. On average, the JP-8 ignition delays are 2 times and 3 times longer than those of the CHRJ and THRJ fuels, respectively. These differences are outside the uncertainty range for the measurements. The enhanced reactivity of the HRJ fuels relative to JP-8 can be attributed primarily to the lack of aromatics in the HRJ fuels. Conventional jet fuel may contain up to 25 % aromatics, and the blend of JP-8 tested in this study contained 15.7 % aromatics by volume. The findings are consistent with cetane numbers reported in the literature. Published studies have reported JP-8 cetane numbers between 38 and 49, while a derived cetane number of 53.9 has been obtained for CHRJ fuel using ASTM D6890 [53]. The (derived) cetane number provides a measure of fuel ignition quality, and a higher number corresponds to a shorter ignition delay time. To our knowledge, no cetane numbers have been reported for THRJ fuel, although a derived cetane number of 49.82 has been reported for a 50/50 blend of JP-8/THRJ fuel [54]. The same report noted a derived cetane number of 49.22 for a 50/50 blend of JP-8/CHRJ fuel, which is a very modest difference (-1 %) from that of the JP-8/THRJ fuel blend. Still, these data support the observation in Figure 3-6a that the THRJ fuel ignites marginally-faster than the CHRJ fuel at a given temperature. Comparisons of unique data points for these two fuels are within the uncertainty range of the measurements, but the overall trend suggests that the ignition delays for the fuels are distinct.

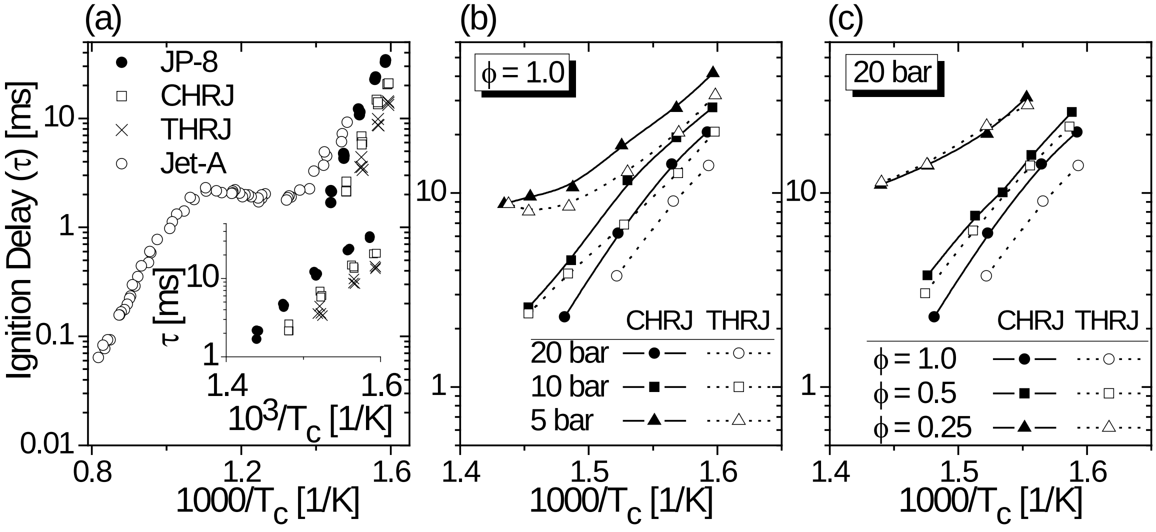

Figure 3-6. (a) Comparison of conventional and biosynthetic kerosene fuels. Data for JP-8, CHRJ, and THRJ fuels are based on the current work, and the Jet-A data are adapted from the work of Dooley et al. [3]. Measurements correspond to p = 20 bar and ϕ = 1.0. The inset figure provides more resolution for the JP-8, CHRJ and THRJ fuels data. (b) Ignition delays for CHRJ and THRJ fuels at ϕ = 1.0 and p_C = 5, 10, and 20 bar. (c) Ignition delays for CHRJ and THRJ fuels at p_C = 20 bar and ϕ = 0.25, 0.5, and 1.0.

Additional comparisons of the HRJ fuels appear in Figure 3-6b and 3-6c. The error bars have been omitted from these data for clarity, and the authors note that the data for the two fuels at any given condition are within the uncertainty range of one another. However, trends within the datasets suggest the ignition characteristics of the two fuels are distinct under certain conditions. Considering Figure 3-6b, where all measurements have been made at ϕ = 1.0, the THRJ fuel ignition delays are generally shorter than for the CHRJ fuel, especially with decreasing compressed temperature. The variation between the datasets does not appear to be influenced by the compressed pressure. In Figure 3-6c, where all data have been recorded with a compressed pressure of 20 bar, a different pattern appears, in which the ignition characteristics increase in resemblance as the charge is made more fuel-lean. Taken together, Figure 3-6b and Figure 3-6c indicate that the hydrocarbon distribution of the two HRJ fuels influences ignition characteristics only for stoichiometric conditions, and not for fuel-lean mixtures.

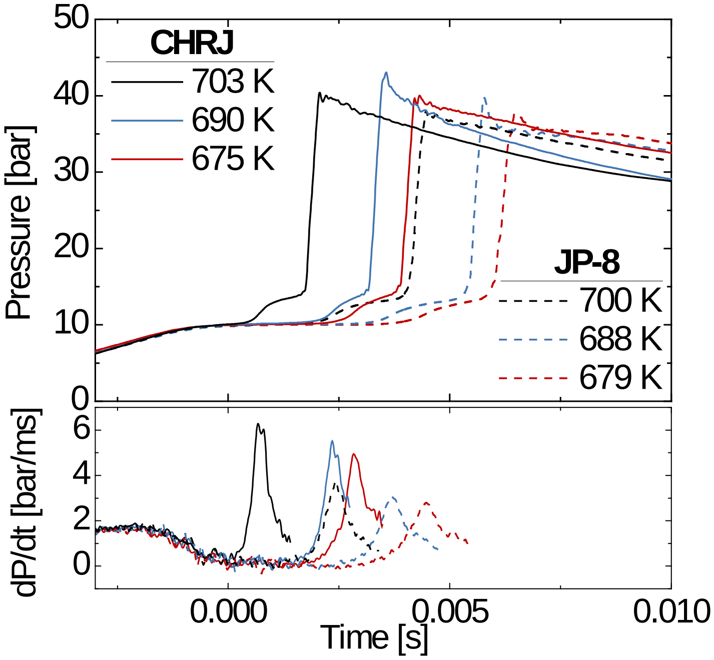

Figure 3-7. Pressure history and rate of pressure rise curves for ignition of CHRJ fuel (solid lines) and JP-8 (dashed lines) in air at similar compressed temperatures.

Pressure History Data

Figure 3-7 shows three ignition pressure history curves for both CHRJ fuel and JP-8 at compressed pressures of 10 bar and an oxidizer-to-fuel mass ratio of *O/F* = 14.6. These tests have been chosen for comparison because the ignition delay times for JP-8 and CHRJ fuel can be compared at similar compressed temperatures. We first note that both the JP-8 and CHRJ fuel exhibit a reduction in both τ_1 and τ as temperature is increased, indicating that these tests are performed outside of the NTC region. The data clearly demonstrate that CHRJ fuel is more reactive than JP-8 at a given test temperature. In fact, the total ignition delay measurements for the CHRJ fuel tests are shorter than all of the total ignition delay measurements for the JP-8 tests. The enhanced reactivity of the CHRJ fuel relative to JP-8 is a result of the lack of aromatics and limited cycloparaffins in the CHRJ fuel which tend to decrease the cetane number of a fuel blend. Conventional jet fuel may contain up to 25 % aromatics, and the specific JP-8 tested in this study contained 15.7 % aromatics by volume. In addition to the timing of the first stage of ignition, it is worthwhile to note that the rate of pressure rise during the first stage of ignition is faster for the CHRJ fuel than for JP-8. This is indicative of more vigorous heat release during the first stage of ignition. We expect this occurs because CHRJ fuel is composed almost entirely of normal and branched paraffins, which are more likely to participate in low temperature ignition pathways. Although normal and branched paraffins comprise a significant portion of JP-8, the aromatics and cycloparaffins do not generally contribute to low temperature chain branching pathways, meaning less energy is released during the first stage of ignition. Ignition behavior of this type is relevant for advanced compression ignition engines where the ignition time is controlled by fuel kinetics, and these characteristics must be studied further by the U.S. Department of Defense before consideration as a single fuel on the battlefield.

3.6.3. Influence of Equivalence Ratio on Ignition Delay Time Measurements and Surrogate Predictions

Figure 3-8 reports ignition delay measurements for JP-8, CHRJ and THRJ fuels at a compressed pressure of 20 bar, and equivalence ratios of 1.0, 0.5 and 0.25. The total ignition delays for all of the fuels exhibit an inverse dependence on the equivalence ratio; and qualitatively, the $\phi = 1.0$ and the $\phi = 0.5$ tests exhibit more similarity than the $\phi = 0.5$ and the $\phi = 0.25$ tests for each fuel. The $\phi = 0.25$ test cases for all of the fuels provide evidence of the onset of negative temperature coefficient (NTC) behavior, a region which is characterized by a loss of reactivity with increasing temperature. No evidence of NTC behavior can be observed in the $\phi = 1.0$ and the $\phi = 0.5$ tests, although it may be expected to emerge at higher compressed temperatures.

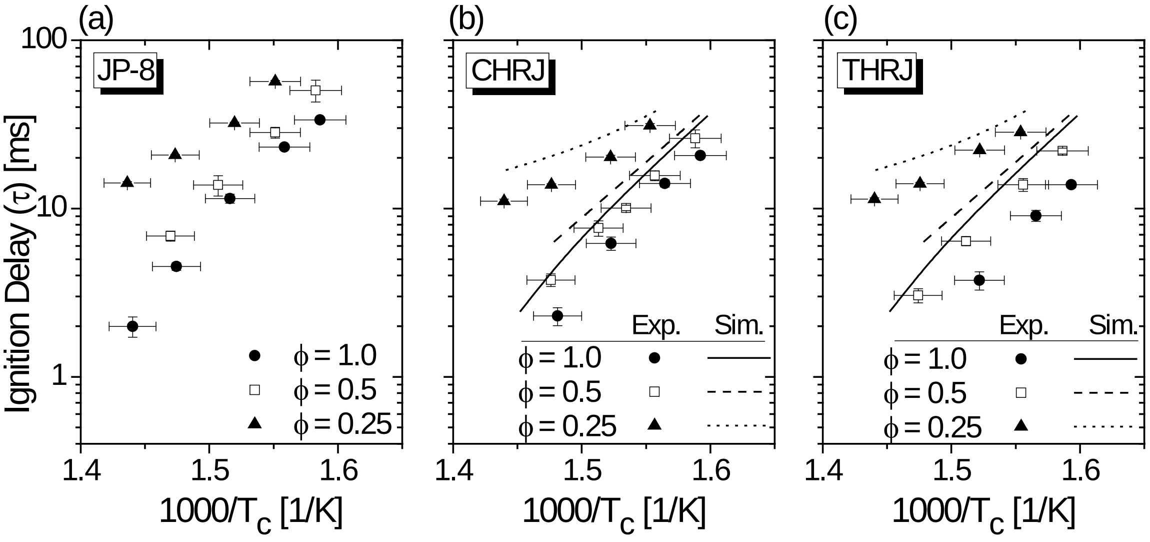

Figure 3-8. Ignition delay measurements for (a) JP-8, (b) CHRJ, and (c) THRJ fuels at p_C = 20 bar and ϕ = 0.25, 0.5 and 1.0. The same set of kinetic simulation results appear in (b) and (c) for ϕ = 0.25, 0.5 and 1.0, using the proposed 2-component surrogate.

For the CHRJ and THRJ fuels, the qualitative behavior of ignition delays with changing temperature is well-represented by the surrogate fuel simulations, however, the absolute magnitudes of the predicted ignition delays do not match measured values. It is worth noting that some of the predictions are within the estimated uncertainty of the compressed temperatures, but the mechanism predicts ignition delays that are longer than the measurements for all test cases. This type of overprediction by the mechanism of Sarathy et al. has been reported in the publication describing the mechanism [34], with respect to 2-methylhexane ignition delay measurements obtained with a RCM and published by Silke et al. [55]. However, the authors make this remark cautiously because the results reported here are for a simplified surrogate that can, at best, approximate global behavior. The predictive accuracy of the model cannot be directly evaluated with the surrogate data reported here, although empirical feedback can be obtained. Typically, we may suggest improvement of the predictions by modifying the surrogate composition to include more reactive species (*i.e.*, normal hydrocarbons), although the compositional changes that improve the predictions would not be reflective of the actual blend composition. A more realistic representation of the fuel may include di-alkylated paraffins (*e.g.*, 2,5-dimethyldecane) or cycloparaffins, but these species will have a tendency to increase the ignition delay predictions, thus deteriorating the agreement with the data. Furthermore, we may not expect dramatic improvements in the predictions because at temperatures below the NTC region (~ 750 K), demethylation at the penultimate carbon does little to enhance reactivity, especially for alkane chain lengths greater than 7 carbons [50]. This analysis suggests that the model generally overpredicts the ignition delay, and that the mechanism may benefit from reassessment of the rate constants.

3.6.4. Influence of Compressed Pressure on Ignition Delay Time Measurements and Surrogate Predictions

Total ignition delays for JP-8, CHRJ and THRJ fuels are shown in Figure 3-9 at compressed pressures of 5 bar, 10 bar, and 20 bar. All measurements were taken under stoichiometric conditions in air. The ignition delays for all fuels exhibit an inverse dependence on compressed pressure, and the 5 bar tests clearly demonstrate NTC behavior with increasing compressed temperature. NTC behavior for the JP-8 tests becomes visible near T_C = 700 K, while the transition temperature is slightly lower for the HRJ fuels at 680 K. Approaching the NTC region from low temperatures, the datasets for each of the compressed pressures begin to diverge for all the fuels. The distinction between the datasets arises because of the competition between decomposition (*i.e.*, chain-terminating) of the alkyl hydroperoxy radical (QOOH) and an oxygen addition reaction (QOOH + O_2) with ensuing chain-branching. The competition between these pathways is highly pressure-dependent [50], and as the QOOH decomposition pathways are activated in the NTC region, the strong pressure dependence emerges.

The model predictions using the Sarathy et al. mechanism [34] and the *n*-dodecane/2-methylundecane surrogate are included in Figure 3-8b and Figure 3-8c. The model results reflect the functional dependence on pressure, including prediction of the pronounced NTC region for the 5 bar CHRJ and THRJ fuels test results. Considering the aggregate results, the mechanism predictions capture the pressure dependence with more accuracy than the equivalence ratio dependence, as presented in § 3.6.3. The best agreement is observed for the 5 bar test cases, with the CHRJ fuel ignition delay measurements providing a closer match than those of the THRJ fuel. For $T_C <$ 675 K, the mechanism predicts ignition delays that are an average of 8 % shorter than the CHRJ fuel measurements, and an average of 4 % longer than the THRJ fuel measurements. Entering the NTC region, the predictions diverge for both HRJ fuels to become 40 % shorter than the experimental measurements. The increased sensitivity to pressure in the NTC region is reason to consider lower molecular weight surrogate components such as the C_{10}

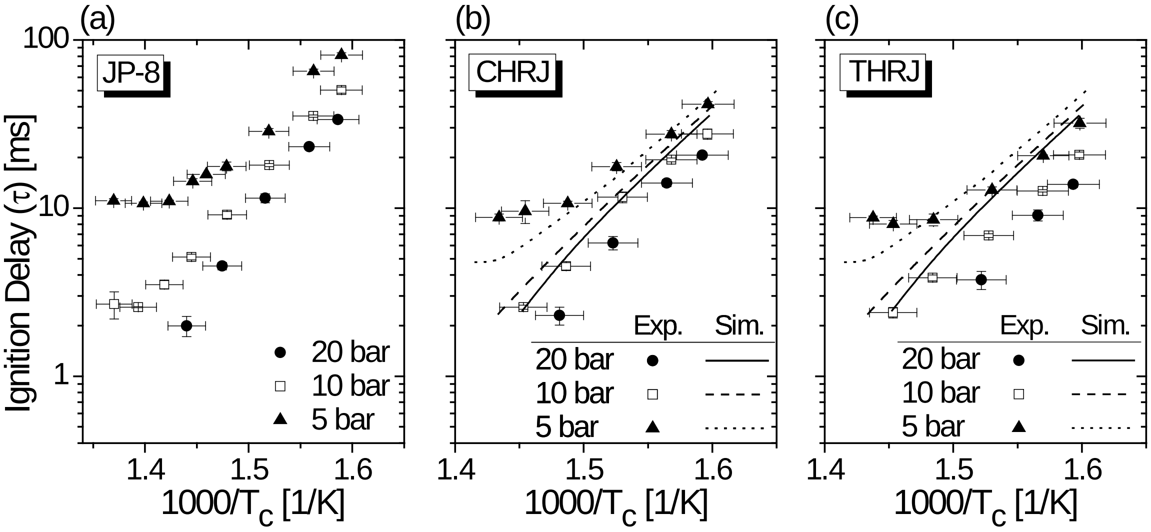

Figure 3-9. Ignition delay measurements for (a) JP-8, (b) CHRJ, and (c) THRJ fuels at $\phi = 1.0$ and p_C = 5, 10, and 20 bar. The same set of kinetic simulation results appear in (b) and (c) for p_C = 5, 10, and 20 bar, using the proposed 2-component surrogate.

hydrocarbons, *n*-decane or 2-methylnonane. Replacement of the C_{12} hydrocarbons in the surrogate with C_{10} hydrocarbons will tend to increase the ignition delay in the NTC region, while having minimal influence at lower temperatures where the agreement is already satisfactory. Future work will explore opportunities to improve the ignition delay predictions by altering the surrogate fuel composition.

3.6.5. Global Regression: Ignition Delay Correlations

Global correlations describing the total ignition delay time have been derived for each of the military-grade jet fuels, considering all of the test conditions. Achievement of acceptable and useful fits to all of the data, including compressed temperatures approaching the NTC region, required that the pressure and equivalence ratio terms in the correlation be defined in terms of temperature. The need to couple these terms is apparent when observing the dramatic change in pressure and equivalence ratio dependence as temperature changes in Figures 3-8 and 3-9. Prior studies have noted that a functional relationship of $\tau \sim p^n$ is too simple to capture the complex pressure dependence across the low-temperature and the NTC region [56], and our data confirm this conclusion. We address this challenge by correlating the data using, $\tau = A \cdot p_c{}^{B+C\cdot T_c} \varphi^{D+E\cdot T_c} e^{F/T_c}$, where *A, B, C, D, E,* and *F* are all arbitrary optimization parameters. The results of this correlation for each fuel are reviewed in Figure 3-10, where the data and correlation are scaled to p_c = 20 bar and ϕ = 1.0 using the correlation parameters. The data clearly capture the distinct difference between the JP-8 and HRJ fuels test data, and a more subtle difference exists between the two HRJ fuels.

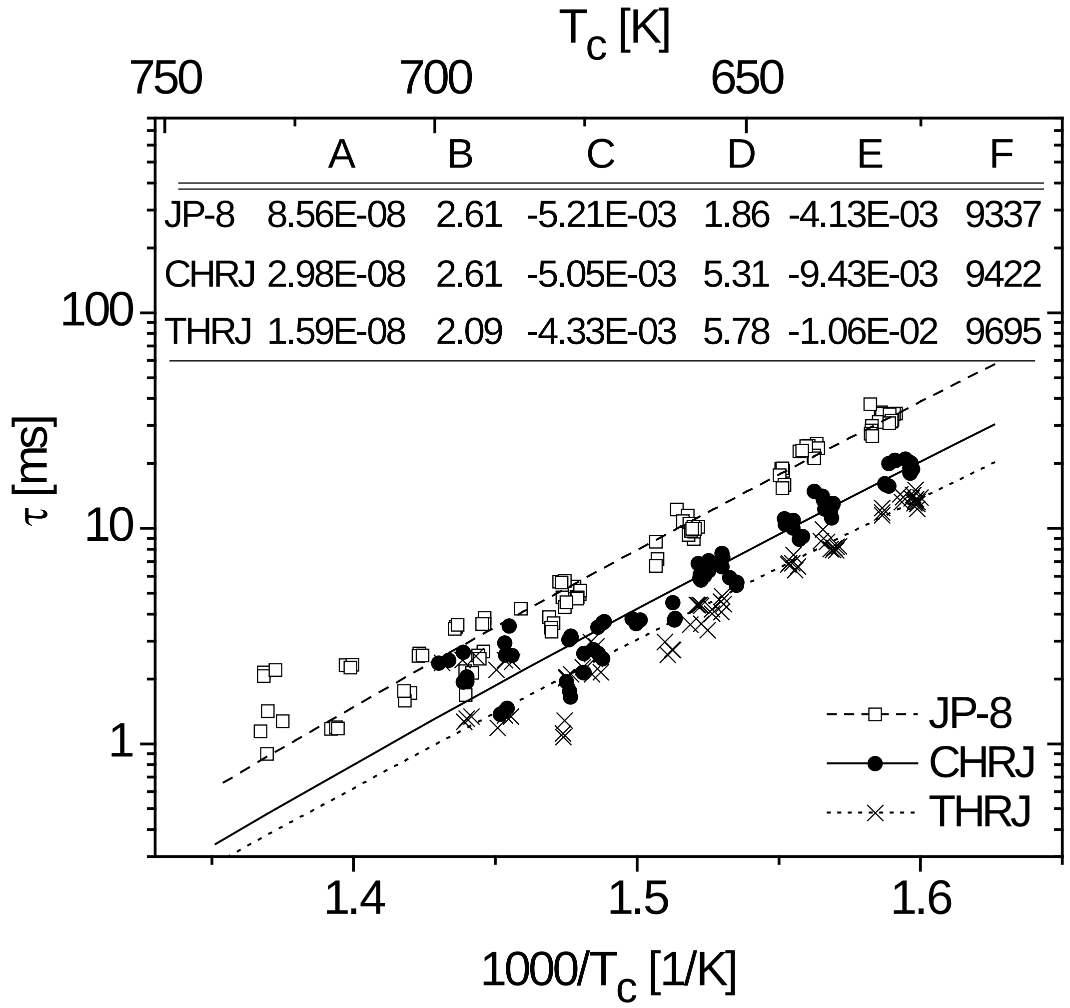

	A	B	C	D	E	F
JP-8	8.56E-08	2.61	-5.21E-03	1.86	-4.13E-03	9337
CHRJ	2.98E-08	2.61	-5.05E-03	5.31	-9.43E-03	9422
THRJ	1.59E-08	2.09	-4.33E-03	5.78	-1.06E-02	9695

Figure 3-10. Global ignition delay correlations for JP-8, CHRJ and THRJ fuels.

3.7. Development of a Commercial Jet Fuel Surrogate

Detailed kinetic simulation of a real hydrocarbon distillate fuel remains a computational challenge, and the most frequently proposed solution is to establish a surrogate fuel that can be used to mimic the combustion behavior of the real fuel under a wide set of conditions. Significant interest exists in identifying such a surrogate for the commercial jet fuel Jet-A (POSF 4658), and recent work has conducted extensive experimental comparisons of Jet-A ignition and combustion behavior with several potential surrogates [3,57]. A second generation surrogate identified as part of a multi-university research initiative has been tested as part of this work. The surrogate composition is defined in Table 2-1 as *n*-dodecane (40.41%), *iso*-octane (29.48%), *n*-propylbenzene (22.83%) and 1,3,5-trimethylbenzene (7.28%) [57].

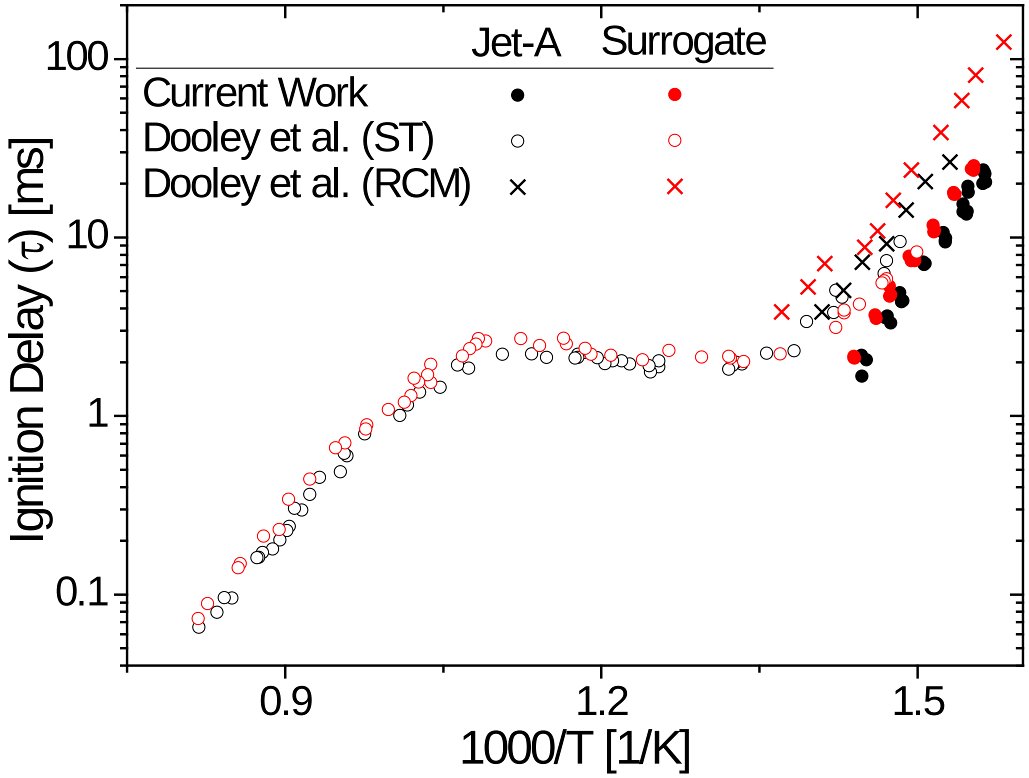

Figure 3-11. Jet-A and surrogate fuel ignition delays.

Ignition delay measurements for Jet-A and the surrogate fuel appear in Figure 3-11, where all measurements have been taken at approximately 20 bar. For conditions that deviate from this pressure, the data have been scaled to 20 bar assuming $\tau \sim p_C$. Figure 3-11 includes data both from this work, and data published by Dooley et al. [57], where the measurements have been made in both a shock tube and a rapid compression machine. At nearly all temperatures tested, the surrogate fuel exhibits a longer ignition delay than the Jet-A. This becomes increasingly evident at low temperatures for the RCM measurements. For the shock tube data at low temperatures, the opposite is true, and the surrogate fuel exhibits a shorter ignition delay than the Jet-A. It does appear that the shock tube measurements and the RCM measurements from this work are trending toward convergence at the lowest tested temperatures, but that the influence of compression may account for the deviation as temperature is increased (see § 3.6.1).

3.8. Conclusion

A new, efficient approach to preparing combustible premixtures with non-volatile fuels in a RCM is described and characterized in this work. In contrast to batch mixture preparation, the DTC approach is used to prepare a reactive mixture directly in the test chamber which enables the use of lower initial temperatures for testing a given equivalence ratio. This benefit minimizes concerns regarding fuel thermal decomposition, and allows testing over a broader set of test conditions. Characterization data regarding the DTC approach has been presented in § 2.2.1, substantiating the claim that the DTC approach is superior to conventional methods at preparing reactive charges in timely manner.

In this study, the autoignition characteristics of JP-8, CHRJ and THRJ fuels have been investigated at low compressed temperatures, low-to-moderate compressed pressures, and at fuel-lean and stoichiometric conditions. The ignition behavior of the HRJ fuels is distinct from the JP-8 at all conditions, with the HRJ fuels exhibiting a more rapid onset of ignition than the JP-8 at a given test condition. The ignition delay measurements of the two HRJ fuels can be distinguished under stoichiometric conditions, although these measurements are generally within the uncertainty range of one another. For fuel-lean mixtures, the ignition delays for the HRJ fuels cannot be distinguished. The data indicate that minor changes in hydrocarbon species distribution have little-to-no effect on synthetic fuel autoignition properties under lean conditions, which may be of importance as the military considers advanced lean-burn technologies and a single fuel for the battlefield.

Kinetic modeling results using a 2-component surrogate (10 % *n*-dodecane/90 % 2-methylundecane) demonstrate that the functional dependence on compressed pressure and equivalence ratio can be represented by the mechanism, but that quantitative agreement is lacking for most test conditions. Good agreement between the data and the simulations can be achieved for the 5 bar, stoichiometric tests at compressed temperatures below the NTC region. The agreement between the data and the predictions may improve within the NTC region by substituting all or a portion of the C_{12} hydrocarbons with lower molecular weight species such as C_{10} hydrocarbons.

Chapter 4:

IGNITION CHARACTERISTICS OF DIESEL AND BIODIESEL FUEL SPRAYS

4.1. Introduction & Background

News outlets and scientific publications abound with evidence of a deteriorating environment and the risk of relying on foreign energy sources [58-60]. A worldwide dependence on fossil fuel energy underlies this problem, and must be addressed by displacing fossil fuels with alternative fuels. The long-term successful replacement of fossil fuels will require new and novel approaches to energy generation. However, short-term solutions must be easily integrated with existing energy infrastructure, namely combustion technology. Biodiesel is an example of a first-generation biofuel which is being actively pursued as a petroleum replacement for these reasons. Biodiesel may be used in existing engines with little to no modification [61], and biodiesel offers many advantages relative to petrodiesel. Biodiesel may be derived from domestic resources [62-63], it is biodegradable and non-toxic [62,64], it has excellent lubricity properties [62,65], and it offers improved safety and handling due to its higher flashpoint (423 K) relative to petrodiesel (337 K) [66,62].

In the U.S., the standard ASTM D6751 governs the specifications of B100 (*i.e.*, biodiesel), in which the composition is described as a blend of “mono-alkyl esters of long chain fatty acids derived from vegetable oils and animal fats” [67]. This definition accommodates some variation in the chemical structure of biodiesel compounds. For example, the lengths and saturation characteristics of the fatty acid chains are not uniform for fatty acid alkyl esters

(FAAE) derived from a single feedstock. In fact, the exact blend of FAAE this is obtained upon transesterification of the vegetable oil or animal fat is often unique for an individual feedstock. The FAAE composition of biodiesel can have profound implications, and frequently, competing interests must be balanced in the selection of a feedstock. It is well-documented that increasing saturation of the fatty acid chain improves the ignition quality of the fuel [68-69], however, the increased saturation is a detriment to the cold flow properties because the saturates exhibit higher crystallization temperatures [70]. ASTM D6751 also accommodates changes in the length and branched nature of the alkoxy chain of the FAAE compounds. The overwhelming majority of biodiesel is derived from oil which is transesterified with methanol, leading to methyl esters. However, alternatives to methyl esters may be used as a way to improve biodiesel cold flow properties. Increasing the length of the alkoxy chain up to four carbons has been shown to improve cold-flow properties while simultaneously improving ignition quality relative to methyl esters [71,59].

An important step to integrating new fuels into existing engines is the ability to model the engine operation using the physical properties and chemical ignition properties of the fuels. The ignition behavior of a fuel is described in a chemical kinetic mechanism which can be coupled with advanced physical models that describe spray breakup, droplet evaporation, and turbulent mixing within the engine. Together, these models comprise computational fluid dynamics simulations which are essential in the engineering process for the development of new engines. It is critical that these models be supplied with accurate kinetic data to achieve meaningful and reliable modeling results. However, for some fuels, kinetic data is limited, which is especially true for non-volatile fuels such as petroleum-based diesel (petrodiesel) and biodiesel. The lack of kinetic data for non-volatile fuels is largely due to the extreme temperatures required to vaporize sufficient fuel quantities to form a premixed charge of fuel and oxidizer gases; these elevated temperatures lead to thermal decomposition of the fuel (*i.e.*, fuel cracking).

Given the challenge of acquiring gas-phase kinetic data for diesel and biodiesel, other approaches must be pursued to supplement modeling efforts by developing a practical understanding of how the spray ignition properties of these fuels respond to changes in engine operating conditions. In this study, a rapid compression machine equipped with a fuel injector is used to compare the spray ignition processes of a reference-grade #2 petroleum-based diesel (D2), and three biodiesels (BD): canola-derived methyl esters (CME), soy-derived methyl esters (SME), and canola-derived butyl esters (CBE). The test conditions created in the RCM for this study are consistent with the diesel engine environment, and the ignition delay and heat release rate data describe the ignition behavior of these fuels under realistic engine conditions. Although the gas phase kinetics are not decoupled from the evaporation process, it has long been recognized that molecular-level fuel properties that influence ignition also affect evaporation [72-73], and this data fully describes the evaporation and ignition behavior that may be seen in an engine. Furthermore, the chemical ignition and evaporation processes in these tests may be partially decoupled through heat loss analysis which makes the data more fundamental in nature by estimating the first appearance of heat release from the fuel as it ignites. A RCM is a useful device for measuring the ignition characteristics of a fuel spray because the test chamber achieves a constant volume prior to ignition, and the elevated test temperatures are generated by compressing the test gas which leaves the wall temperature nearly unchanged. This is in contrast to constant-volume combustion bombs where electrically-heated walls may influence the ignition process in combination with the changes in gas temperature [74].

The objectives of this study are to develop a systematic approach for testing fuel spray autoignition in a RCM and to use the approach to study the ignition characteristics of BD and D2 fuel sprays. Three unique biodiesels will be tested to investigate the influence of fatty ester composition on the autoignition characteristics of biodiesel. Specifically, the influence of two different molecular features will be investigated: (1) the degree of unsaturation in the alkyl chain and (2) the length of the alkoxy chain. Biodiesel derived from soybean oil and from canola-seed oil differ primarily in the degree of unsaturation, with soybean-derived biodiesel containing more esters of the polyunsaturated linoleic acid. These two fuels form the basis for investigating the influence of unsaturation on autoignition characteristics. The influence of the alkoxy chain length is studied by comparing the autoignition characteristics of methyl esters and butyl esters made from the transesterification of canola-seed oil with methanol and *n*-butanol, respectively. The test conditions used to characterize the ignition behavior of these fuels are modeled after the thermal and oxidative conditions seen in low temperature combustion (LTC) strategies of clean diesel technology. Low combustion temperature conditions (< 1800 K) are sought in LTC to avoid NO_X formation that is associated with high combustion temperatures in conventional diesel combustion [75]. Additionally, LTC modes commonly inject fuel early to allow for additional fuel and air mixing time which helps to minimize soot formation during combustion. To prevent the fuel from igniting too early, a large amount of cooled exhaust gas recirculation (EGR) is used to prolong the ignition delay [76]. The EGR reduces the available oxygen in the cylinder, and as such, the test conditions in this study use oxygen fractions of less than 21 %. The results of this study will give insight into the autoignition processes of diesel and biodiesel after injection into low temperature oxidizing atmospheres, and will contribute to the modeling and development of advanced compression ignition engines. It should be noted that the focus of this study is not on the detailed kinetics of biodiesel ignition, but on developing a practical understanding of how changes in biodiesel composition affect the aggregate physical and chemical ignition delay.

Diesel ignition delays have been reported in many prior studies. These data are most commonly measured for fuel sprays in RCMs [77-79], combustion bombs [80-82], or motored engines [83-85]. The earliest known investigation of diesel ignition delays was completed by Wolfer [82] in a combustion bomb. In that work, an ignition delay correlation was proposed in Arrhenius-like form. The proposed ignition delay correlation included the total physical delay time (atomization, vaporization, and mixing) and the chemical delay time. Since then, many studies have appeared in literature with measurements of diesel fuel ignition delay times and some with modified coefficients for the Arrhenius ignition delay correlation [83,86,77,87]. Of particular relevance to this study are the correlations established using data measured in constant volume devices (*i.e.,* RCMs or combustion bombs). The results from these studies will be scaled according to the coefficients proposed by the respective authors, and compared with our experimental results in a subsequent section.

Measurement of diesel fuel ignition delays remains a research topic of interest today. New approaches are being applied to elucidate the gas-phase kinetics of the fuel. A recent study by Haylett et al. [86] employed an aerosol shock tube which uses the incident shock to vaporize the fuel before the reflected shock ignites the mixture. This is a new approach to investigating gas-phase ignition delays of non-volatile fuels and enables the fuel to be tested under well-defined conditions. Additionally, the authors of this work have recently proposed a charge preparation method in the RCM which will enable testing of fuels with volatility that is similar to that of diesel [88].

The autoignition characteristics of biodiesel and its constituent alkyl esters have been the focus of many studies in the literature [89-91]. As previously noted, gas phase ignition delay measurements for fatty acid alkyl esters are particularly difficult to obtain as the length of the fatty acid alkyl chain or alkyl ester chain grows. For example, creation of a stoichiometric mixture (p_0 = 1 bar, X_{O2} = 0.21), of methyl decanoate (C_{10} methyl ester) in air requires an initial temperature near T_0 = 110 °C. The use of initial temperatures in gross excess of this leads to concerns regarding fuel cracking and seal degradation, and in general, has prohibited the investigation of a meaningful range of test conditions for the high molecular weight methyl esters in biodiesel. Studies in literature regarding biodiesel combustion characteristics are frequently completed in engines where physical and chemical events are linked, and occur in a temporally varying volume [92-94]. These studies also frequently focus on applied issues such as emissions. Studies on the reactivity of biodiesel have commonly reported cetane numbers (CN) for a wide variety of FAAE components and blends that represent real biodiesels. The cetane number represents the ignition propensity of a fuel, where a higher cetane number corresponds to a shorter ignition delay. The cetane number of a fuel may be determined using a Cooperative Fuels Research (CFR) engine according to ASTM D613 [95]. Alternatively, the derived cetane number may be determined using an Ignition Quality Tester (IQT) in accordance with ASTM D6890 [53].

A review article by Graboski and McCormick [96] compiled cetane numbers for methyl and ethyl esters of C_8 to C_{18} fatty acids which demonstrated specific trends in cetane number with changes in molecular structure. The data, which was compiled from the original works of Freedman and Bagby [97], Klopfenstein [98], and Knothe et al. [99], showed that cetane number increases with fatty acid chain length and decreases with unsaturation in the fatty acid chain. Concerning the alkoxy chain length (*e.g.*, methyl vs. ethyl), no conclusive trend existed.

Numerous papers have been published under the sponsorship of the U.S. Department of Agriculture, which describe the relationship between fatty acid alkyl ester molecular structure and properties such as cetane number, oxidative stability, melting point, boiling point, viscosity, cloud point, pour point, and cold filter plug point [70,100-108]. The studies regarding cetane number typically attribute first-authorship or sole-authorship to Knothe, and are discussed here in some detail. Knothe has published a series of papers regarding the optimization of biodiesel fuel properties, specifically to address deficiencies in the cold flow behavior and the oxidative stability of biodiesel relative to petrodiesel [102,109,103-104,110], Knothe proposes five methods to improve biodiesel properties, among which are modifying the fatty acid profile and changing the alcohol used in the transesterification process [110]. Changing the fatty ester composition of biodiesel in this manner requires caution because molecular structure changes that improve one property may lead to deterioration in another fuel property [103]. Methyl oleate, for example, is known to possess superior ignition quality characteristics relative to natural biodiesels, and has been proposed for enrichment in engineered biodiesels by Bringe [111] and Kinney et al. [112]. However, in spite of the increased cetane number of methyl oleate (CN ~ 57.9) relative to biodiesel, Knothe reports data that indicate a failure of methyl oleate to meet the oxidative stability requirements for biodiesel, as prescribed by ASTM D6751 [103]. This illustrates the challenge of optimizing biodiesel properties while maintaining compliance with the required specifications. Other work by Knothe [105]. includes extensive cetane number characterization of fatty esters using an IQT. The study concluded that unsaturation in the fatty acid chain had the most dramatic influence on the reduction in cetane numbers relative to other molecular structure changes. Furthermore, branching in the alkoxy chain which improves cold flow properties was reported to have no significant influence on the ignition properties of the fatty ester.

Ignition delay times have been measured for soybean-derived fatty acid methyl esters (FAME) in a constant volume tube furnace by Vaughn et al. [113] and Marchese et al. [114]. In these experiments, a single droplet of fuel was injected into a heated furnace and tracked photographically until the onset of OH* chemiluminescence indicated ignition. In the work of Vaughn et al. [113], methyl oleate is proposed as a biodiesel surrogate because it exhibited ignition delay times that were similar to soy FAMEs over a range of furnace temperatures. The subsequent experiments of Marchese et al. [114] were performed under microgravity conditions where the measured ignition delays closely matched predictions from a 1-D numerical model integrated with a skeletal chemical kinetic mechanism for methyl decanoate [115].

A recent publication by Schönborn et al. [94] investigated the influence of FAAE molecular structure on diesel combustion. Schönborn et al. considered the diesel combustion characteristics of single molecule FAAE with varying fatty acid chain lengths, degrees of unsaturation, and alkoxy chain lengths, and additionally tested blends of these alkyl esters meant to reproduce the composition of FAMEs produced from rapeseed oil, palm oil, jatropha oil, and tallow. The results of Schönborn et al. demonstrated that increasing the length of the fatty acid chain led to shorter ignition delays. The tests regarding unsaturation in the fatty acid chain supported previously published cetane number data [71,99,105] by showing an increase in ignition delay with increasing unsaturation. The effect of alkoxy chain length on diesel combustion was investigated by testing methyl oleate and ethyl oleate. For this modest change in molecular structure, a marginal reduction in ignition delay was observed for ethyl oleate relative to methyl oleate.

Table 4-1. Fatty acid composition of soybean and canola biodiesels and derived cetane numbers of methyl and butyl ester biodiesel components

Fatty Acid Ester	Canola BD Composition [59,116]	Soybean BD Composition [117]	Methyl Ester DCN [105]	Butyl Ester DCN [105]
SATURATED				
Palmitic Acid (C16:0)	2 – 6 % (4 %)	6 – 10 % (8 %)	85.9	91.9
Stearic Acid (C18:0)	1 – 3 % (3 %)	2 – 5 % (4 %)	101.01	92.5
UNSATURATED				
Oleic Acid (C18:1)	52 – 67 % (60 %)	20 – 30 % (24 %)	59.3	92.5
Linoleic Acid (C18:2)	16 – 31 % (23 %)	50 – 60 % (58 %)	38.2	53.5
Linolenic Acid (C18:3)	6 – 14 % (10 %)	5 – 11 % (5 %)	22.7 [99]	26.8 [102]
Natural Biodiesel CN	FAME: 47.9 – 56 [118-120]	FAME: 48.7 – 55.9 [118,121-122]		

Klopfenstein [71] used a CFR engine to investigate the cetane numbers of saturated fatty acid esters of various molecular weights. The molecular weight of the esters was altered by increasing the fatty acid chain length (C_8 – C_{18}) and by changing the type of alcohol used in the transesterification. The cetane number was found to increase nonlinearly with growth in the fatty acid chain, and Klopfenstein notes that this is in contrast to hydrocarbons which may exhibit a linear proportionality between cetane number and normal paraffinic chain length. The data reported by Klopfenstein also indicates that molecular weight changes due to fatty acid chain modification more strongly influence cetane number than identical molecular weight changes that are effected in the alkoxy chain.

Data from the aforementioned studies have been compiled in Table 4-1, which describes the cetane numbers [102,99,105] for the methyl and butyl esters of the fatty acids comprising

Table 4-2. Biodiesel (BD) and petrodiesel fuel properties

Property	Canola BD (Methyl Ester)	Soybean BD (Methyl Ester)	Canola BD (Butyl Ester)	Petrodiesel
Molecular Formula (estimated)	$C_{18.82}H_{34.96}O_2$	$C_{18.71}H_{34.31}O_2$	$C_{21.81}H_{40.92}O_2$	$C_{14}H_{25}$
Heat of Combustion (LHV)	37.3 MJ/kg [119]	37.3 MJ/kg [122]	38.5 MJ/kg	42.98 MJ/kg [94]
Density (@ 15 $^{\circ}$C)	0.883 g/ml [123]		--	0.834 g/ml [94]
Viscosity (@ 40 $^{\circ}$C)	4.34 mm^2/s [123]	4.18 mm^2/s	--	2.56 mm^2/s [94]
Surface Tension	23.6 mN/m [124]		--	25.2 mN/m [125]
Boiling Range	338 – 366 $^{\circ}$C [116]		--	161 – 371 $^{\circ}$C [126]
Cetane Number	47.9 – 56 [59]	48.7 – 55.9	--	47 – 49.8 [127,94]

soybean biodiesel and canola biodiesel. As noted by previous studies, three general trends can be observed in the data: cetane number increases with fatty acid chain length, decreases with additional unsaturation in the fatty acid chain, and usually increases with alkoxy chain length. A sharp reduction in cetane number is noted between methyl oleate (59.3) and methyl linoleate (38.2). This is noteworthy because methyl oleate is the predominant component of canola biodiesel, while methyl linoleate is the predominant component of soybean biodiesel. We may expect this to lead to a marked change in ignition quality characteristics for natural biodiesel blends derived from these two feedstocks, yet the reported cetane numbers of canola biodiesel (47.9 – 56) and soybean biodiesel (48.7 – 55.9) are remarkably similar. Cetane number, however, is not fully informative of the ignition characteristics of a fuel spray because data is collected for a single test condition. This consideration further motivates this study which assesses the autoignition characteristics of biodiesel fuel sprays at temperatures between 676 and 816 K and at two different oxygen concentrations.

4.2. Test Fuels

Spray ignition delays were measured for canola-derived methyl esters (CME), canola-derived butyl esters (CBE), soybean-derived methyl esters (SME), and petroleum-based diesel (D2). The butyl esters were formed by transesterifying canola oil with *n*-butanol, hence there is no branching in the alkoxy chain of the butyl esters.

As previously described in Table 4-1, the fatty acid composition is known to vary significantly between canola biodiesel and soy biodiesel. Additional properties for all of the tested fuels appear in Table 4-2. All of the biodiesels are comprised of the same five primary fatty acid alkyl esters, and the structures of these esters appear in Table 4-3. However, esters of the monounsaturated oleic acid predominate in canola biodiesel, while the majority of soy biodiesel is comprised of esters of the polyunsaturated linoleic acid. The reaction zone temperature calculations that are described in § 4.4.1 require molar fuel composition as an input. The input compositions used in this study have been estimated for canola and soy biodiesels and

Table 4-3. Molecular structures of alkyl esters comprising the tested natural biodiesels

Component Name	Molecular Structure
Alkyl Palmitate *C16:0*	
Alkyl Stearate *C18:0*	
Alkyl Oleate *C18:1*	
Alkyl Linoleate *C18:2*	
Alkyl Linolenate *C18:3*	

Methyl esters, $n = 0$; butyl esters, $n = 3$

appear in parentheses in Table 4-1 for each fatty ester. These compositions result in average molecular formulae of $C_{18.71}H_{34.31}O_2$ for SME, $C_{18.82}H_{34.96}O_2$ for CME, and $C_{21.81}H_{40.92}O_2$ for CBE. These estimations are consistent with other studies in the literature [61,59,128], and enable the fuels to be tested at similar carbon concentrations. Starting with the desired bulk equivalence ratio of $\phi = 0.25$, the formulae are used to calculate the required injection mass, and they enable testing to be done on an approximately constant carbon concentration basis.

4.3. Experimental Test Conditions

The effect of temperature on the ignition delay and heat release rate of D2 and biodiesel fuel sprays has been studied at various temperatures, oxygen concentrations and fuel concentrations as described in Table 4-4. Tests were conducted at reaction zone temperatures of $676 \text{ K} \leq T_{RZ} \leq 816 \text{ K}$ using oxygen mole fractions of $X_{O2} = 0.12$ and $X_{O2} = 0.18$. All tests have been completed using a compressed pressure of $p_c = 30$ bar and a bulk equivalence ratio of $\phi = 0.25$, which is calculated assuming the fuel is fully vaporized and mixed with the oxygen and diluent gases. The bulk equivalence ratios have been calculated by assuming average formulas described in Table 4-2. The equivalence ratios are calculated on an oxygen basis using the 12 % and 18 % oxygen fractions contained in the test mixtures. The RCM was configured with a compression ratio of 12.7:1. The compressed temperatures have been adjusted by altering the composition of the diluent gas (nitrogen:argon ratio), and by changing the injection timing. The details of this hybrid approach for generating the test temperature is described and characterized in §§ 2.3.1 – 2.3.2. As noted, all gas mixtures contained either 12 % or 18 % oxygen, while the diluent gases nitrogen and argon comprised the balance of the mixture. Argon accounted for 0 %, 20 % and 40 % of the diluent gas composition, with increases in the argon mole fraction bringing about a corresponding increase in compressed temperature. For each diluent gas composition used, an additional set of compressed temperatures were tested by allowing the gas mixture to cool for varying amounts of time after compression before commencing the fuel injection.

Table 4-4. Summary of test conditions for experiments

All Tests	Compressed pressure	$p_c = 30$ bar
	Bulk equivalence ratio	$\phi = 0.25$
	Compression ratio	$CR = 12.7{:}1$
	Fuel Temperature	$T_{fl,0} = 298$ K
Fuel Injector	Fuel Pressure	$p_f = 100$ bar
	Number of Holes	7
	Hole Diameter	$d = 200$ μm
	Discharge Coefficient	$C_D = 0.33$

	Diluent ratio	O_2 mole fraction	Fuel mass injected	Reaction Zone Temperature	Injection time after TDC
Mix #	$N_2/(N_2 + Ar)$	X_{O2}	m_f	T_{RZ}	$t_{inj,ATDC}$
Mix 1	1.0	0.12	SME: 9.0 – 10.5 mg CME: 9.0 – 10.4 mg CBE: 8.8 – 10.2 mg D2: 7.7 – 9.0 mg	683 – 714 K	9.1 – 129.1 ms
Mix 2	1.0	0.18	SME: 13.2 – 15.4 mg CME: 13.1 – 15.4 mg CBE: 12.9 – 15.0 mg D2: 11.4 – 13.3 mg	676 – 708 K	3.6 – 100.3 ms
Mix 3	0.8	0.12	SME: 9.0 – 10.2 mg CME: 8.9 – 10.1 mg CBE: 8.7 – 10.0 mg D2: 7.7 – 8.8 mg	720 – 748 K	23.8 – 137.2 ms
Mix 4	0.8	0.18	SME: 13.1 – 15.0 mg CME: 13.0 – 14.9 mg CBE: 12.8 – 14.5 mg D2: 11.3 – 12.9 mg	711 – 741 K	10.7 – 86.9 ms
Mix 5	0.6	0.12	SME: 7.9 – 9.4 mg CME: 7.9 – 9.4 mg CBE: 7.7 – 9.2 mg D2: 6.8 – 8.1 mg	771 – 816 K	6.3 – 96.4 ms
Mix 6	0.6	0.18	SME: 12.3 – 14.4 mg CME: 12.2 – 14.3 mg CBE: 12.0 – 13.3 mg D2: 10.6 – 12.4 mg	751 – 791 K	6.9 – 89.6 ms

4.4. Data Analysis and Uncertainty

4.4.1. Reaction Zone Temperatures

The presentation of meaningful ignition delay and heat release rate data requires well-defined temperatures for the gas-environment in which the data is measured. Calculation of the core gas temperature in a RCM is straightforward, and typically proceeds through application of the adiabatic core hypothesis. As noted in § 2.3.1, this method assumes the existence of a core gas region that is compressed adiabatically, and that actual heat losses only influence gas temperature near the cylinder wall. In this study, a creviced piston has been used to promote the formation of an adiabatic core which we consider valid until the injection begins. As fuel is injected into the combustion chamber, the core deteriorates and the calculated core temperature no longer adequately describes the test condition. As the liquid fuel droplets penetrate the hot gas, heat is transferred to the cool droplets for heating and vaporization. The energy required for this process reduces the temperature in the region where fuel vapor mixes with oxidizer and diluents gases. We refer to this region as the reaction zone.

Temperature calculations in the reaction zone (T_{RZ}) are based on the conservation of energy, with the adiabatic mixing assumption described by El-Wakil et al. [129] and Espey et al. [130]. As thermodynamic equilibrium is established, temperatures in the reaction zone can be calculated as d

$$\int_{T_{RZ}}^{T_{g,0}} C_{v,g}\,dT = \frac{n_f}{n_g}\left[\int_{T_{fl,0}}^{T_{int}} C_{v,l}\,dT + h_{v,T_{int}} + \int_{T_{int}}^{T_{RZ}} C_{v,fv}\,dT\right] \tag{4-1}$$

The left-hand side of Equation 4-1 represents the total decrease in thermal energy of the oxidizer and diluent gas mixture, which is calculated by integrating the heat capacity of the gas mixture ($C_{v,g}$) between the reaction zone temperature and the core-gas temperature at the time the injection begins ($T_{g,0}$). The adiabatic core gas temperature at SOI is used as $T_{g,0}$ in Equation 4-1. On the right hand side, the corresponding increase in thermal energy of the fuel is represented by the term in brackets, which considers contributions from the liquid fuel heat capacity ($C_{v,l}$), the enthalpy of vaporization ($h_{v,Tint}$), and the fuel vapor heat capacity ($C_{v,fv}$). The liquid fuel heat capacity is integrated between the initial fuel temperature ($T_{fl,0}$) and the intermediate temperature (T_{int}) at which vaporization occurs. The amount of thermal energy exchanged between the gas mixture and fuel is proportional to the ratio of fuel moles (n_f) to gas mixture moles (n_g). T_{RZ} is numerically calculated using Equation 4-1, and for the tests presented in this study, reaction zone temperatures were 16 – 37 K lower than the initial core-gas temperatures calculated at the SOI.

4.4.2. Ignition Delay Definition

In general, the ignition delay of a fuel is defined as the time required to autoignite after the fuel has been exposed to autoignition conditions. In our study of fuel spray ignition, we have defined two unique events during the ignition process that characterize the ignition behavior of the fuel. In the following, an approach is described that uses experimental pressure data to identify these ignition delay periods.

After fuel injection begins, the pressure in the cylinder continues to decrease due to wall heat losses and fuel evaporation. This is illustrated in Figure 4-1 where the pressure loss is accelerated after fuel injection at t = 0. Immediately following this time, the heat release rate

(dQ_C/dt) calculated using the heat loss model in § 4.4.4 is less than zero, indicating energy is lost not only to the walls, but also to the fuel droplets. At the onset of ignition, fuel energy is released and dQ_C/dt begins to rise. The time at which dQ_C/dt becomes positive marks the first ignition delay period of interest, τ_1, which is illustrated in Figure 4-1. τ_1 represents the time at which more energy is being released from fuel than is being consumed for vaporization and warming. It should be noted that τ_1 is not coincident with $dp/dt = 0$ because wall heat losses have been

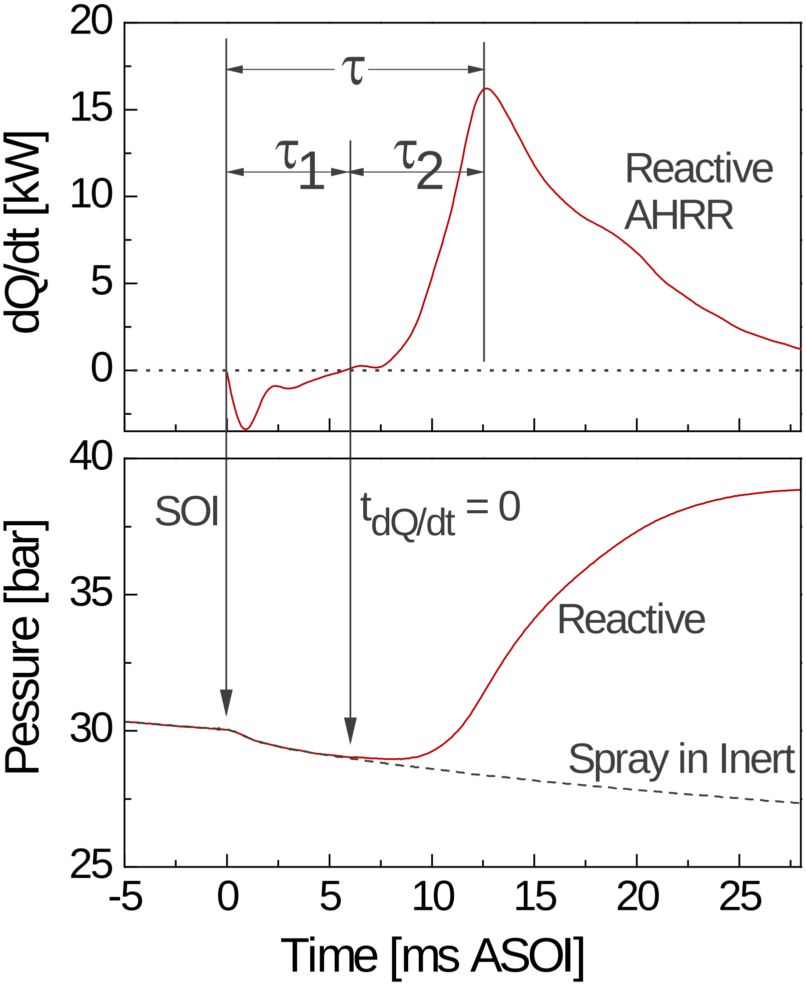

Figure 4-1. Ignition delay definition for spray ignition studies.

accounted for in the heat loss model. This is evident in Figure 4-1 where the minimum pressure after injection occurs subsequent to τ_1. The second ignition delay period of interest occurs some time, τ_2, after τ_1 when the maximum rate of heat release due to combustion is observed. The sum total of these time periods, $\tau = \tau_1 + \tau_2$ is referred to as the total ignition delay and is illustrated in Figure 4-1. All ignition delays reported in this work have been calculated using these definitions. Within this definition, it is important to consider that a portion of the ignition delay time is devoted to fuel spray warming, breakup, and evaporation in the process of forming a combustible mixture. Based on a review of literature [129,131], we would expect this requires 2 – 5 ms. Analysis of Figure 4-1 suggests it is near 2 – 3 ms, where the most intense heat loss event due to the spray is seen to conclude.

4.4.3. Thermophysical Properties & Group Contribution Methods

The reaction zone temperature and heat release rate calculations presented in the following sections rely heavily on thermophysical property data, many of which are unavailable for the methyl esters that comprise biodiesel. Similarly, diesel is a blend of numerous hydrocarbons. Its exact composition is unknown which prevents the use of the thermodynamic property databases which provide data for individual molecules.

Biodiesel that results from the transesterification of a triglyceride with alcohol is primarily comprised of five methyl esters: alkyl palmitate, alkyl stearate, alkyl oleate, alkyl linoleate, and alkyl linolenate. The respective fractions of each of these alkyl esters are estimated to be 4 %, 3 %, 60 %, 23 %, and 10 % for the canola-derived biodiesels, and 8 %, 4 %, 24 %, 58 %, and 6 % for the soybean-derived biodiesels [59]. These compositions have been used to estimate the average molecular formulae described in Table 4-2. A limited amount of thermophysical property data is available for these biodiesel components, which includes critical temperature and enthalpy of vaporization data for the methyl esters of palmitic, stearic and oleic acid [132]. Liquid heat capacity data is available for all of the methyl ester components; however, the experimental data is at standard temperatures which do not match the test conditions in the RCM. When possible, these experimental data have been used to calculate reaction zone temperatures. The unavailable thermophysical property data has been estimated using group contribution methods which assume that the properties of a substance can be estimated by summing the contributions of polyvalent atoms (*i.e.*, groups) within the molecule [133]. The gas-phase heat capacity for all biodiesel components has been estimated using the group additivity method of Benson [133]. The method yields temperature-dependent heat capacity data for individual chemical species and is widely used in literature for estimating heat capacity data [134-136]. The liquid-phase heat capacities have been estimated using the method of Růžička and Domalski [137] and the assumption that the constant-volume heat capacity and constant-pressure heat capacity are equivalent for the liquid fuels. In the original work by Růžička and Domalski [137], correlation predictions for esters are compared with experimental data, and the predictions were within 3 % of the experimental value for greater than 80 % of the 85 esters tested. The enthalpies of vaporization have been estimated with the method of Tu and Liu [138] which utilizes a 3-parameter fit coupled with critical temperature data for the species of interest. Tests by Tu and Liu [138] indicate the method predicts the enthalpy of vaporization of esters within 5.7 % of the experimental value. The group contribution method proposed by Constantinou and Gani [139] has been used to estimate critical temperatures where experimental data is not available. The method of Constantinou and Gani may be expected to predict critical temperatures within 5 % of the experimental value.

For diesel fuel, where the exact composition is unknown, we have used the thermodynamic property correlations provided in the appendix of Sazhin et al. [140]. The appendix provides correlations and original references for gas-phase heat capacity [141], liquid-phase heat capacity [141], and enthalpy of vaporization [142]. Equivalence ratios for the tests have been determined assuming an average molecular formula of $C_{14}H_{25}$.

4.4.4. Single-Zone Heat Loss Model

A zero-dimensional heat loss model was developed for the RCM to analyze the apparent heat release rates (AHRR) for biodiesel and diesel fuel in the RCM. The spray and ignition processes occurred under constant volume conditions in the RCM. Thus, by assuming ideal gas behavior, the first law of thermodynamics may be written as

$$\frac{dQ_C}{dt} = \frac{C_V V}{R_u}\frac{dp}{dt} - \frac{dQ_W}{dt}, \tag{4-2}$$

where dQ_C/dt is the apparent rate of heat release due to combustion, C_V is the constant-volume heat capacity of the reacting gas mixture, V is the volume at the end of compression, R_u is the universal gas constant, dp/dt is the time derivative of the pressure and dQ_W/dt is the rate of heat loss to the walls. In the first term on the right-hand side of Equation 4-2, C_V is the only parameter which is not determined directly from experimental data. Instead, C_V is calculated from an average cylinder temperature that is estimated using the ideal gas law and known pressure data. The second term on the right-hand side requires a heat loss model to estimate the rate at which energy is lost through the walls of the combustion chamber. By considering convective and radiative effects, the heat loss can be estimated as

$$\frac{dQ_W}{dt} = A \cdot h_c(T - T_W). \tag{4-3}$$

The constitutive equation presented in Equation 3-3 uses Newton's law of cooling for convection losses. The convective heat losses are directly proportional to variations between the mean gas temperature (T) and wall temperature (T_W). The proportionality is dependent on the surface area (A) of the inside of the combustion chamber and the instantaneous heat transfer coefficient (h_c). It should be noted that the initial heat loss model developed included a radiation heat loss component of the form described by Annand [143]. The radiative component has been omitted from the final model because it was of negligible magnitude at our test conditions. Calculations indicated that less than 0.5 % of the heat loss occurred through radiation.

Defining the instantaneous heat transfer coefficient, h_c, in Equation 3-3 is challenging due to the evolving conditions in the RCM during the post-compression period. This challenge is not unlike that encountered in modeling heat losses from internal combustion engines where field gradients are even more severe than experienced by the RCM charge. Many useful correlations have been proposed [143-145] for modeling heat losses in engines, and we have chosen the well-known Hohenberg model [144] from among these as a starting point to estimate h_c. The original Hohenberg model has been applied with some success to model heat losses in homogenous charge compression ignition (HCCI) engines [146], and a prior study has examined the ability of the model to predict heat losses from a rapid compression expansion machine [147].

In the original work by Hohenberg [144] a correlation is developed for the heat transfer coefficient, h_c, as

$$h_c = C_1 \frac{p\left(\bar{v}_p + C_2\right)^{0.8}}{V_C^{0.06} T^{0.4}}, \tag{4-4}$$

where p is the cylinder pressure, $\bar{v}_p$ is the mean piston speed, V_c is the cylinder volume, and T is the mean gas temperature. Both C_1 and C_2 are arbitrary constants for which Hohenberg proposed values of 130 and 1.4, respectively. The mean piston speed in Equation 4-4 is intended to capture the influence of charge turbulence on heat loss. Although the piston in the RCM is at rest during the modeling period, charge motion will still influence heat loss. Both Mittal and Sung [15] and Würmel and Simmie [26] have published numerical studies on fluid motion in a RCM with a creviced piston. Together, these studies indicate that the peak gas velocity in the combustion chamber occurs when the piston is at TDC and quickly dissipates. Simulation results from Mittal and Sung [15] show that for compressed pressures of 39.9 bar, using a creviced piston, the peak gas velocity decreases by 78 % and 95 % at 20 ms and 80 ms after TDC, respectively. This rapid dissipation of gas motion is markedly different than conditions in an engine, and has prompted the replacement of $\bar{v}_p$ in Equation 4-4 with an exponentially decreasing velocity value, thus updating the original Hohenberg expression as

$$h_c = C_1 \frac{p\left(\bar{v}_p e^{C_2} + C_3\right)^{0.8}}{V_C^{0.06} T^{0.4}}. \tag{4-5}$$

The mean piston speed in Equation 4-5 is calculated using the piston speed data calculated during the compression stroke in the RCM. All other parameters are as described for Equation 4-4. The constants C_1, C_2 and C_3 in Equation 4-5 were determined using 25 non-reactive gas tests (*i.e.,* no fuel injected) of varying compressed temperatures, compressed pressures, and mixture heat capacities. For these tests, where no combustion occurred, radiation was assumed to be negligible. Using the pressure data from the non-reactive tests, a non-linear optimization scheme was used to determine the values of C_1, C_2, and C_3 which yield the best fit for

$$\frac{C_v V}{R_u}\frac{dp}{dt} \cong A \cdot C_1 \frac{p\left(\bar{v}_p e^{C_2} + C_3\right)^{0.8}}{V_C^{0.06} T^{0.4}} (T - T_w). \tag{4-6}$$

For these calculations, mean gas temperatures were used, and the walls were assumed to be at a constant temperature which was equal to the initial temperature of 298 K for all tests. The analysis yielded values of C_1 = 29.5, C_2 = 51.2, and C_3 = 0.6. While employing these constants, we caution that Hohenberg [144] described the importance of considering combustion of when

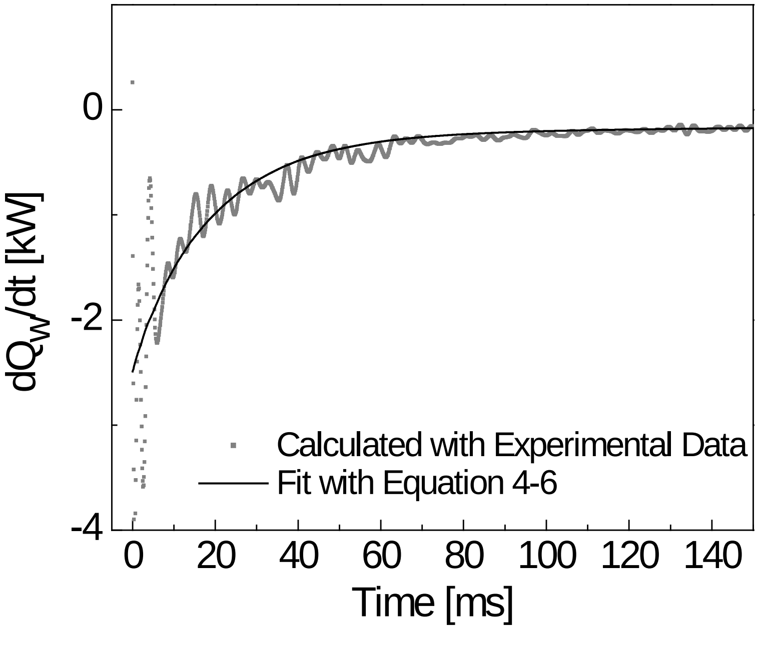

Figure 4-2. Sample wall heat loss calculations from experimental data and the corresponding fit calculated using Equation 4-6.

calibrating the model constants. The constants we present have been calibrated using non-reactive tests for straightforward application of Equation 4-2 even though this may lead to some inaccuracy in the values of the optimized constants. Figure 4-2 compares a heat loss profile calculated using $\frac{dQ_W}{dt} = \frac{C_v V}{R_u}\frac{dp}{dt}$ with the heat losses calculated using the optimized coefficients in $\frac{dQ_W}{dt} = A \cdot C_1 \frac{p\left(\bar{v}_p e^{C_2} + C_3\right)^{0.8}}{V_C^{0.06} T^{0.4}} \left(T - T_W\right)$. It is emphasized that the model comparison and its basis are derived from heat loss calculations using the First Law of Thermodynamics, not experimental measurements of the heat flux. The empirically-determined fit does not reproduce the inflection point where the maximum rate of heat loss is observed shortly after TDC; however, the agreement between the two is very good for $t \geq 5$ ms after TDC, where all injections for this study have occurred. The lack of agreement during the first 5 ms after TDC is insignificant because the wall heat loss calculations for this time period are not used in the AHRR calculations. The h_c correlation has been used to estimate wall heat losses for all ignition tests which allows calculation of the AHRR using

$$\frac{dQ_c}{dt} = \frac{C_v V}{R_u}\frac{dp}{dt} - A \cdot C_1 \frac{p\left(\bar{v}_p e^{C_2} + C_3\right)^{0.8}}{V_C^{0.06} T^{0.4}} \left(T - T_W\right). \tag{4-7}$$

4.4.5. Experimental Uncertainty

The preceding sections have outlined an approach for interpreting the raw pressure data recorded in the RCM. The approach is not posed as a replacement for a more rigorous treatment of the problem which would require the application of advanced optical diagnostics and CFD model development. Such treatment is outside the scope of this study, but it is important to assess the accuracy of the analysis. In this section, we present a discussion of the uncertainty in our analysis, particularly with respect to characterizing the charge temperature and equivalence ratio.

The compressed temperature calculations we consider valid until the start of injection depend on input data from a T-type thermocouple (Omega), an absolute pressure manometer (MKS Instruments Baratron 626B), and a piezoelectric pressure transducer (Kistler 6125B). The T-type thermocouple is used for the initial RCM temperature measurements and is specified to have an error limit of 1 °C in this temperature region. For our p_C = 30 bar test condition, we estimate the uncertainty in the compressed pressure to be ±0.5 %. We have used these data to estimate the maximum uncertainty in the compressed temperature calculations as ±5 K. These compressed temperature calculations serve as the input to the reaction zone temperature calculations described by Equation 4-1. The reaction zone temperature is seen to depend on fuel mass injection data and thermophysical property data. Data acquired during calibration of the fuel injector indicates that the mass of fuel injected varies by ±3.0 % (ϕ = 0.25 ± 0.01). By considering the accuracy of the group contribution methods discussed in § 4.4.3, we estimate the maximum uncertainty in the reaction zone temperature calculations to be ±8 K. Assigning this uncertainty still ignores the fact that we cannot expect that a homogeneous temperature exists in the core of the chamber after the fuel spray occurs; however, full multi-dimensional characterization of the temperature field is outside the scope of the applied data presented in this work. The present study requires assignment of a system reference temperature for presenting the ignition delay data, and the authors have chosen the reaction zone temperature for this purpose. Although the reaction zone temperatures are not validated here, they are based on well-established analysis methods from literature, and the data presented in Figure 2-17. supports use of the reaction zone temperature as the reference temperature for studying spray ignition in the RCM.

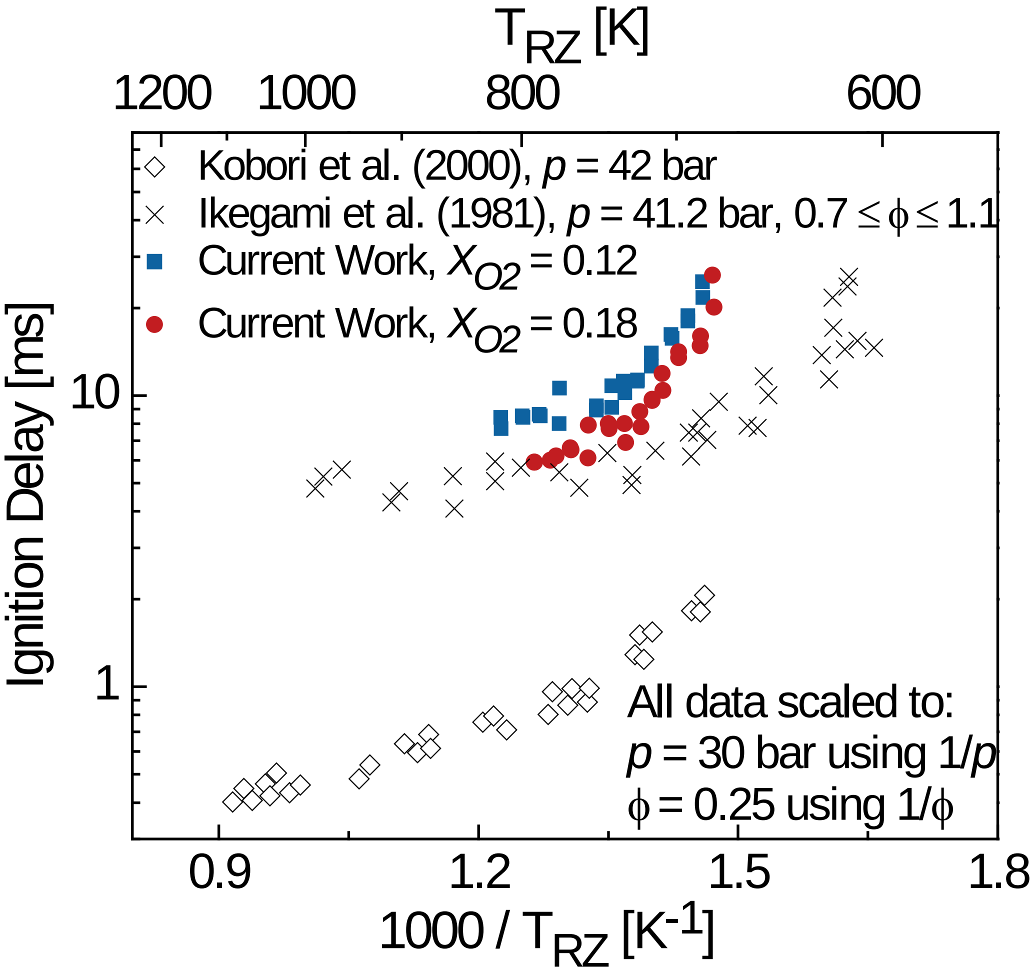

Figure 4-3. Comparison of diesel ignition delays with data published in the literature.

4.5. Experimental Results

4.5.1. Comparison of Diesel Ignition Delay Measurements with Literature Data

Figure 6 shows a comparison of the D2 ignition delay measurements recorded for this study with other measurements published in literature. All the published diesel ignition delays were measured using an oxygen mole fraction of $X_{O2} = 0.21$, while the tests reported for this work used oxygen mole fractions of $X_{O2} = 0.12$ and $X_{O2} = 0.18$. The measurements for all of the studies were taken in a RCM, although small variations in ignition delay definition exist between the studies. Despite this difference, a comparison among the datasets is useful to view the overall trends occurring within the data and to check for logical consistency. All of the data appearing in Figure 4-3 have been scaled to p_C = 30 bar and ϕ = 0.25, using the pressure scaling of $1/p$ and equivalence ratio scaling of $1/\phi$ that are frequently referenced in literature [83,86-87,148]. The actual test conditions used in each of these studies appears within the legend of Figure 4-3.

The ignition delays recorded for this work are a full order of magnitude longer than those reported by Kobori et al. [78] Despite the higher oxygen concentration (21 %) used by Kobori et al., we don’t expect this would account for all of the difference, especially considering the relatively small ignition delay reduction that is observed between the X_{O2} = 0.12 and X_{O2} = 0.18 datasets reported in this study. However it is noted that Kobori et al. do not describe the equivalence ratio used for their testing, which may contribute to the disparity in the data. The measurements of Ikegami et al. [77] appear to be much more consistent with the measurements reported here. The shorter ignition delays reported by Kobori et al. are likely a result of shorter evaporation and mixing times that arise due to the finer atomization that can be achieved with a high pressure injector. The low pressure injectors used for this study and by Ikegami et al. [77] produce larger droplet sizes which lead to a longer physical delay time during which evaporation and mixing occur.

Taken as a whole, the aggregate data exhibit a roll-off in the ignition delay near 800 K where the ignition delay becomes less sensitive to changes in temperature. This behavior suggests the presence of a negative temperature coefficient region where increases in temperature lead to an increase in the chemical ignition delay time. The measurements from this study seem to be consistent with diesel ignition delays reported in literature, and there is potential evidence of NTC behavior near the upper temperature limit that we have reported,

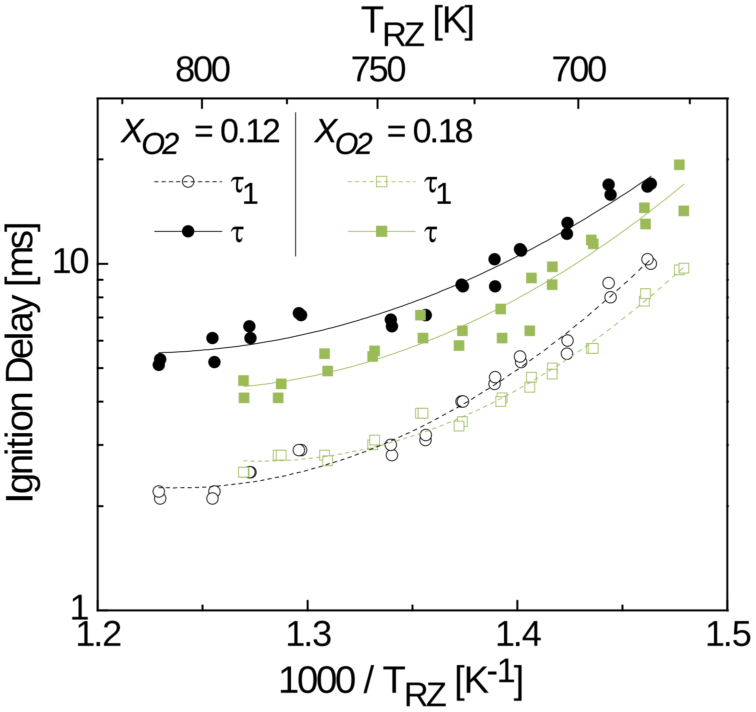

Figure 4-4. Ignition delay measurements (τ_1 and τ) for fuel CME sprays in oxidizing environments with X_{O2} = 0.12 and X_{O2} = 0.18.

where little change in the ignition delay is observed with changes in reaction zone temperature. Additional measurements at higher temperatures and higher oxygen concentrations may provide a more complete comparison, and additional confirmation of NTC behavior in the spray ignition process.

4.5.2. Effect of Reaction Zone Temperature on D2 and BD Ignition Delays

Canola Methyl Esters

The ignition delay data, τ_1 and τ, measured for CME with X_{O2} = 0.12 and X_{O2} = 0.18 are shown in Figure 4-4. For the tests using X_{O2} = 0.12, the first ignition delay period varied between 2.1 ms $\leq \tau_1 \leq$ 10.3 ms, while the total ignition delay varied between 5.1 ms $\leq \tau \leq$ 17.0 ms. For the tests using X_{O2} = 0.18, the first ignition delay period varied between 2.5 ms $\leq \tau_1 \leq$ 9.7 ms, while the total ignition delay varied between 4.1 ms $\leq \tau \leq$ 19.3 ms. There is evidence of potential NTC behavior near the upper limit of the reaction zone temperatures that were tested. This can be observed near T_{RZ} = 770 K where both the τ_1 and τ data become less sensitive to increases in temperature. The evidence of NTC behavior in a spray ignition measurement was not fully anticipated because the physical and chemical ignition delays are tightly convolved. For some test conditions, it may be expected that small changes in the chemical ignition delay would be overwhelmed by the physical effects. The diesel spray ignition study of Kobori et al. [78] did report NTC behavior for some of the spray ignition measurements, but only for injector orifice sizes between 25 – 100 μm. The orifice size of the injector used for this study approaches 200 μm, and Kobori et al. [78] did not observe NTC behavior when testing with a similar orifice size. Another important observation from Figure 4-4 is that the fuel and oxygen concentrations have an obvious influence on the total ignition delay period. However, the τ_1 data for both oxygen concentrations are remarkably similar, and the two datasets are not easily distinguished from one another over the tested temperature domain. We do, however, see separation in the two datasets near the lower limit of tested temperatures. We interpret this finding to mean that fuel kinetics play an increasingly important role at lower temperatures, but that at higher temperatures, the first ignition delay period may be dominated by physical transport processes such as spray breakup and evaporation. Near T_{RZ} = 750 K, we observe a crossover in the two τ_1 datasets. Within the precision of the data, we cannot say this occurrence has significance, but it does motivate future studies at higher temperatures and additional oxygen mole fractions. The increased availability of oxygen, however, does subsequently lead to more rapid fuel oxidation, and a reduction in the time required to reach the maximum rate of heat release. As previously described, the tests were carried out for the constant bulk equivalence ratio of $\phi = 0.25$, thus the injections for the $X_{O2} = 0.18$ tests carry 50 % more mass than the $X_{O2} = 0.12$ tests. The increased fuel mass leads to additional radicals that contribute to the low temperature chain branching mechanism, and hence faster ignition.

Soy Methyl Esters

All of the ignition delay measurements for the SME fuel sprays are presented in Figure 4-5, including measurements of both τ_1 and τ at the molar oxygen fractions of $X_{O2} = 0.12$ and $X_{O2} = 0.18$. For the $X_{O2} = 0.12$ tests, the first ignition delay varied between 2.3 ms $\leq \tau_1 \leq$ 11.8

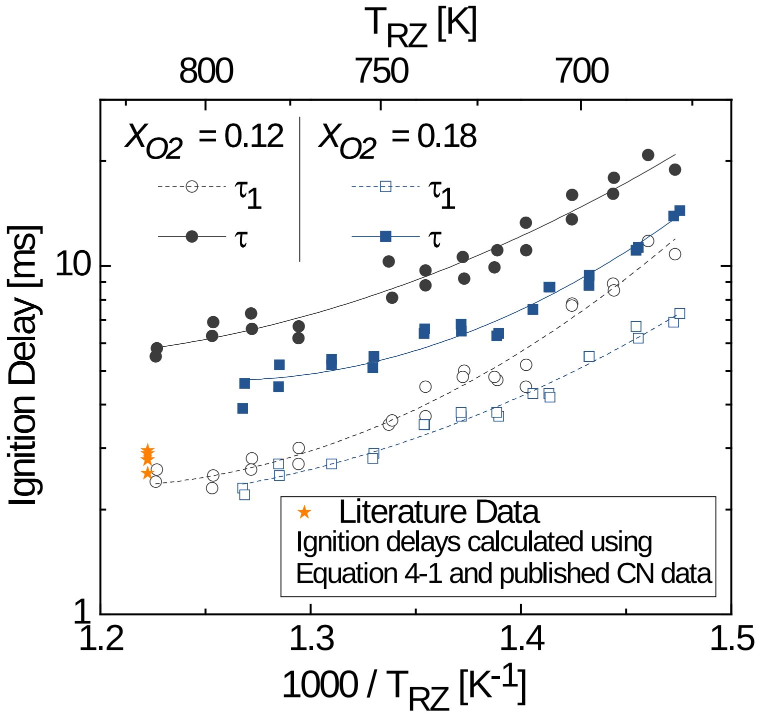

Figure 4-5. Ignition delay measurements (τ_1 and τ) for SME fuel sprays in oxidizing environments with $X_{O2} = 0.12$ and $X_{O2} = 0.18$.

ms, while the total ignition delay assumed values between 5.5 ms $\leq \tau \leq$ 20.8 ms. For the X_{O2} = 0.18 tests, first ignition delay varied between 2.2 ms $\leq \tau_1 \leq$ 7.3 ms, while the total ignition delay assumed values between 3.9 ms $\leq \tau \leq$ 14.4 ms. The potential onset of negative temperature coefficient (NTC) behavior becomes visible in the X_{O2} = 0.18 dataset near T_{RZ} = 750 K. This evidence appears as a gentle roll-off in the ignition delay data, demonstrating decreased temperature sensitivity with increasing temperature, which typically characterizes an NTC region. NTC behavior is commonly observed in gas phase ignition delay measurements, but under certain conditions, it may be expected that effects of physical transport processes such as spray vaporization would prevent its identification. Evidence to the contrary exists in the X_{O2} = 0.18 test data as well as in published petrodiesel and CME ignition delay data [149]. The appearance of NTC behavior in spray ignition delay measurement has also been noted by Kobori et al. [78] in their study regarding the ignition of petrodiesel fuel sprays. The X_{O2} = 0.12 test data does appear to be approaching NTC behavior near the upper limit of tested reaction zone temperatures, but additional tests at higher temperatures are required for confirmation. It is also observed that in the lower temperature limit, the τ_1 data diverge for the X_{O2} = 0.12 and the X_{O2} = 0.18 tests. We hypothesize this occurs due to the combination of three effects. First, as described in Table 1, all tests been conducted using a bulk equivalence ratio of ϕ = 0.25. Thus, by increasing the oxygen mole fraction by 50 % from X_{O2} = 0.12 to X_{O2} = 0.18, the injected fuel mass is similarly increased by 50 %. The increased fuel mass will lead to additional radicals that contribute to ignition mechanisms and faster reaction. The second effect that must be considered is that low temperature chain branching mechanisms rely on oxygen availability. Increasing the oxygen fraction by 50 % around the periphery of the spray is expected to augment the reactivity. Finally, by assuming these kinetic effects influence the behavior of the system, there must be sufficient time for the reactants to vaporize and mix. We previously estimated that the physical ignition delay is 2 – 3 ms, and by reviewing Figure 4-5, we see that the two datasets diverge most dramatically for $\tau_1 > 3$ ms, or $T_{RZ} < 740$ K. This may indicate that measurements with $T_{RZ} < 740$ K are kinetically-influenced, while the measurements with $T_{RZ} < 740$ K are determined primarily by physical transport processes.

Figure 4-5 also shows ignition delays that have been calculated based on published cetane number data for soybean methyl ester biodiesel [118,121,150,122]. These data points have been calculated using the expression,

$$\mathrm{DCN} = 4.46 + \frac{186.6}{\mathrm{ID}} \tag{4-8}$$

which is normally used to calculate the derived cetane number (DCN) from ignition delay (ID) data recorded in an IQT device. The CN data used for these calculations has been measured in a CFR engine rather than an IQT; however, we presume this is immaterial because CN and DCN data are highly correlated [151]. Still, some important disclaimers must accompany these calculated ignition delays. First, the analysis of the published CN data begins by assuming test conditions [53] matching those in an IQT: $T = 545\ ^{\circ}\mathrm{C}$ and $p = 21.37$ bar. We have subsequently scaled the data by a $1/p$ pressure dependence to match the 30 bar test condition used in our experiments. This pressure dependence is commonly cited in the literature, but we cannot be certain it is accurate for these tests. The second cautionary note is that cetane numbers are measured using 21 % oxygen [53], while the ignition delays reported in this work were measured with oxygen percentages of 12 % and 18 %. Finally, it should be noted that cetane number tests in a CFR engine begin by adjusting the compression ratio until an ignition delay of 13.0 ± 0.2° crank angle is obtained. For the given compression ratio, the CN is assigned by identifying the blend of *n*-cetane and heptamethylnonane which produces ignition quality matching that of the test fuel, according to the equation,

$$\mathrm{CN} = \%\ n\text{-cetane} + 0.15\ (\%\ \mathrm{HMN}). \tag{4-9}$$

In light of these considerations, the comparison in Figure 4-5 must be viewed as general check for consistency between our measurements and data published in the literature. The calculated ignition delays which are plotted in Figure 4-5 correspond to temperatures exceeding our test conditions, but suggest that our measurements are logically consistent with CN measurements for soy-based biodiesel. It may be expected that any deviation in the results is accounted for by incorrect pressure scaling and/or inconsistency in the oxygen concentrations and ignition delay definition.

Canola Butyl Esters

Figure 4-6 displays the τ_1 and τ measurements for CBE fuel sprays in oxidizing environments with X_{O2} = 0.12 and X_{O2} = 0.18. For the CBE tests using X_{O2} = 0.12, the first ignition delay and total ignition delay periods varied between 2.2 ms ≤ τ_1 ≤ 11.6 ms and 5.5 ms ≤ τ ≤ 20.8 ms, respectively. By increasing the oxygen mole fraction to X_{O2} = 0.18, the span of ignition delay times was reduced to 2.6 ms ≤ τ_1 ≤ 8.6 ms and 4.9 ms ≤ τ ≤ 15.2 ms. The X_{O2} = 0.18 CBE ignition delay data also exhibit potential NTC behavior, which begins to appear at reaction zone temperatures near T_{RZ} = 750 K. Contrary to the SME data, the X_{O2} = 0.12 dataset shows stronger evidence of NTC behavior, near T_{RZ} = 770 K. The τ_1 measurements are very similar for both of the tested oxygen concentrations for reaction zone temperatures of $T_{RZ} > 720$ K. By reconsidering the ignition delay definitions, we interpret this observation to mean that the timing of initial fuel heat release is dominated by the physical transport processes of spray breakup and evaporation, and that the oxygen availability plays a secondary role. For lower

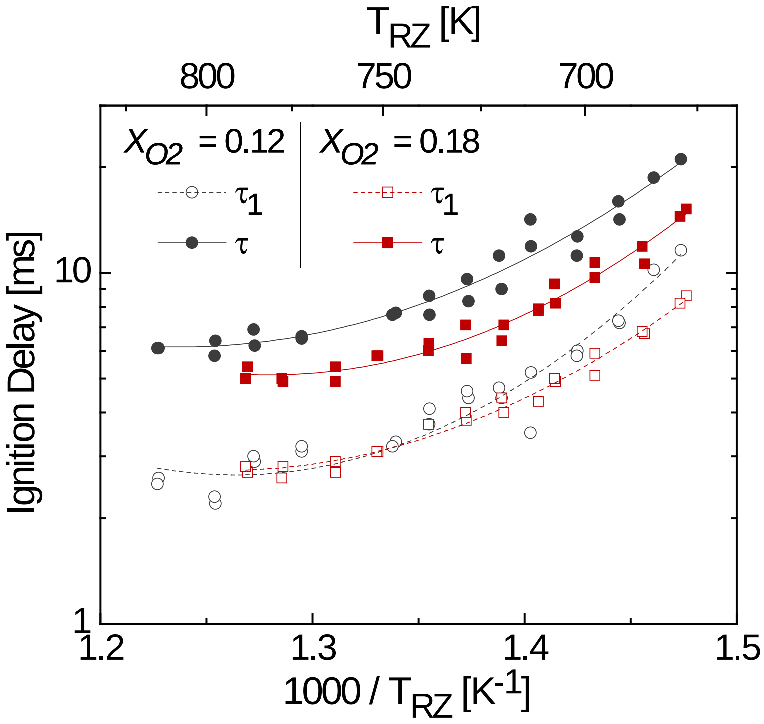

Figure 4-6. Ignition delay measurements (τ_1 and τ) for CBE fuel sprays in oxidizing environments with X_{O2} = 0.12 and X_{O2} = 0.18.

reaction zone temperature ($T_{RZ} < 720$), the two τ_1 datasets diverge, as seen for the SME tests. Our hypothesis regarding this behavior is the same for CBE as for SME. Figure 4-6 also shows the total ignition delay data for the two oxygen concentrations is easily distinguished, indicating the oxygen concentration is important in determining the time required to reach the maximum heat release rate.

Petrodiesel

A similar set of ignition delay data for D2 is presented in Figure 4-7, where τ_1 and τ measurements are presented for spray ignition tests in oxidizing environments with X_{O2} = 0.12 and X_{O2} = 0.18. For the tests using X_{O2} = 0.12, the first ignition delay period varied between 2.8 ms ≤ τ_1 ≤ 12.0 ms, while the total ignition delay varied between 7.7 ms ≤ τ ≤ 24.6 ms. For the tests using X_{O2} = 0.18, the first ignition delay period varied between 2.4 ms ≤ τ_1 ≤ 11.8 ms, while the total ignition delay varied between 5.9 ms ≤ τ ≤ 25.9 ms. The overall trends are quite

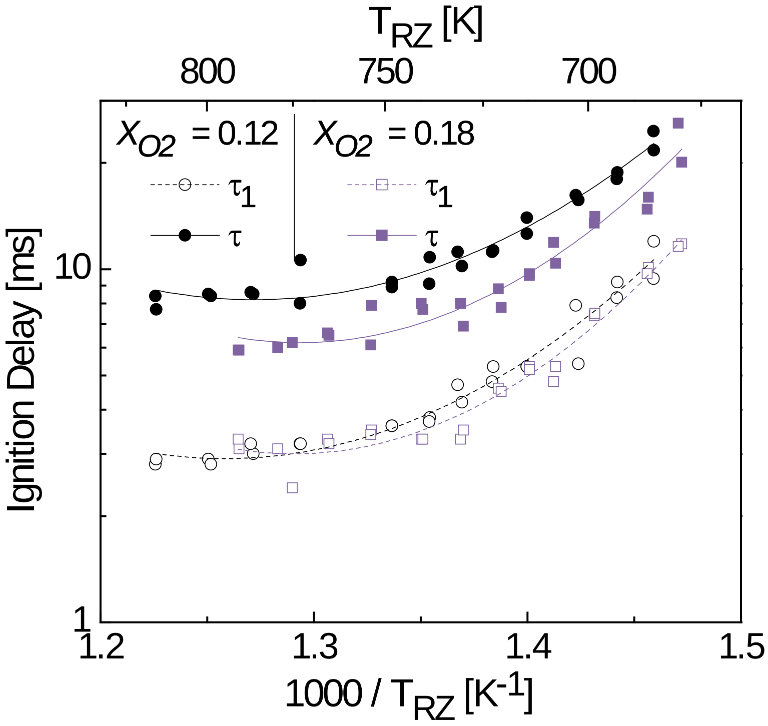

Figure 4-7. Ignition delay measurements (τ_1 and τ) for D2 fuel sprays in oxidizing environments with X_{O2} = 0.12 and X_{O2} = 0.18.

similar to those observed for the BD ignition delays, with evidence of NTC behavior becoming visible near T_{RZ} = 740 K where the ignition delays become less sensitive to increases in temperature. This corresponds very well with the published data of Kobori et al. [78] which indicates the onset of NTC behavior in diesel spray ignition between 730 – 745 K. As with the BD results, the τ_1 measurements for D2 sprays show little sensitivity to the oxygen and fuel concentration change, while a marked reduction in τ is observed as the oxygen mole fraction increases from X_{O2} = 0.12 to X_{O2} = 0.18. The increase in oxygen mole fraction also leads to increased fuel mass concentration because all tests use ϕ = 0.25. As with our discussion of the τ_1 data for the CME tests, we would expect fuel kinetics to play an increasingly important role for longer delays. For τ_1 measurements longer than 3 ms, data from the X_{O2} = 0.18 dataset appear to be longer than for the X_{O2} = 0.12 data, but we are cautions to draw this conclusion given the precision of the data.

Comparison of Canola Methyl Esters and Petrodiesel

The data from Figures 4-4 and 4-7 are plotted again in Figures 4-8 and 4-9 to allow a direct comparison of the CME and D2 ignition delays using the same carbon concentrations for each fuel. Figure 4-8 shows that although the first ignition delay period for CME is shorter than for D2 over the range of tested reaction zone temperatures, the difference between the two fuels is quite small. In fact, over the full range of tested reaction zone temperatures, non-linear least squares fits were used to calculate that on average, the τ_1 ignition delay measurements for CME are only 0.6 ms (-12 %) and 0.8 ms (-16 %) shorter at X_{O2} = 0.12 and X_{O2} = 0.18, respectively.

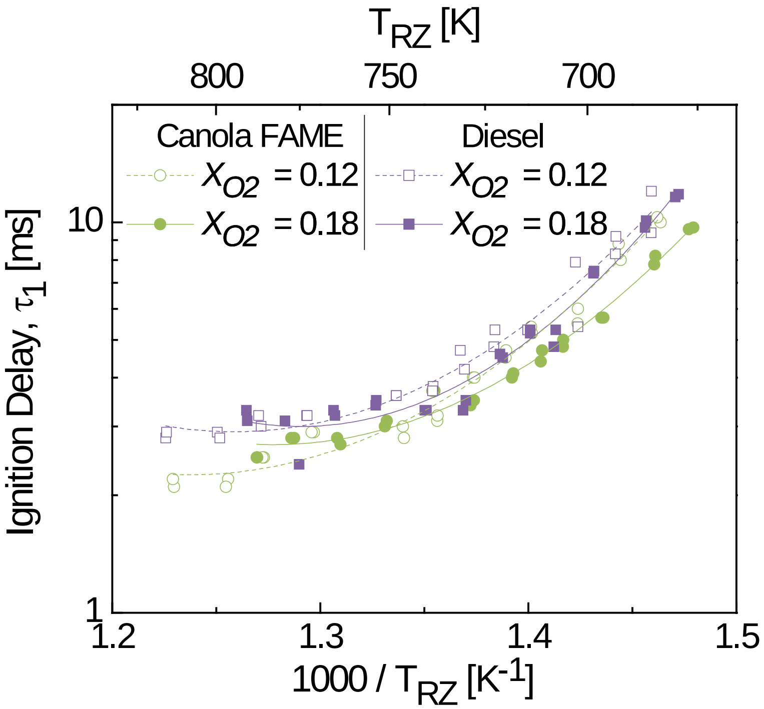

Figure 4-8. Comparison of ignition delay period τ_1 for CME and D2 fuel sprays in oxidizing environments with X_{O2} = 0.12 and X_{O2} = 0.18.

Given the uncertainty of the measurements, these are effectively the same. We do note that a longer physical delay is expected for CME relative to D2 based on the physical properties of the two fuels (*i.e.*, higher viscosity and surface tension for BD relative to D2). If the τ_1 measurements are in fact shorter for CME than D2, we expect this indicates that kinetics plays an important role in determining τ_1. For the τ measurements, the disparity between the two fuels grows, and the CME measurements are shorter than the D2 measurements by 3.0 ms (-23 %) and 2.3 ms (-23 %) at X_{O2} = 0.12 and X_{O2} = 0.18, respectively. A longer total ignition delay period for D2 is consistent with our expectations based on reported cetane number for the fuels. A typical D2 cetane number is 47 [127], while canola CME cetane numbers have been reported between 47.9 and 56 [118-120]. The direct comparison of the two fuels also illustrates that evidence of potential NTC behavior occurs for the D2 spray ignition measurements at lower reaction zone temperatures than for the CME. Furthermore, the data suggests that the NTC region may be more pronounced for D2 than for CME. The kinetics that would lead to NTC behavior are known to strongly depend on the competition between decomposition reactions of the alkyl hydroperoxy radical and the oxygen addition reaction that leads to low temperature chain branching reactions [152]. The competition between these reaction pathways depends on fuel structure such as molecular unsaturation and branching in the alkyl chain. For example, unsaturation in ester compounds like the biodiesel components is known to decrease low temperature reactivity [153]. We expect these influences to affect the observed onset of NTC-like behavior, but among the complicated blend of fuel species and transport processes, we present these only as considerations when interpreting the data.

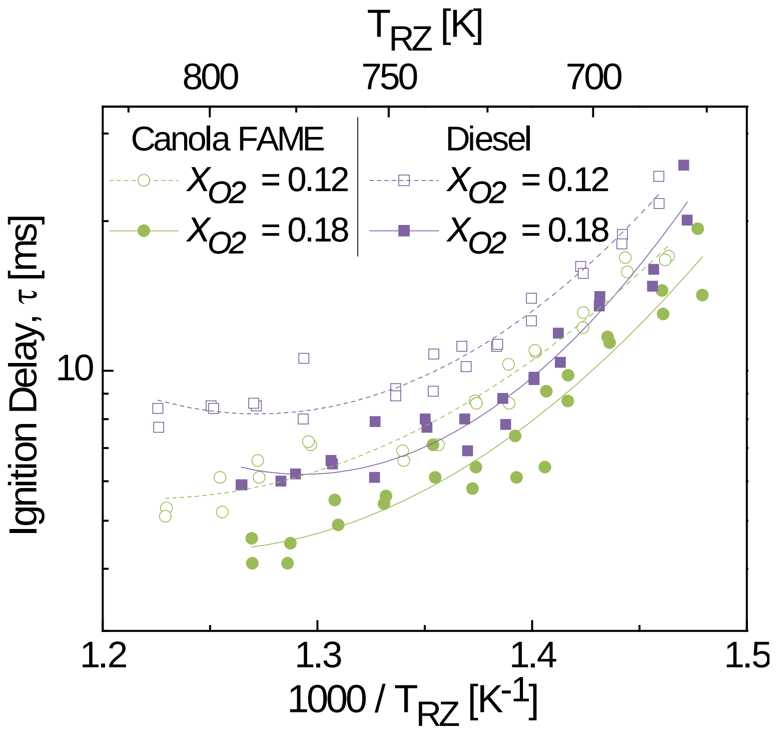

Figure 4-9. Comparison of ignition delay period τ for canola BD and D2 fuel sprays in oxidizing environments with X_{O2} = 0.12 and X_{O2} = 0.18.

4.5.3. Effect of Fatty-Ester Composition on BD Ignition Delays

The ignition delay measurements taken using X_{O2} = 0.18 appear in Figure 4-10 for SME, CME, and CBE fuel sprays. At each tested reaction zone temperature, variation can be seen between the τ_1 and τ measurements for the tested fuels; however, when considering the overall behavior, the fuels are effectively indistinguishable. These data imply that with sufficient oxygen availability, small changes in alkyl chain unsaturation and alkoxy chain length do little to alter the ignition characteristics of a biodiesel fuel spray. This finding is not unlike what is observed in biodiesel combustion pressure traces of rapeseed FAMEs (RME) and tallow FAMEs (TME), published by Schönborn et al. [94]. Over 70 % of both RME and TME are composed of esters of C_{18} fatty acids. However, of the samples investigated by Schönborn et al., the RME contained

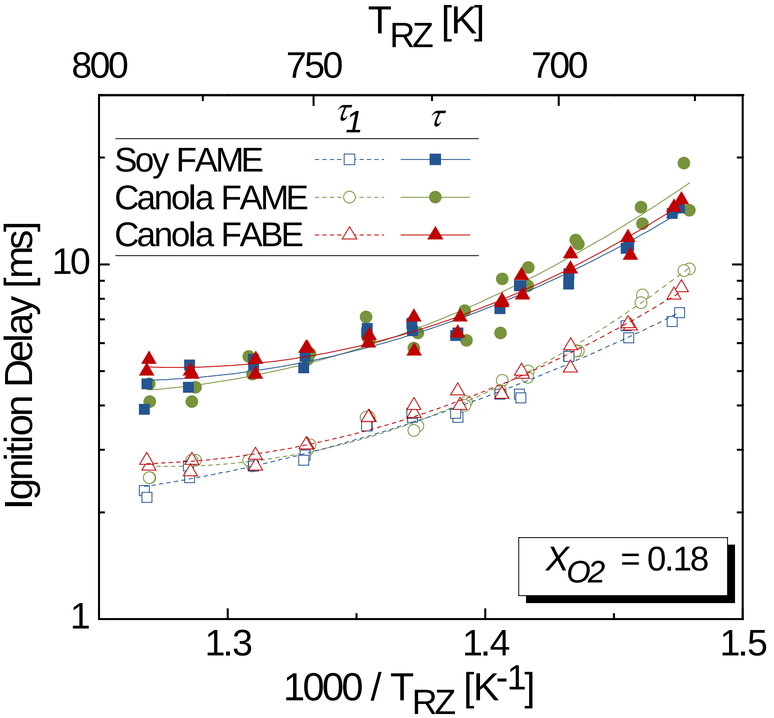

Figure 4-10. Ignition delay measurements (τ_1 and τ) for SME, CME and CBE fuel sprays in an oxidizing environment with X_{O2} = 0.18.

61 % of the monounsaturated C_{18} fatty ester, methyl oleate, while the TME contained only 44 % methyl oleate. These compositional changes did little to distinguish the ignition characteristics of the two fuels. Furthermore, the CN data listed in Table 4-1, which are measured using 21 % oxygen in the inlet air, indicate that canola FAMEs and soy FAMEs are virtually identical.

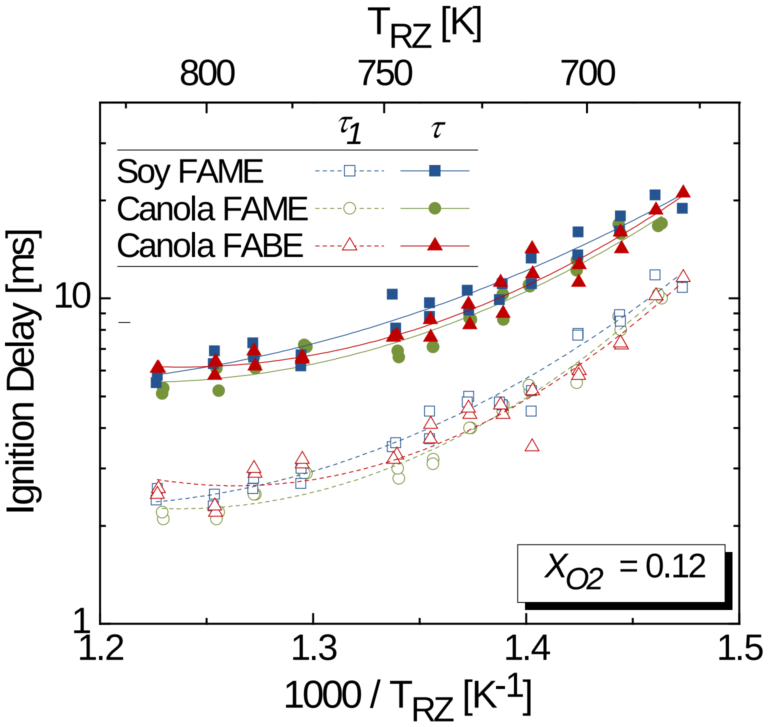

Figure 4-11. Ignition delay measurements (τ_1 and τ) for SME, CME and CBE fuel sprays in an oxidizing environment with X_{O2} = 0.12.

By decreasing the oxygen availability to 12 %, some variation in the ignition delays between the biodiesel fuels is observed, as illustrated in Figure 4-11. By comparing the CME and CBE data, we see little variation in both τ_1 and τ. This is not entirely unexpected because as noted previously, other studies have failed to establish a conclusive trend in reactivity change as a function of alkoxy chain length. For low-temperature autoignition measurements taken in the gas phase, we would expect the butyl esters to ignite more readily than the methyl esters because increasing the carbon chain length tends to enhance low temperature chain branching [154]. For a spray ignition measurement, however, where physical transport processes are linked with chemical events, this does not appear to be the case. For changes in molecular unsaturation, represented by a comparison of the SME and CME data, we do observe a change in both the τ_I and τ measurements. The variation in the ignition delays between the SME and CME datasets is not dramatic, but we believe the disparity in the data to be meaningful, especially considering the similarity in the data measured for X_{O2} = 0.18. For additional confirmation, the ignition delays measured at each reaction zone temperature were averaged for the unique fuels and compared.

For these calculations, the τ measurements for CME were shorter than for SME at all points except one ($T_{RZ} \approx$ 772 K). This is in contrast to the X_{O2} = 0.18 dataset where 75 % of the τ measurements for SME were shorter than for CME. The observed reduction in ignition delay of the CME fuel sprays relative to the SME fuel sprays may be expected, because of the two fuels, SME has more molecular unsaturation which tends to decrease cetane number. The ability to observe altered ignition behavior for changes in molecular unsaturation, but not for changes in alkoxy chain length corroborate the findings of Knothe [105], which indicated that unsaturation in the fatty acid chain had the strongest influence on cetane number.

Collectively, the data at X_{O2} = 0.18 indicate that modest variations in the fatty acid composition do not significantly affect the spray ignition characteristics of a biodiesel fuel under low temperature and moderate oxygen concentrations, but that the ignition characteristics of the fuels can be distinguished as oxygen concentrations are decreased. This type of effect may have practical consequences for advanced diesel engines operating with heavy exhaust gas recirculation. As more biodiesel is introduced to the market with modified fatty ester composition for improved fuel properties, engine control schemes should consider the variation in ignition and combustion properties of the fuels.

4.5.4. Effect of Reaction Zone Temperature on the Maximum Normalized AHRR of BD and D2

Comparison of Biodiesels

The maximum AHRR ($\dot{Q}_{c,m}$) has been determined for each test using the heat loss model described in this chapter. This data is presented in its original form in Figure 4-12, and in modified form in Figure 4-13 where the data has been normalized by the total ignition delay time

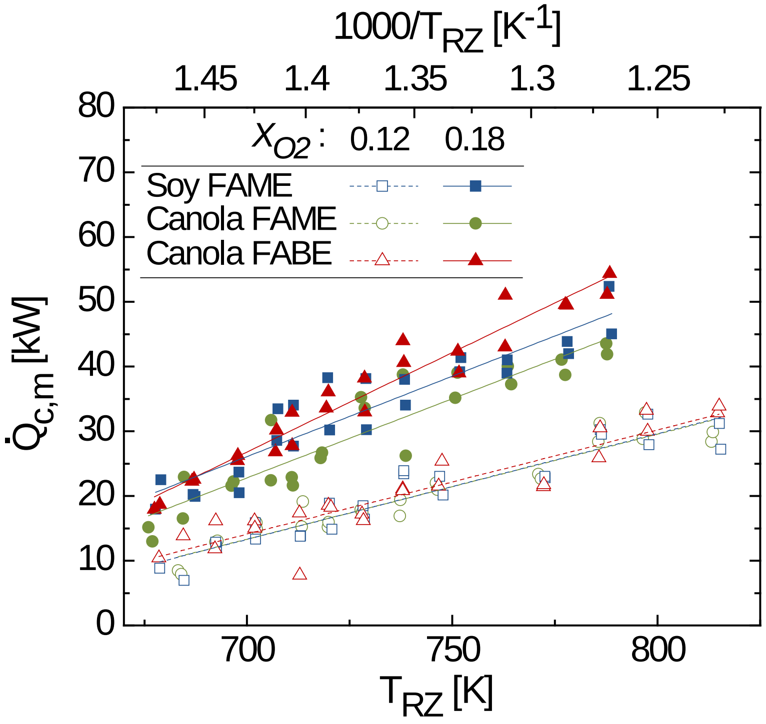

Figure 4-12. Comparison of maximum AHRR values ($\dot{Q}_{c,m}$) for SME, CME and CBE fuel sprays in oxidizing environments with X_{O2} = 0.12 and X_{O2} = 0.18.

and on an input energy basis (*i.e.*, $\frac{\dot{Q}_{c,m}}{\tau \cdot m_f \cdot \Delta H_c} = \hat{\dot{Q}}_{c,m}$). The input energy is calculated by multiplying the injected fuel mass (m_f) by the lower heating value of the fuel (ΔH_c). Normalization by the total ignition delay time and on an input energy basis provides a comparison between the maximum AHRR of the fuels which is isolated from the influences of premixing time and available chemical energy in the fuel.

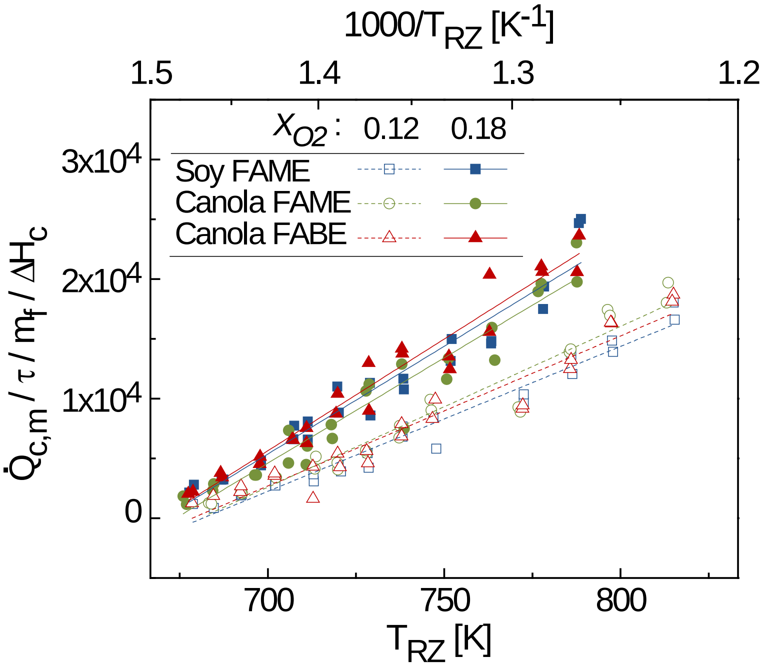

Figure 4-13. Comparison of maximum AHRR values normalized by total ignition delay and by input energy ($\frac{\dot{Q}_{c,m}}{\tau \cdot m_f \cdot \Delta H_c}$) for SME, CME and CBE fuel sprays in oxidizing environments with X_{O2} = 0.12 and X_{O2} = 0.18.

The data in Figure 4-12 shows that for changes in reaction zone temperature, $\dot{Q}_{c,m}$ varies approximately linearly for all fuels at both the X_{O2} = 0.12 and the X_{O2} = 0.18 test conditions. The linear trendlines applied to the test cases vary substantially for all fuels between the two tested oxygen concentrations. The steeper trendline slopes for the X_{O2} = 0.18 tests relative to the

X_{O2} = 0.12 tests indicate that the sensitivity of $\dot{Q}_{c,m}$ to the reaction zone temperature increases with oxygen concentration. We suspect this is a transport effect because as temperature increases, fuel in the reaction zone is more readily volatilized and mixed with the oxidizer gases. This increases the premixed volume prior to ignition and leads to higher $\dot{Q}_{c,m}$ values during combustion. In the lower limit of tested reaction zone temperatures, the X_{O2} = 0.12 and the X_{O2} = 0.18 tests are seen to converge. Based upon our stated hypothesis regarding the variation in sensitivity to T_{RZ} changes, we believe this occurs because volatilization is not fast enough at the lower temperatures to provide an adequate premixing time for augmentation of $\dot{Q}_{c,m}$ by the increased oxygen concentrations.

The data in Figure 4-12 illustrates that the maximum AHRR of the tested biodiesels is not the same for the X_{O2} = 0.18 tests, especially for increasing reaction zone temperatures (T_{RZ} > 750 K) where the CBE exhibits larger $\dot{Q}_{c,m}$ values than the CME and SME tests. However, this data does not consider variation in time available for premixing that arises from differences in ignition delay times among the fuels. Nor does this data consider small differences in input energy that arise from unique heating values for each fuel. Figure 4-13 compares data from the same tests where the maximum AHRR has been normalized by the total ignition delay time and by the input fuel energy. Compared to the data in Figure 4-12, the $\hat{\dot{Q}}_{c,m}$ data for the different biodiesels at X_{O2} = 0.18 are seen to approach one another. The trendlines do not overlap perfectly, but considering the scatter in the experimental data, they cannot be used to distinguish between the fuels. The data in Figures 4-12 and 4-13 collectively indicate that differences in the maximum AHRR between the biodiesels arise from the unique premixing times and heating values of the fuels.

Comparison of D2 and CME

The maximum normalized AHRR for the CME and D2 test cases appear in Figure 4-14 for both X_{O2} = 0.12 to X_{O2} = 0.18. For the X_{O2} = 0.12 tests, the $\hat{\dot{Q}}_{c,m}$ data for CME and D2 data are very similar at all reaction zone temperatures. This result suggests that the rate of reaction for the X_{O2} = 0.12 tests is limited by the low oxygen concentrations in the reaction zone. A diesel fuel blend contains some components which are more volatile than the methyl esters that comprise biodiesel. At a given temperature, these D2 fuel components are more readily volatilized which should lead to a larger premixed volume relative to the CME tests. Based on this description, we would expect the $\hat{\dot{Q}}_{c,m}$ values for D2 to be larger than for CME; however, this is not the case for these low oxygen concentrations. We suspect this occurs because there is insufficient oxygen to react with all of the fuel in the reaction zone. Although the D2 fuel volatilizes more quickly than CME, and thus begins mixing with oxidizer gases at an earlier stage, a portion of this fuel remains unreacted and does not appear to contribute to increasing $\hat{\dot{Q}}_{c,m}$. A comparison of the $\hat{\dot{Q}}_{c,m}$ data for the X_{O2} = 0.18 tests in Figure 4-14 clearly demonstrates that the D2 exhibits greater maximum normalized AHRR than CME at increased temperatures. The $\hat{\dot{Q}}_{c,m}$ data for D2 and CME are similar for reaction zone temperatures near 700 K, but diverge for temperatures increases beyond this point with the maximum normalized AHRR of both fuels demonstrating an exponential dependence on reaction zone temperature. Application of our hypothesis regarding the X_{O2} = 0.12 results to these data implies that the increased oxygen concentration in the X_{O2} = 0.18 tests provides sufficient oxygen to react with more of the volatilized D2 fuel than the tests using X_{O2} = 0.12. Based on this hypothesis, we may expect an additional gain in $\hat{\dot{Q}}_{c,m}$ by further increasing the oxygen concentration.

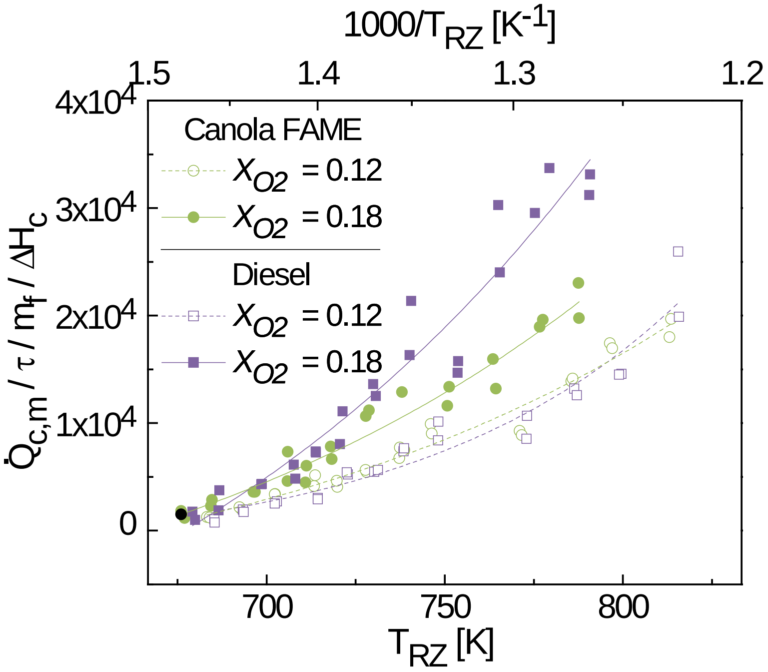

Figure 4-14. Comparison of maximum AHRR data normalized by total ignition delay time for canola BD and D2 fuel sprays in oxidizing environments with X_{O2} = 0.12 and X_{O2} = 0.18.

4.6. Conclusion

A rapid compression machine has been used to investigate the autoignition delay times and maximum AHRR of D2, CME, SME, and CBE fuel sprays under test conditions that are relevant to the LTC regime in diesel engine combustion. Comparison of the ignition characteristics of CME, SME, and CBE formed the basis for investigating the influence of fatty ester composition on biodiesel ignition and combustion behavior. Specifically, the influence of increasing the alkoxy chain length from a methyl group to a butyl group has been tested with canola-based fatty esters. Additionally, the influence of varying amounts of molecular unsaturation has been tested by comparing the ignition behavior of soy-based methyl esters and canola-based methyl esters. The ignition delay and AHRR measurements have been taken at various oxygen mole fractions (X_{O2} = 0.12 and X_{O2} = 0.18), and various reaction zone temperatures (676 K $\leq T_{RZ} \leq$ 816 K) which were investigated by altering the diluent composition and the post-compression cooling time. The viability of this test approach has been examined, and tests show that for post-compression cooling times between 11.9 ms and 150.8 ms, the first and total ignition delay periods are repeatable to within 8 % and 7 %, respectively.

Test temperatures in the reaction zone have been numerically calculated using the adiabatic mixing assumption proposed by El-Wakil et al. [129] This approach accounts for temperature reductions in the reaction zone which occur as energy is transferred from the hot gas to the cooler fuel droplets for warming and vaporization. A single-zone heat loss model has been developed which calculates convective heat losses using a modification to the approach described by Hohenberg. [144] The calculated heat loss profiles have been used as the basis for calculating two ignition delay periods.

The total ignition delay measurements for D2 are compared with values reported in literature. The measurements we report are not at identical test conditions to those in literature, but when scaled, our data exhibits logical consistency with literature data. A comparison with other diesel spray ignition studies indicates that the orifice size of the injector and the injection pressure may strongly influence the total ignition delay of D2. The ignition delay data for D2 and CME exhibit potential evidence of NTC behavior near the upper limit of the tested temperatures for both oxygen mole fractions tested. This is observed through decreased ignition delay sensitivity to changes in temperature. The reduction in temperature sensitivity occurs near T_{RZ} = 740 K for the D2 measurements which is consistent with literature data. For CME, the decreased temperature sensitivity becomes evident at a higher reaction zone temperature of T_{RZ} = 770 K. At similar test conditions, the total ignition delay period of CME was on average 23 % shorter than for D2 at oxygen mole fractions of X_{O2} = 0.12 and X_{O2} = 0.18, respectively. Although the first ignition delay period was shorter for CME than for D2, the average results differed by less than 1 ms. Increases in the oxygen mole fraction at a given reaction zone temperature led to a reduction in the total ignition delay for both CME and D2, but had little to no influence on the first ignition delay period. The onset of potential NTC behavior is visible for both SME and CBE, approaching the upper limit of tested reaction zone temperatures. However, there is no conclusive evidence for this behavior for the SME tests using X_{O2} = 0.12. The SME ignition delay measurements show logical consistency with ignition delays that have been calculated using published cetane number data and a correlation developed to relate ignition delays with derived cetane numbers from an Ignition Quality Tester device.

A comparison of the ignition delays of the various biodiesels indicates that increasing the alkoxy chain length from a methyl group to a butyl group has little to no effect on the ignition delay of the fuel. This is observed at both of the tested oxygen concentrations and throughout the range of tested reaction zone temperatures. However, a comparison of SME and CME fuel sprays shows that the increased polyunsaturation of the SME tends to increase the ignition delay relative to CME. This effect was visible for the tests at X_{O2} = 0.12, but could not be observed for the X_{O2} = 0.18 tests where we presume that the influence of oxygen availability on the total ignition delay plays a secondary role to the more pronounced physical ignition delay.

Calculation of the maximum AHRR for the biodiesels illustrates an approximately linear dependence on the reaction zone temperature. For the X_{O2} = 0.18 tests, the CBE tests exhibit the largest maximum AHRR of the fuels, especially approaching the upper limit of reaction zone temperatures (T_{RZ} > 750 K). Normalization of the data by the ignition delay times and input fuel energy indicates that variation in the maximum AHRR among the fuels is primarily due to differences in fuel heating values and to premixing times that arise from non-uniform ignition delays between the fuels.

The maximum normalized AHRR data for the CME and D2 fuels were compared over the full range of reaction zone temperatures, with the data exhibiting an approximately linear dependence on the reaction zone temperature at both oxygen fractions (12 % and 18 %). The results appear to be largely influenced by the amount of oxygen available in the reaction zone to react with volatilized fuel. We expect the increased volatility of D2 to enhance the extent of the premixture relative to CME, and thus lead to larger maximum normalized AHRR values. However, this is only conclusively observed for the X_{O2} = 0.18 tests where sufficient oxygen exists to react with more of the volatilized D2 fuel.

Increases in the reaction zone temperature led to modest increases in maximum AHRR for CME, but a more pronounced increase in the AHRR was observed for D2 over the same set of reaction zone temperatures. We hypothesize that the greater temperature sensitivity of the D2 maximum AHRR occurs because the more volatile components of the D2 readily enter the vapor phase at higher temperatures and increase the extent of the premixture prior to ignition. The maximum AHRR is augmented for both CME and D2 as the oxygen mole fraction increases; however, the D2 maximum AHRR is greatly enhanced for the X_{O2} = 0.18 tests at higher temperatures where the volatilized D2 components burn more rapidly with the more plentiful oxygen.

The results presented here form a basis for comparing the spray ignition properties of two fuels under practical engine conditions where the chemical ignition process is tightly coupled to the physical transport processes such as spray breakup and evaporation. The data demonstrate the ability to differentiate between the spray ignition properties of different fuels and to potentially identify subtle ignition features such as NTC behavior. Future studies will be devoted to investigating the spray ignition characteristics of fuels with changes in molecular structure, to identify molecular features which lead to significant changes in the total physical and chemical ignition delays of a fuel.

Chapter 5:

ENERGETIC ENHANCEMENT OF LIQUID AEROSOL FUELS

5.1. Introduction

The next generation of advanced propulsion systems will strive to combine dramatically enhanced power output with high efficiency and control; pushing combustion to occur at the very limits of flammability and stability for a specific fuel. To address the potential challenges ahead in terms of achieving combustion stability, advanced technologies for active combustion enhancement such as high-energy laser spark ignition [155], turbulent jet ignition [156], and plasma jet ignition [157] are being investigated for a range of novel concept engines. The problem is further compounded by the introduction of new and alternative fuel blends which can exhibit drastic variation in combustion characteristics depending on the operational conditions. The HRJ fuels investigated in Chapter 3 exhibit reduced volumetric energy density relative to conventional fuels, which leads to range and payload limitations for aircraft operating on the fuels. A new strategy to address this issue is to change the reactivity and the energetic output of the fuel itself by adding highly exothermic, energetic nanoparticles to the liquid fuel.

Energetic nanoparticles are nano-sized (10−100 nm range) particles, usually metallic with a passivated oxide layer, and are characterized by a high rate of energy release [158]. Energetic nanoparticles offer a high volumetric heat of oxidation, enabling transportation of more energy per given fuel volume. When mixed in a fuel or a composite, they generally exhibit faster ignition timescales due to the dramatic increase in the surface-to-volume ratio [159], and can ignite below the bulk melting point of the metal due to rapid temperature gradients through their thin oxide layers [160]. Nano-sized energetic particles offer the potential of controlled reactivity of the fuel, increased combustion efficiencies, and increased safety in handling.

The purpose of this study is to develop an aerosol rapid compression machine, a flexible experimental platform to investigate the ignition characteristics of liquid fuels where energetic nanoparticles are suspended by surfactants. Charging the RCM with an aerosol instead of vaporized fuel is important as the embedded nanoparticles must also be carried into the combustion chamber and cannot undergo vaporization. The new testbed is designed for combustion at practical high-pressure conditions and provides optical access for laser and optical diagnostics to be added in the future. As a proof-of-concept demonstration of the aerosol RCM's functionality, energetic-nanoparticle-enhanced combustion of ethanol and JP-8 will be presented.

5.2. Target Fuels for Demonstration

The target fuels used in the demonstrations are ethanol and JP-8 with 50 nm average particle size (APS) aluminum nanoparticles. Ethanol was chosen primarily because the combustion characteristics are well-defined and a detailed chemical kinetic mechanism [161] is available. Also, ethanol is an easy fuel to handle and adequate for initial testing of the aerosol RCM. Therefore, most of the characterization of the aerosol RCM was conducted using ethanol.

Aluminum nanoparticles were selected because they have a high heat of oxidation and have received much attention in the literature [162-163]. Compared to the ignition temperatures of micron-sized particles (1300−2100 K) [164-165], aluminum nanoparticles have shown ignition well below the bulk melting temperature [165] and as low as 800 K [166], enhancing the burning rate of propellants by 10 to 20 times over conventional bulk aluminum particles [159].

Their ignition profiles are generally very rapid and recently have shown potential as additives for liquid fuels [167-168]. For this study, we are using 50 nm Alex® particles from Argonide Corporation, which are suspended in both ethanol and JP-8.

To extend the demonstration of the aerosol RCM to practical fuels, measurements of energetic-nanoparticle-enhanced ignition are also shown using JP-8, the most widely used jet fuel for the Air Force and the candidate for the 'single fuel forward' policy of the Army. A number of studies have looked into the thermal oxidation chemistry of JP-8 including ignition delay measurements in shock tubes and RCM [169-170,33], chemical kinetics and emission studies in experimental burners [171], and numerical modeling of both reduced and detailed chemical kinetic mechanisms for surrogate blends of JP-8 [52,46]. These studies have found large variations in the ignition properties of JP-8 as a function of initial conditions which can be problematic for design of novel propulsion systems, and where nanoparticles can be of benefit by tuning the reactivity.

5.3. Temperature Analysis

Calculation of the compressed temperature for an aerosol charge is complicated due to heat and mass transfer between the gas mixture and vaporizing aerosols. Although heat loss to the reaction chamber walls can be modeled through the effective volume approach commonly used in RCM studies [1,16], the volumetric heat transfer to the droplets that occurs during compression cannot be accurately characterized without the knowledge of aerosol vaporization history (*e.g.*, measured by optical diagnostics). As a first step, here we calculate the compressed gas temperature under two limiting conditions. The upper bound of compressed temperature assumes no aerosol evaporation ('frozen aerosol'), while the lower bound of compressed temperature is calculated assuming complete evaporation before the onset of compression. Both limiting calculations proceed through the direct application of the effective volume approach, which assumes the existence of an adiabatically-compressed core of gases whose temperature is calculated using Equation 3-3. The actual value of T_C is expected to be bounded by the two limiting values, and would be closer to the lower bound value for highly volatile fuels. In the following, the T_C estimates presented are averages of the upper and lower bounds, and the uncertainties for these calculations approach ±40 K. Although the presence of the aerosol prevents formation of an adiabatic core for which Equation 3-3 is intended, our approach provides an approximate T_C that is useful for understanding the temperature regime of nanoparticle-enhancement presented in this paper. Future studies will be devoted to the application of laser and optical diagnostics for improving the accuracy of these estimates.

5.4. Test Mixture Preparation

Tests investigating the influence of nanoparticles on the ignition of liquid fuel droplets used 50 nm APS aluminum nanoparticles from Argonide Corporation. All nanoparticle-enhanced tests used 2 %-wt nano-aluminum in the respective liquid fuel where it was suspended by adding 0.03 %-wt alizarin and 0.004 %-volume triethanolamine before placing the solution in an ultrasonic bath for 120 minutes.

5.5. Experimental Results

5.5.1. Experimental Repeatability

Pressure measurements were taken during the ignition of neat ethanol aerosols to test the experimental repeatability of the RCM data. The measurements were taken using a Kistler 6125B pressure transducer, and the data were used to calculate the ignition delay (τ), which we define as the time interval between the end of compression (TDC) and the time at which the maximum rate of pressure rise due to ignition occurs [$(dP/dt)_{max}$]. TDC is identified as the time at which dP/dt becomes negative. This definition is consistent with that of the total ignition delay defined in § 3.5.2.

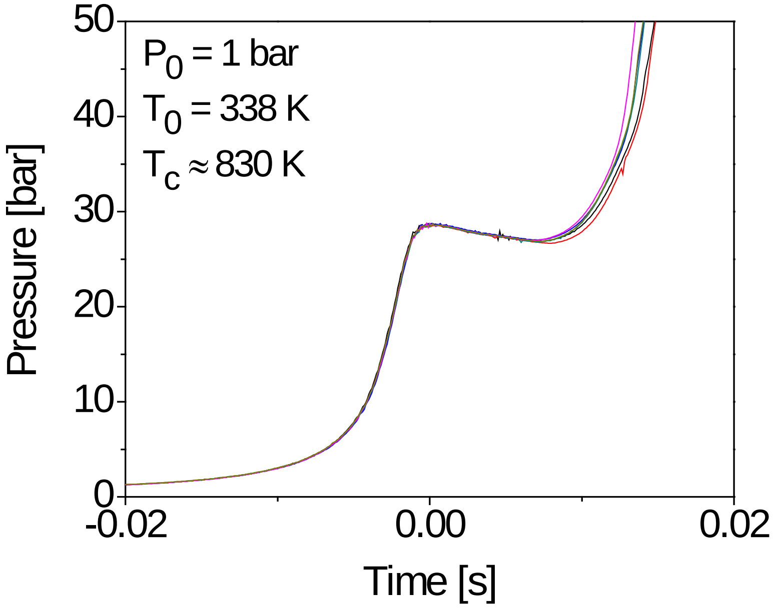

Figure 5-1. Demonstration of the experimental repeatability of autoignition of an ethanol aerosol charge at P_c = 28 bar, $T_c \approx$ 830. Molar composition (aerosol test): $C_2H_5OH/O_2/N_2$ = 1.0/6.0/22.6. Initial conditions: P_0 = 1 bar, T_0 = 338 K.

The operation protocol described in the previous section was used to investigate the experimental repeatability of ignition delays for a neat ethanol aerosol charge. Ignition tests were conducted under identical conditions (initial wall temperature: T_0 = 338 K; initial pressure: p_0 = 1 bar; compressed temperature: $T_c \approx$ 830 K; compressed pressure: p_c = 28 bar) with a molar composition of 1.0 C_2H_5OH + 6.0 O_2 + 22.6 N_2, and the results shown in Figure 5-1. support the repeatability of test data in the aerosol RCM. The figure shows six pressure traces that overlap identically during compression, and follow nearly the same profile during ignition. For the pressure traces shown in Figure 5-1, the ignition delay is repeatable to within ±10 %.

5.5.2. Ignition Enhancement with Low-Concentrations of Nanoparticles

Ignition delay measurements were taken for neat ethanol and compared with ethanol seeded with 2 %-wt aluminum nanoparticles to investigate energetic-nanoparticle-enhanced combustion of our model system. A TEM image of the aluminum nanoparticles appears in the inset of Figure 5-2. The TEM image shows the polydisperse nature of the nanoparticle size, and confirms the 50 nm APS technical specification of the nanoparticles. As a baseline for comparison, Figure 5-2 shows the same neat ethanol pressure traces displayed in Figure 5-1 from

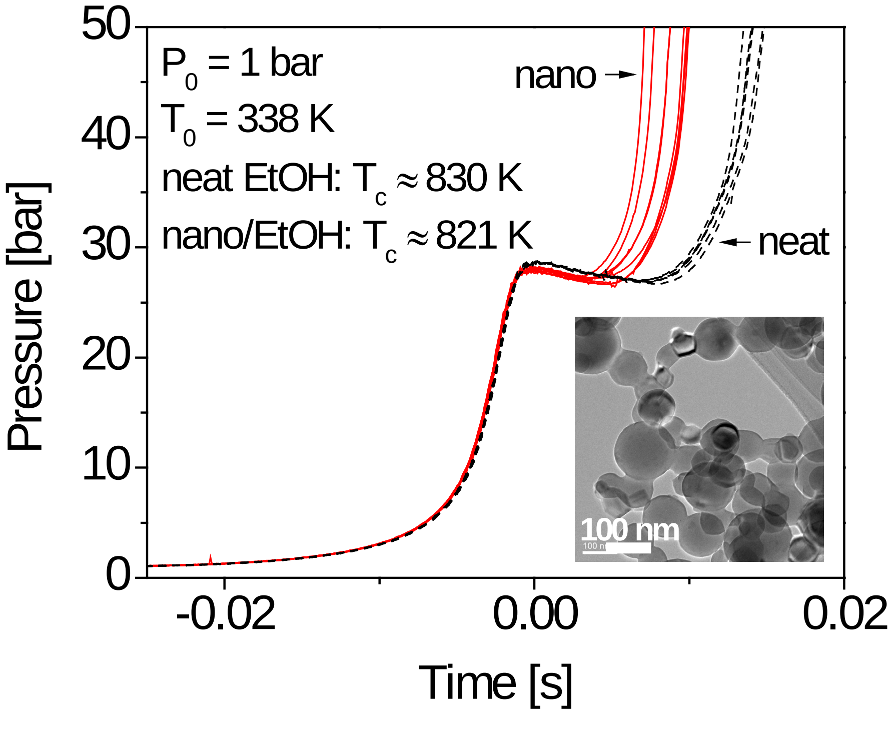

Figure 5-2. Reactive pressure traces for neat ethanol (dashed lines) and for 2 %-wt nanoparticle-enhanced ethanol (solid lines). Inset displays TEM image of 50 nm APS aluminum nanoparticles. Molar composition for neat and nano-enhanced tests (aerosol + gas): $C_2H_5OH/O_2/N_2$ = 1.0/6.0/22.6.

the repeatability experiment. Figure 5-2 also shows five pressure traces obtained for energetic-nanoparticle-enhanced ethanol combustion. It is evident from the pressure traces that the presence of the energetic nanoparticles leads to a significant reduction in the ignition delay time of ethanol. For the conditions tested (p_C = 28 bar, $T_C \approx$ 820 K), the nanoparticles led to an average ignition delay reduction of 32 % (4.6 ms) as compared to neat ethanol ignition delay times, and the results were reproducible to within ±20 %. We emphasize that all of the neat ethanol and nanoparticle-seeded ethanol tests were conducted with identical initial and operating conditions. Thus, in spite of the uncertainty in the T_C calculations our observation of a reduced ignition delay under these conditions supports the enhancement effect of the nanoparticles.

The energetic enhancement requires a lower concentration (2 %-wt) than previously reported results for nanoparticle-enhanced liquid fuels which have used concentrations of $\geq$ 5 %-wt nano-aluminum in *n*-dodecane to achieve ignition delay reductions of 40 – 75 % in a shock tube at reflected temperatures of 1175 – 1249 K [167]. The results demonstrate the ability to energetically-enhance combustion through low concentrations of nanoparticles. The mechanism whereby aluminum nanoparticles reduce the ignition delay is not evident from this study, however, we hypothesize the ignition delay reduction is a result of an increased droplet thermal conductivity that has been observed in liquids seeded with nanoparticles (nanofluids) as compared to the thermal conductivity of the neat liquid [172]. We hypothesize that by adding aluminum nanoparticles to our liquid fuel, the thermal conductivity of the droplets increases which leads to more rapid internal heating and evaporation of the aerosol droplets, and thereby the earlier onset of fuel vapor ignition. Once the nanoparticle-carrying aerosol droplets evaporate, the nanoparticles are exposed to a hot, oxidizing environment, and the nanoparticles may ignite in advance of the fuel vapors, providing another route to a shorter ignition delay. Aluminum nanoparticles have been shown to ignite at temperatures as low as ~800 K [166], which are attained in our RCM experiments.

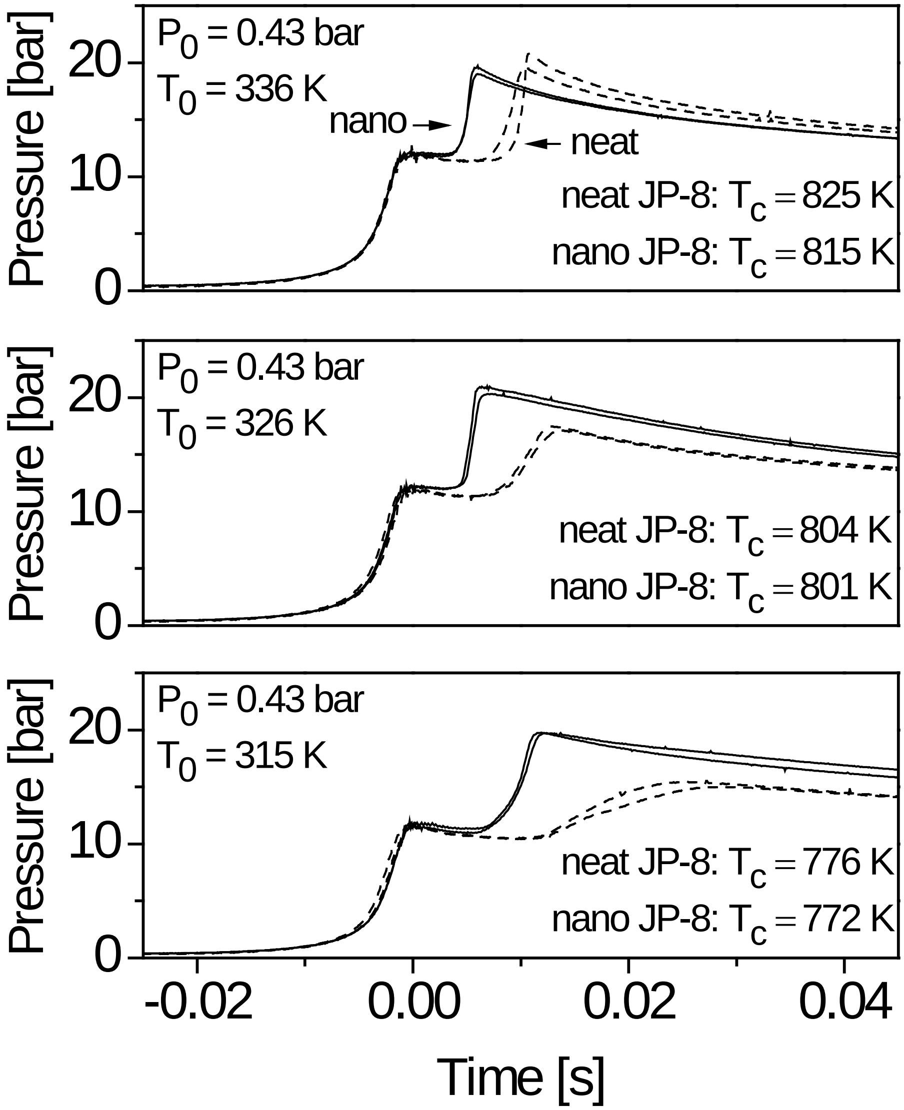

Figure 5-3. Reactive pressure traces for neat JP-8 (dashed lines) and for nanoparticle-enhanced JP-8 (solid lines). Molar composition: JP-8/O_2/N_2 = 1.0/32.5/122.2.

Energetic-nanoparticle enhanced combustion was also tested by adding nano-aluminum (2 %-wt) to JP-8. For all tests, we have assumed the molecular formula of JP-8 to be $C_{11}H_{21}$ [33]. Before testing nanoparticle-enhanced mixtures, we established a baseline for JP-8 by obtaining ignition delays for varying compressed temperatures. These compressed temperatures were calculated using Jet-A thermodynamic data [31] because JP-8 data is unavailable. Changes in compressed temperature were made by altering the initial temperature of the charge. Nanoparticle enhanced mixtures of JP-8 were tested at the same conditions as the neat JP-8 fuel, and the results are shown in Figure 5-3. The three plots in Figure 5-3 compare neat JP-8 and nanoparticle-enhanced JP-8 ignition at three different compressed temperatures. For each of the compressed temperatures tested, the presence of the nanoparticles at 2 %-wt concentrations led to a reduction in ignition delay of nearly 50 %. Additionally, for all tests conducted at $T_C \leq 804$ K, the heat release rate is increased over that of the neat JP-8 test. To our knowledge, this is the first observation of nanoparticle-enhanced combustion of JP-8 at concentrations of less than 5 %-wt. As with tests of nanoparticle-enhanced ethanol, we suspect the enhancement is a consequence of the increased thermal conductivity and faster evaporation of the liquid fuel and nanoparticle mixtures, relative to the neat liquid fuels.

5.6. Conclusion

An aerosol RCM has been designed and built for the purpose of testing nanoparticle-enhanced liquid fuels. The aerosol RCM has been demonstrated as a viable tool for investigating the influence of nanoparticle additives on the ignition delays of fuels. Aerosol ignition tests confirmed that the RCM produces repeatable ignition delays within ±10 % for identical test conditions.

The addition of energetic nanoparticles at low concentrations has been shown to significantly alter the ignition characteristics of ethanol and of JP-8. In ethanol, nano-aluminum concentrations as low as 2 %-wt led to an average ignition delay reduction of 32 % at the conditions tested. Nanoparticle-enhanced (2 %-wt) JP-8 showed ignition delay reductions approaching 50 % for all compressed temperatures tested, and led to faster heat release during ignition at compressed temperatures of less than 804 K. It is hypothesized that the addition of aluminum nanoparticles to the liquid fuel increases the thermal conductivity of the droplets relative to the neat liquid fuel droplets, and that this increased thermal conductivity drives faster evaporation and the earlier onset of ignition. It is unclear whether the reduction in ignition delay results from fuel vapor ignition or from ignition of the nanoparticles. Ongoing work in our lab seeks to identify the contributions of these sources to the ignition delay reduction and to validate our hypothesis of faster evaporation.

Chapter 6:

CONCLUSIONS & PROPOSED FUTURE WORK

Conclusions regarding technical matter in this work have been presented as part of each chapter that documents a given research project. To conclude this dissertation, additional remarks are offered to address general aspects of these research projects and provide considerations for future research.

At the conclusion of this work, the RCM may be considered a world-class design, capable of producing relevant and useful kinetic data. The RCM can be used to efficiently investigate the autoignition behavior of a fuel in the low-temperature oxidation regime. Elucidation of fuel kinetics in this region are important today, and will continue to grow in importance for modeling purposes as industry works to implement kinetically-controlled combustion modes into advanced compression-ignition engines. Future investigations aimed at the study of non-volatile, alternative fuels should continue to be fruitful as the civilian and military ranks consider the integration of these new fuels into existing engines and infrastructure, creating a need for the kinetic data.

In its current state, the mechanics of the RCM and the characterization of test methods, specifically the DTC approach, can be considered completed work. With the foundational test methods of the RCM operating smoothly, three potential types of research projects may be considered for the future: surrogate fuel development, the refinement of a test strategy for considering the practical combustion behavior of a fuel, and the implementation of optical diagnostics for investigating applied and fundamental topics.

6.1. Surrogate Fuel Development

The jet fuel surrogate study described in this work lays the groundwork for the optimization of a surrogate blend to describe the autoignition characteristics of bio-synthetic jet fuels. At this time, the kinetic models are limited in their offerings of high molecular weight branched paraffins, but as simulation capabilities for these species improve, so will the prediction capabilities of the surrogate. It is suggested that this type of surrogate fuel development work continue for jet fuels and other complex alternative fuel blends being considered.

For simulations that do not require predictive abilities for intermediate combustion species, the kinetic data gathered for fuels may also be used to calibrate empirical kinetic models as done at Michigan State University for methyl butanoate [173], dimethyl ether [174], and blends of methyl butanoate and *n*-heptane [175]. These calibrated models may be integrated with engine CFD codes as an indicator of expected performance.

6.2. Test Strategies to Assess Fuel Viability

Although different test methods have been developed here for investigating the autoignition characteristics of non-volatile fuels, the strategy for selecting a given method has not been described, nor has the preferred method of DTC testing been demonstrated as suitable for diesel fuels. This may be of little consequence for investigations which only require characterization of ignition behavior relative to some baseline fuel. Furthermore, there may be an opportunity to correlate spray ignition behavior with the autoignition characteristics observed in a premixed system.

With respect to this work, it is noted that new alternative fuels often must meet stringent fuel specification standards. In some cases, cetane numbers describing the ignition propensity of a fuel are measured for these fuels, but acceptable limits are not defined as part of the fuel specification. However, ignition behavior is indirectly considered because many of the fuel properties included in the specification are linked to ignition behavior (*e.g.*, distillation data) A practically-useful fuel research program would seek to firmly establish the relationship between these parameters, so that measurements of ignition behavior would be suggestive of a fuel's ability to meet specifications. Future work at Michigan State University aimed at integrating a high-pressure diesel injection system into the RCM will be a powerful tool for investigating this relationship.

6.3. Optical Diagnostics for Practical Applications

The main deficiency of the RCM is that no advanced optical diagnostic have been integrated with the design. Preliminary work has been done to establish a framework for these systems, including initial measurements, but the optical systems have not been characterized for use. The pressure data that is measurable from the RCM is a useful tool for investigating the global combustion response of a fuel for a particular condition, but an abundance of useful data may be provided by coupling the pressure curves with species concentration data or optical measurements of temperature.

Published work by Cignoli et al. [176] outlines an approach for optical measurements of soot temperature and soot volume fractions in a premixed technical burner. The measurement principle is based on the popular 2-color pyrometry technique, and is a robust means for quantifying soot formation at a given test condition. Initial steps to replicate this type of measurement in the RCM have been taken, and progress suggests that the diagnostic may be successfully implemented. If completed, this will be a powerful tool for investigating chemical soot formation, and how it may be controlled by blending oxygenates into a fuel.

APPENDIX

APPENDIX

Python Codes for Cantera Simulations

```
##--------------------------------------------------------------------------------------------------------------
##      velocityProfile.py
##--------------------------------------------------------------------------------------------------------------
##      This program reads in effective volume profile data as a function of time, and calculates
##      the corresponding piston velocity as a function of time. The effective volume profile data
##      is split into two regions: (1) prior to TDC and (2) after TDC. The calculated volume
##      profiles for each of these regions are fit with nth order polynomials to eliminate noise in
##      the data. This new fit is used as a basis for calculating the piston velocity profile. A high
##      order polynomial fit is applied to each of the calculated velocity profiles (e.g., before and
##      after TDC), and the coefficients are exported to a text file. These coefficients are used in
##      Cantera to set the rate of the piston in the engine simulator.
##--------------------------------------------------------------------------------------------------------------

from numpy import *
import matplotlib.pyplot as plt
import csv

# Set required parameters
D = 1.0                                       # Piston diameter -- arbitrary selection

# Read in volume profile (and convert numeric arrays to lists)
profile = recfromtxt('Effective Volume Profiles\\tV_12.15.11_11_ds.txt')
time = array(profile[:,0])
vol = array(profile[:,1])

# Identify the index of TDC
tdc = vol.argmin()
print time[tdc]
print time[tdc]/(4.e-5)

# Make necessary adjustments to data
#time = time - time[0]          # Set the first element to time zero – Cantera doesn’t accept t<0
#vol[(tdc+1):] = vol[(tdc+1):] + (vol[tdc] - vol[(tdc+1)])       # Improve consistency @ transition

# Split the volume profile and time data into BTDC and ATDC regions (add a few points on
# either side of domain for improved fit)
volB = vol[:(tdc+5)]
volA = vol[(tdc+1):]

tB = time[:(tdc+5)]
tA = time[(tdc+1):]

# Generate nth order polynomial fits for volume data
```

```
# Alter the polynomial order to achieve the best results
volBfit = polyfit(tB, volB, 20)
pB = poly1d(volBfit)

volAfit = polyfit(tA, volA, 7)
pA = poly1d(volAfit)

plt.figure(1)                              # Examine the fit
plt.plot(time,vol,'.',tB,pB(tB),tA,pA(tA))

# Calculate the time derivative of the volume profile, dV/dt, using the the polynomial fit as the
# basis
VB = pB(tB)
VA = pA(tA)
dt = time[1] - time[0]                     # Calculate time step
dVB = gradient(VB)/dt
dVA = gradient(VA)/dt
dV = append(dVB,dVA)

# Calculate the piston velocity based on the volume profile
uB = 4.0 * dVB / (pi  * D**2)
uA = 4.0 * dVA / (pi  * D**2)
u = append(uB,uA)

# Calculate the fit for the velocity profile data
uBfit = polyfit(tB, uB, 20)
puB = poly1d(uBfit)

uAfit = polyfit(tA, uA, 7)
puA = poly1d(uAfit)

plt.figure(2)                              # Examine the velocity profile data
plt.plot(tB,uB,'.',tB,puB(tB),tA,uA,'.',tA,puA(tA))

plt.figure(3)                              # Examine the velocity profile data
plt.plot(tB,uB,tB,puB(tB),'.')

plt.show()

# Save velocity coefficients to a text file for use by Cantera. Note the output format
# here is appropriate for Numpy. To be used by Cantera for calculating the velocity profile
# the polynomial coefficients must be reversed to yield accurate calculations. Numpy and
# Cantera evaluate polynomials differently.
savetxt('velcoeff_BTDC.dat', uBfit, fmt="%12.16G”)
savetxt('velcoeff_ATDC.dat', uAfit, fmt="%12.16G")
```

```
##----------------------------------------------------------------------------------------------------------
##      jp8_ranzi.py
##----------------------------------------------------------------------------------------------------------
##      This conducts a premixed compression ignition simulation using piston velocity data that
##      is based on a  calculated effective volume profile. The simulation is divided into two
##      regions: (1) before TDC and (2) after TDC. Each of the regions has a unique set of
##      coefficients that are read in and used as the basis for calculating the piston velocity
##      profile. Results of the simulation are written out to a text file.
##----------------------------------------------------------------------------------------------------------

from Cantera import *
from Cantera.Reactor import *
from Cantera.Func import *
from numpy import *
import matplotlib.pyplot as plt
import csv
import time

# Read in chemical kinetic mechanisms
gas = importPhase('tot1101_cantera.cti')

# Read in polynomial coefficients for calculating piston velocity
uBfit = loadtxt('velcoeff_BTDC.dat')      # Read in polynomial coefficients -- for Numpy format
uBfit = uBfit.tolist()                    # Convert from Numpy array to Python list
uBfitrev = uBfit[::-1]                    # Read in polynomial coefficients -- for Cantera format

uAfit = loadtxt('velcoeff_ATDC.dat')      # Read in polynomial coefficients -- for Numpy format
uAfit = uAfit.tolist()                    # Convert from Numpy array to Python list
uAfitrev = uAfit[::-1]                    # Read in polynomial coefficients -- for Cantera format

piston_rate_B = Polynomial(uBfitrev)
piston_rate_A = Polynomial(uAfitrev)

piston_stop = Polynomial([0])

# Set formats for outputting data
fmt = '%12.5f  %12.9f  %12.9f  %12.9f  %12.9f'
print '%10s  %12s  %12s  %12s  %12s' % ('Time', 'Temperature', 'Pressure', 'Volume', 'Piston
Velocity')
print '%10s  %12s  %12s  %12s  %12s' % ('=======', '=======', '=======', '=======',
'=======')

# Initialize arrays for storing data
tout = []
Tout = []
Pout = []
```

```
uout = []
Vout = []

# JP-8 surrogate (Violi #3)
gas.setState_TPX(399.05, 1.5511473*OneAtm, "MCYC6:0.00111, C7H8:0.00111,
C6H6:0.000111, IC8H18:0.0006105, NC12H26:0.0081585, O2:0.2080, N2:0.7809")

r1 = Reactor(contents = gas,  volume = 1.0, name = 'rcm')
air = Air()
env = Reservoir(contents = air,  name = 'environment')

net = ReactorNet([r1])                              # Create reactor network (required)
w = Wall(r1, env, A = pi/4.0)
w.setVelocity(piston_rate_B)

t = 0.0
dt = 4.e-5
sBTDC = 875
sATDC = 1500

f = open("output.csv","w")
for n in range(sBTDC):
    t += dt
    net.advance(t)
    writeCSV(f, [net.time(), r1.temperature(), r1.pressure(), r1.volume()])
    tout.append(t)
    Tout.append(r1.temperature())
    Pout.append(r1.pressure())
    Vout.append(r1.volume())
    uout.append(piston_rate_B(t))
    print fmt % (t, r1.temperature(), r1.pressure(), r1.volume(), piston_rate_B(t))

w.setVelocity(piston_rate_A)

for n in range(sATDC):
    t += dt
    net.advance(t)
    writeCSV(f, [net.time(), r1.temperature(), r1.pressure(), r1.volume()])
    tout.append(t)
    Tout.append(r1.temperature())
    Pout.append(r1.pressure())
    Vout.append(r1.volume())
    uout.append(piston_rate_A(t))
    print fmt % (t, r1.temperature(), r1.pressure(), r1.volume(), piston_rate_A(t))

f.close()
```

```
plt.figure(1)
plt.plot(tout, Tout)
plt.show()
```

REFERENCES

REFERENCES

[1] G. Mittal and C.J. Sung, *Combust. Sci. Technol.* 179 (2007) 497-530.

[2] K. Kumar and C.-J. Sung, *Combust. Flame* 157 (4) (2010) 676-685.

[3] S. Dooley, S.H. Won, M. Chaos, J. Heyne, Y. Ju, F.L. Dryer, K. Kumar, C.-J. Sung, H. Wang, M.A. Oehlschlaeger, R.J. Santoro and T.A. Litzinger, *Combust. Flame* 157 (12) (2010) 2333-2339.

[4] K.G. Falk, *Journal of the American Chemical Society* 28 (1906) 1517.

[5] K.G. Falk, *Journal of the American Chemical Society* 29 (1907) 1536.

[6] W.S. Affleck and A. Thomas, *Proc. Inst. Mech. Engrs.* 183 (1) (1969) 365-385.

[7] P. Beeley, J.F. Griffiths and P. Gray, *Combust. Flame* 39 (1980) 255-268.

[8] S.B. Gupta, R.R. Sekar, G.M. Klett and M. Ghaffarpour, *SAE Transactions Journal of Fuels and Lubricants* SAE 2005-01-2189 (2005)

[9] I. Kitsopanidis and W.K. Cheng, *J. Eng. Gas Turbines Power* 128 (4) (2006) 942.

[10] D. Lee and S. Hochgreb, *Int. J. Chem. Kinet.* 30 (6) (1998) 385-406.

[11] M.T. Donovan, X. He, T.R. Palmer, B.T. Zigler and M.S. Wooldridge, *Combust. Flame* 137 (2004) 351-365.

[12] M. Ribaucour, R. Minetti, M. Carlier and L.R. Sochet, *Journal de Chimie Physique* 89 (1992) 2121-2152.

[13] G. Mittal, *A rapid compression machine - design, characterization, and autoignition investigations* (2006), Doctor of Philosophy Thesis. Case Western Reserve University.

[14] J.F. Griffiths, J.P. MacNamara, C. Mohamed, B.J. Whitaker, J. Pan and C.G.W. Sheppard, *Faraday Discussions* 119 (2002)

[15] G. Mittal and C.-J. Sung, *Combust. Flame* 145 (1-2) (2006) 160.

[16] S. Tanaka, F. Ayala and J.C. Keck, *Combust. Flame* 133 (4) (2003) 467-481.

[17] J. Würmel, E.J. Silke, H.J. Curran, M.S. Ó Conaire and J.M. Simmie, *Combust. Flame* 151 (1–2) (2007) 289-302.

[18] R.K. Hanson, *Shock Tube/Laser Absorption Studies of Chemical Kinetics*, CEFRC Second Annual Conference, (2011).

[19] K. Kumar, G. Mittal and C.-J. Sung, *Combust. Flame* 156 (6) (2009) 1278.

[20] S. Gersen, N.B. Anikin, A.V. Mokhov and H.B. Levinsky, *International Journal of Hydrogen Energy* 33 (7) (2008) 1957-1964.

[21] J. Clarkson, J.F. Griffiths, J.P. MacNamara and B.J. Whitaker, *Combust. Flame* 125 (3) (2001) 1162.

[22] P. Desgroux, L. Gasnot and L.R. Sochet, *Appl. Phys. B: Lasers O.* 61 (1) (1995) 69-72.

[23] J.F. Griffiths, Q. Jiao, W. Kordylewski, M. Schreiber, J. Meyer and K.F. Knoche, *Combust. Flame* 93 (3) (1993) 303-315.

[24] D. Lee and S. Hochgreb, *Combust. Flame* 114 (3) (1998) 531-545.

[25] P. Park, *Rapid Compression Machine Measurements of Ignition Delays for Primary Reference Fuels* (1990), Doctor of Philosopy Thesis. Massachusetts Institute of Technology.

[26] J. Würmel and J.M. Simmie, *Combust. Flame* 141 (4) (2005) 417.

[27] P. Park and J.C. Keck, *SAE Transactions* 99 (900027) (1990) 11-23.

[28] M.T. Donovan, X. He, B.T. Zigler, T.R. Palmer, M.S. Wooldridge and A. Atreya, *Combust. Flame* 137 (3) (2004) 351-365.

[29] S. Gersen, A.V. Mokhov, J.H. Darmeveil and H.B. Levinsky, *Combust. Flame* 157 (2) (2010) 240-245.

[30] S. Tanaka, F. Ayala, J.C. Keck and J.B. Heywood, *Combust. Flame* 132 (1-2) (2003) 219.

[31] A. Burcat and B. Ruscic, *New NASA Thermodynamic Polynomials Database With Active Thermochemical Tables Updates*. Report ANL 05/20 TAE 960. <ftp://ftp.technion.ac.il/pub/supported/aetdd/thermodynamics>; 1/9/2010. Mirrored at <http://garfield.chem.elte.hu/Burcat/burcat.html>; 1/9/2010.

[32] E. Ranzi, M. Dente, A. Goldaniga, G. Bozzano and T. Faravelli, *Prog. Energy Combust. Sci.* 27 (1) (2001) 99-139.

[33] S.S. Vasu, D.F. Davidson and R.K. Hanson, *Combust. Flame* 152 (1-2) (2008) 125-143.

[34] S.M. Sarathy, C.K. Westbrook, M. Mehl, W.J. Pitz, C. Togbe, P. Dagaut, H. Wang, M.A. Oehlschlaeger, U. Niemann, K. Seshadri, P.S. Veloo, C. Ji, F.N. Egolfopoulos and T. Lu, *Combust. Flame* 158 (12) (2011) 2338-2357.

[35] U.S.D.o. Defense. *Annual Energy Management Report, Fiscal Year 2009* (2010), available at

[36] U.S.A. Force. *Air Force Energy Plan* (2010), available at <http://www.safie.hq.af.mil/shared/media/document/AFD-091208-027.pdf>.

[37] P. Dagaut and M. Cathonnet, *Prog. Energy Combust. Sci.* 32 (1) (2006) 48-92.

[38] M.S.P. Kahandawala, M.J. DeWitt, E. Corporan and S.S. Sidhu, *Energ. Fuel* 22 (6) (2008) 3673-3679.

[39] A.J. Dean, O.G. Penyazkov, K.L. Sevruk and B. Varatharajan, *Proceedings of the Combustion Institute* 31 (2) (2007) 2481-2488.

[40] G. Fernandes, J. Fuschetto, Z. Filipi, D. Assanis and H. McKee, *Proceedings of the Institution of Mechanical Engineers, Part D: Journal of Automobile Engineering* 221 (8) (2007) 957-970.

[41] P. Schihl, L. Hoogterp, H. Pangilinan, E. Schwarz and W. Bryzik, *Modeling JP-8 Fuel Effects on Diesel Combustion Systems*, Report No. RDECOM-TARDEC, 2006.

[42] V.K. Rao and M.F. Bardon, *Industrial & Engineering Chemistry Process Design and Development* 24 (2) (1985) 498-500.

[43] E. Corporan, T. Edwards, L. Shafer, M.J. DeWitt, C. Klingshirn, S. Zabarnick, Z. West, R. Striebich, J. Graham and J. Klein, *Energ. Fuel* 25 (3) (2011) 955-966.

[44] J.D. Kinder, *Evaluation of Bio-Derived Synthetic Paraffinic Kerosenes (Bio-SPKs)*, Report No. The Boeing Company, UOP, United States Air Force Research Laboratory, 2010.

[45] S. Blakey, L. Rye and C.W. Wilson, *Proc. Combust. Inst.* 33 (2) (2011) 2863-2885.

[46] A. Violi, S. Yan, E.G. Eddings, A.F. Sarofim, S. Granata, T. Faravelli and E. Ranzi, *Combustion Science and Technology* 174 (11) (2002) 399-417.

[47] C.K. Westbrook, W.J. Pitz, O. Herbinet, H.J. Curran and E.J. Silke, *Combust. Flame* 156 (1) (2009) 181-199.

[48] J.E. Dec, W. Hwang and M. Sjöberg, *An Investigation of Thermal Stratification in HCCI Engines Using Chemiluminescence Imaging*, SAE Paper, 2006-01-1518 (2006).

[49] B.L. Smith and T.J. Bruno, *Energ. Fuel* 21 (5) (2007) 2853-2862.

[50] H.-P.S. Shen, J. Steinberg, J. Vanderover and M.A. Oehlschlaeger, *Energ. Fuel* 23 (5) (2009) 2482-2489.

[51] C.M. Allen, E. Toulson and T. Lee, in: *49th AIAA Aerospace Sciences Meeting Including the New Horizons Forum and Aerospace Exposition*, 2011. Paper No. AIAA-2011-0604.

[52] T. Edwards and L.Q. Maurice, *Journal of Propulsion and Power* 17 (2) (2001) 461-466.

[53] American Society for Testing and Materials (ASTM). *Standard Test Method for Determination of Ignition Delay and Derived Cetane Number (DCN) of Diesel Fuel Oils by Combustion in a Constant Volume Chamber*. West Conshohocken, PA: ASTM International.

[54] G.B. Bessee, S.A. Hutzler and G.R. Wilson, *Propulsion and Power Rapid Response Research and Development (R&D) Support, Delivery Order 0011: Analysis of Synthetic Aviation Fuels*, Report No. AFRL-RZ-WP-TR-2011-2084, Southwest Research Institute, 2011.

[55] E.J. Silke, H.J. Curran and J.M. Simmie, *Proc. Combust. Inst.* 30 (2) (2005) 2639-2647.

[56] M.A. Oehlschlaeger, H.-P.S. Shen, J. Steinberg and J. Vanderover, *The Ignition of C7 and C16 Normal and Branched Alkanes at Elevated Pressures*, Proceedings of the 6th U.S. National Combustion Meeting, (2010).

[57] S. Dooley, S.H. Won, J. Heyne, T.I. Farouk, Y. Ju, F.L. Dryer, K. Kumar, X. Hui, C.-J. Sung, H. Wang, M.A. Oehlschlaeger, V. Iyer, S. Iyer, T.A. Litzinger, R.J. Santoro, T. Malewicki and K. Brezinsky, *Combust. Flame* 159 (4) (2012) 1444-1466.

[58] A. Demirbas, *Energ. Convers. Manage.* 50 (9) (2009) 2239.

[59] in: G. Knothe, J. Krahl and J.V. Gerpen (Eds.), *The Biodiesel Handbook*, AOCS Press, Champaign, Illinois, 2005, p.

[60] M. Lapuerta, O. Armas and J. Rodríguez-Fernández, *Prog. Energy Combust. Sci.* 34 (2) (2008) 198.

[61] M. Canakci and J.H. Van Gerpen, *Transactions of the ASABE* 46 (4) (2003) 937-944.

[62] G. Knothe, in: G. Knothe, J. Van Gerpen, and J. Krahls, *Introduction*, AOCS Press, Champaign, IL, 2005, p. 1-3.

[63] J. Sheehan, T. Dunahay, J. Benemann and P. Roessler, *A Look Back at the U.S. Department of Energy's Aquatic Species Program - Biodiesel from Algae*, Report No. NREL/TP-580-24190, National Renewable Energy Laboratory, 1998.

[64] N.S. Venkataraman, *Nandini Chem J IX* 9 (10) (2002) 19-21.

[65] M. Mittelbach and C. Remschmidt, *Biodiesels - The Comprehensive Handbook*, Karl-Franzens University, Graz, Austria, 2004, p.

[66] A. Demirbas, *Biodiesel: A realistic fuel alternative for diesel engines*, Springer, London, 2008, p. 208.

[67] American Society for Testing and Materials (ASTM). *Standard Specification for Biodiesel Fuel Blend Stock (B100) for Middle Distillate Fuels*. West Conshohocken, PA: ASTM International.

[68] K.J. Harrington, *Biomass* 9 (1) (1986) 1-17.

[69] W. Klopfenstein, *Journal of the American Oil Chemists' Society* 59 (12) (1982) 531-533.

[70] R. Dunn, *Journal of the American Oil Chemists' Society* 85 (10) (2008) 961-972.

[71] W. Klopfenstein, *Journal of the American Oil Chemists' Society* 62 (6) (1985) 1029-1031.

[72] A.H. Lefebvre, A.M. Mellor and J.E. Peters, in: C.T. Bowman, and J. Birkelands, *Ignition/Stabilization/Atomization-Alternative Fuels in Gas Turbine Combustors*, American Institute of Aeronautics and Astronautics, 1978, p. 137-159.

[73] J.E. Peters and A.M. Mellor, *Combust. Flame* 38 (1980) 65-74.

[74] B. Bougie, M. Tulej, T. Dreier, N.J. Dam, J.J. Ter Meulen and T. Gerber, *Appl. Phys. B: Lasers O.* 80 (8) (2005) 1039-1045.

[75] U. Azimov, K. Kim, D. Jeong and Y. Lee, *Int. J. Automot. Techn.* 10 (3) (2009) 265-276.

[76] J.E. Dec, *Proc. Combust. Inst.* 32 (2) (2009) 2727.

[77] M. Ikegami, K. Miwa and M. Inada, *B. JSME* 24 (195) (1981) 1608-1615.

[78] S. Kobori, T. Kamimoto and A.A. Aradi, *Int. J. Engine Res.* 1 (1) (2000) 29-39.

[79] K. Miwa, T. Ohmiya and T. Nishiwaki, *Jap. Soc. Mech. Engrs Int. J., Ser. II* 31 (1) (1988) 166.

[80] T.J. Callahan and T.W. Ryan, *Engine and Constant Volume Bomb Studies of Diesel Ignition and Combustion*, SAE Paper, 881626 (1988).

[81] C.F. Edwards and L.D. Siebers, *A study of the autoignition process of a diesel spray via high speed visualization*, SAE Paper, 920108 (1992).

[82] H.H. Wolfer, *VDI. Forsch.-hf* 392 (1938) 15.

[83] D.N. Assanis, Z.S. Filipi, S.B. Fiveland and M. Syrimis, *J. Eng. Gas Turbines Power* 125 (2) (2003) 450-457.

[84] C.V. Callahan, T.J. Held, F.L. Dryer, R. Minetti, M. Ribaucour, L.R. Sochet, T. Faravelli, P. Gaffuri and E. Rani, *Symp. (Int.) Combust* 26 (1) (1996) 739.

[85] H.O. Hardenberg and F.W. Hase, *SAE Transactions* 88 (790493) (1979)

[86] D.R. Haylett, P.P. Lappas, D.F. Davidson and R.K. Hanson, *Proc. Combust. Inst.* 32 (2008)

[87] L.J. Spadaccini and J.A. Tevelde, *Combust. Flame* 46 (1982) 283-300.

[88] C. Allen, E. Toulson, T. Edwards and T. Lee, *Combust. Flame* In Review - Available Upon Request (2011)

[89] S. Bax, M.H. Hakka, P.-A. Glaude, O. Herbinet and F. Battin-Leclerc, *Combust. Flame* 157 (6) (2010) 1220-1229.

[90] P. Dagaut, S. Gaïl and M. Sahasrabudhe, *Proc. Combust. Inst.* 31 (2) (2007) 2955-2961.

[91] M.H. Hakka, P.-A. Glaude, O. Herbinet and F. Battin-Leclerc, *Combust. Flame* 156 (11) (2009) 2129-2144.

[92] J.V. Pastor, R. Payri, J. Gimeno and J.G. Nerva, *Energ. Fuel* 25 (2) (2010) 843-843.

[93] A. Schönborn, N. Ladommatos, J. Williams, R. Allan and J. Rogerson, *Effects on Diesel Combustion of the Molecular Structure of Potential Synthetic Bio-Fuel Molecules*, SAE Paper, 2007-24-0125 (2007).

[94] A. Schönborn, N. Ladommatos, J. Williams, R. Allan and J. Rogerson, *Combust. Flame* 156 (7) (2009) 1396.

[95] American Society for Testing and Materials (ASTM). *Standard Test Method for Cetane Number of Diesel Fuel Oil*. West Conshohocken, PA: ASTM International.

[96] M.S. Graboski and R.L. McCormick, *Prog. Energy Combust. Sci.* 24 (2) (1998) 125-164.

[97] B. Freedman and M. Bagby, *Journal of the American Oil Chemists' Society* 67 (9) (1990) 565-571.

[98] W. Klopfenstein, in: *Vegetable Oil as a Diesel Fuel: Seminar III*, 1983. Paper No.

[99] G. Knothe, M.O. Bagby and T.W. Ryan, *Cetane Numbers of Fatty Compounds: Influence of Compound Structure and of Various Potential Cetane Improvers*, SAE Paper, 971681 (1997).

[100] R.O. Dunn, *Fuel Process. Technol.* 86 (10) (2005) 1071.

[101] R.O. Dunn, *Energ. Fuel* 23 (8) (2009) 4082-4091.

[102] G. Knothe, *Fuel Process. Technol.* 86 (10) (2005) 1059-1070.

[103] G. Knothe, *Energ. Fuel* 22 (2) (2008) 1358-1364.

[104] G. Knothe, *Energy & Environmental Science* 2 (7) (2009) 759-766.

[105] G. Knothe, A.C. Matheaus and T.W. Ryan, *Fuel* 82 (8) (2003) 971-975.

[106] B.R. Moser, *In Vitro Cellular & Developmental Biology - Plant* 45 (3) (2009) 229-266.

[107] B.R. Moser and S.F. Vaughn, *Biomass and Bioenergy* 34 (4) (2010) 550-558.

[108] B.R. Moser and S.F. Vaughn, *Bioresource Technology* 101 (2) (2010) 646-653.

[109] G. Knothe, *Fuel Process. Technol.* 88 (7) (2007) 669-677.

[110] G. Knothe, in: T. Yaos, *The Potential of Biodiesel with Improved Properties to an Alternative Energy Mix*, Springer Japan, 2011, p. 75-82.

[111] N.A. Bringe, in: G. Knothe, J. Van Gerpen, and J. Krahls, *Soybean oil composition for biodiesel*, AOCS Press, Champaign, IL, 2005, p. 161-164.

[112] A.J. Kinney and T.E. Clemente, *Fuel Process. Technol.* 86 (10) (2005) 1137-1147.

[113] T. Vaughn, M. Hammill, M. Harris and A. Marchese, *Ignition Delay of Bio-Ester Fuel Droplets*, S.A.E (2006).

[114] A.J. Marchese, T.L. Vaughn, K. Kroenlein and F.L. Dryer, *Proc. Combust. Inst.* 33 (2) (2011) 2021-2030.

[115] K. Seshadri, T. Lu, O. Herbinet, S. Humer, U. Niemann, W.J. Pitz, R. Seiser and C.K. Law, *Proc. Combust. Inst.* 32 (1) (2009) 1067-1074.

[116] W. Yuan, A.C. Hansen and Q. Zhang, *Fuel* 84 (7-8) (2005) 943.

[117] J.V. Gerpen, B. Shanks, R. Pruszko, D. Clements and G. Knothe, *Biodiesel production technology*, Report No. NREL/SR-510-36244, National Renewable Energy Laboratory, 2004.

[118] F. Avella, A. Galtieri and A. Fiumara, *Rivista dei combustibili* 46 (6) (1992) 181-188.

[119] T. Bouché, M. Hinz, R. Pittermann and M. Herrmann, *Optimising tractor CI engines for biodiesel operation*, SAE Paper, 2000-01-1969 (2000).

[120] J. Krahl, K. Baum, U. Hackbarth, H.E. Jeberien, A.M.C.S.O. Schröder, N. Walter, J. Bünger, M.M. Müller and A. Weigel, *Trans. ASAE* 44 (2) (2001) 179-191.

[121] M. Canakci and J. Van Gerpen, *The Performance and Emissions of a Diesel Engine Fueled with Biodiesel from Yellow Grease and Soybean Oil*, 2001 ASAE Annual Meeting, (2001).

[122] A. Yahya and S.J. Marley, *Biomass and Bioenergy* 6 (4) (1994) 321-328.

[123] E. Alptekin and M. Canakci, *Renew. Energ.* 33 (12) (2008) 2623-2630.

[124] C. Allen, K. Watts and R. Ackman, *Journal of the American Oil Chemists' Society* 76 (3) (1999) 317-323.

[125] C.E. Ejim, B.A. Fleck and A. Amirfazli, *Fuel* 86 (10-11) 1534-1544.

[126] *MSDS Summary Sheet: No. 2 Diesel Fuel*, Report No. Phillips Petroleum Company,

[127] C.E. Goering, A.W. Schwab, M.J. Daugherty, E.H. Pryde and A.J. Heakin, *Trans. ASAE* 25 (6) (1982) 1472-1477.

[128] A. Tsolakis and S.E. Golunski, *Chem. Eng. J.* 117 (2) (2006) 131-136.

[129] M.M. El-Wakil, P.S. Myers and O.A. Uyehara, *SAE Transactions* 64 (1956) 712–726.

[130] C. Espey, J.E. Dec, T.A. Litzinger and D.A. Santavicca, *Combust. Flame* 109 (1-2) (1997) 65-78.

[131] M.C. Wolff, J. Meisl, R. Koch and S. Wittig, *Symp. (Int.) Combust* 27 (2) (1998) 2025-2031.

[132] C.L. Yaws, *Yaws' Thermophysical Properties of Chemicals and Hydrocarbons*, Knovel, Norwich, N.Y., 2009.

[133] S.W. Benson, *Thermochemical Kinetics*, John Wiley & Sons, Inc., New York, 1968, p. 223.

[134] O. Herbinet, W.J. Pitz and C.K. Westbrook, *Combust. Flame* 154 (3) (2008) 507-528.

[135] E.R. Ritter, *Journal of Chemical Information and Computer Sciences* 31 (3) (1991) 400-408.

[136] E.R. Ritter and J.W. Bozzelli, *Int. J. Chem. Kinet.* 23 (9) (1991) 767-778.

[137] V. Růžička, Jr. and E.S. Domalski, *J. Phys. Chem. Ref. Data* 22 (3) (1993) 619-657.

[138] C.-H. Tu and C.-P. Liu, *Fluid Phase Equilibr.* 121 (1-2) (1996) 45-65.

[139] L. Constantinou and R. Gani, *AIChE J.* 40 (10) (1994) 1697-1710.

[140] S.S. Sazhin, *Prog. Energy Combust. Sci.* 32 (2) (2006) 162-214.

[141] R.P. Durret, D.C. Oren and C.R. Ferguson, *A multidimensional data set for Diesel combustion model validation: I. Initial conditions, pressure history and spray shapes*, SAE Paper, 872087 (1987).

[142] J.S. Chin and A.H. Lefebvre, *Int. J. Turbo Jet Eng.* 2 (1985) 315-325.

[143] W.J.D. Annand, *Proc. Inst. Mech. Engrs.* 177 (1963) 973-990.

[144] G.F. Hohenberg, *Advanced Approaches for Heat Transfer Calculations*, SAE Paper, 790825 (1979).

[145] G. Woschni, *A Universally Applicable Equation for the Instantaneous Heat Transfer Coefficient in the Internal Combustion Engine*, S.A.E Paper 670931 (1967).

[146] H.S. Soyhan, H. Yasar, H. Walmsley, B. Head, G.T. Kalghatgi and C. Sorusbay, *Appl. Therm. Eng.* 29 (2-3) (2009) 541-549.

[147] S.S. Goldsborough, *Evaluating the Heat Losses from HCCI Combustion within a Rapid Compression Expansion Machine,* S.A.E. Paper 2006-01-0870 (2006).

[148] N. Watson, A.D. Pilley and M. Marzouk, *A Combustion Correlation for Diesel Engine Simulation*, S.A.E (1980).

[149] C.M. Allen, E. Toulson, D.L.S. Hung, H. Schock, D. Miller and T. Lee, *Energ. Fuel* 25 (7) (2011) 2896-2908.

[150] C.L. Peterson, J.S. Taberski, J.C. Thompson and C.L. Chase, 43 (6) (2000) 1371-1381.

[151] Advanced Engine Technology Ltd., *Diesel Fuel Ignition Quality Tester (IQT)* (2009), available at

<http://aet.ca/files/resourcesmodule/@random428b4e06ecd32/1254780127_IQT_Brochure___June_18__2009_with_EN590__stainless_steel_mod.pdf>.

[152] C.K. Westbrook, *Proc. Combust. Inst.* 28 (2) (2000) 1563.

[153] Y. Zhang, Y. Yang and A.L. Boehman, *Combust. Flame* 156 (6) (2009) 1202-1213.

[154] M.J. Pilling, *Proc. Combust. Inst.* 32 (1) (2009) 27-44.

[155] D. Bradley, C.G.W. Sheppard, I.M. Suardjaja and R. Woolley, *Combust. Flame* 138 (1-2) (2004) 55-77.

[156] E. Toulson, H.C. Watson and W.P. Attard, *SAE 2009-01-0506* (2009)

[157] S.M. Starikovskaia, *Journal of Physics D: Applied Physics* 39 (16) (2006) R265-R299.

[158] K.K. Kuo, G.A. Risha, B.J. Evans and E. Boyer, in: *2003 Materials Research Society Fall Meeting*, 2003. Paper No. AA1.1.

[159] G.V. Ivanov, and F. Tepper, in: K.K. Kuo, T.B. Brill, R.A. Pesce-Rodriguez, A.R. Mitchell, J. Covino, S.K. Chan, A. Peretz, N.-E. Gunners, S.T. Thynell and S.H. Chan (Eds.), *Challenges in Propellants and Combustion: 100 Years After Nobel*, Begell House, New York, 1997, p. 636-645.

[160] A. Rai, K. Park, L. Zhou and M.R. Zachariah, *Combustion Theory and Modelling* 10 (5) (2006) 843-859.

[161] N.M. Marinov, *International Journal of Chemical Kinetics* 31 (3) (1999) 183-220.

[162] T. Bazyn, H. Krier and N. Glumac, *Combust. Flame* 145 (4) (2006) 703.

[163] M.W. Beckstead, Y. Liang and K.V. Pudduppakkam, *Combustion, Explosion, and Shock Waves* 41 (6) (2005) 622-638.

[164] A.L. Breiter, V.M. Mal'tsev and E.I. Popov, *Combustion, Explosion, and Shock Waves (English Translation of Fizika Goreniya i Vzryva)* 13 (4) (1977) 475.

[165] A.K. Lokenbakh, N.A. Zaporina, A.Z. Knipele, V.V. Strod and L.K. Lepin, *Combustion, Explosion, and Shock Waves* 21 (1) (1985) 69-77.

[166] M.M. Mench, K.K. Kuo, C.L. Yeh and Y.C. Lu, *Combustion Science and Technology* 135 (1) (1998) 269-292.

[167] D.E. Jackson, D.F. Davidson and R.K. Hanson, in: *44th AIAA/ASME/SAE/ASEE Joint Propulsion Conference & Exhibit*, 2008. Paper No. AIAA-2008-4767.

[168] H. Tyagi, P.E. Phelan, R. Prasher, R. Peck, T. Lee, J.R. Pacheco and P. Arentzen, *Nano Letters* 8 (5) (2008) 1410-1416.

[169] J.M. Char, W.J. Liou, J.H. Yeh and C.L. Chiu, *Shock Waves* 6 (5) (1996) 259-266.

[170] K. Kumar and C.J. Sung, *Combust. Flame* 157 (4) (2010) 676-685.

[171] G. Freeman and A.H. Lefebvre, *Combust. Flame* 58 (1984) 152-156.

[172] J.A. Eastman, S.U.S. Choi, S. Li, W. Yu and L.J. Thompson, *Applied Physics Letters* 78 (6) (2001) 718-720.

[173] E. Toulson, C.M. Allen, D.J. Miller and T. Lee, *Energ. Fuel* 24 (2) (2009) 888-896.

[174] E. Toulson, C.M. Allen, D.J. Miller, H.J. Schock and T. Lee, *Energ. Fuel* 24 (6) (2010) 3510-3516.

[175] E. Toulson, C.M. Allen, D.J. Miller, J. McFarlane, H.J. Schock and T. Lee, *Energ. Fuel* 25 (2) (2011) 632-639.

[176] F. Cignoli, S. De Iuliis, V. Manta and G. Zizak, *Appl. Opt.* 40 (30) (2001) 5370-5378.